AN EVALUATION OF ULTRASONIC SHOT PEENING AND ABRASIVE FLOW MACHINING AS SURFACE FINISHING PROCESSES FOR SELECTIVE LASER MELTED 316L

A Thesis

presented to

the Faculty of California Polytechnic State University,

San Luis Obispo

In Partial Fulfillment

of the Requirements for the Degree

Master of Science in Industrial Engineering

by

Rhys William Gilmore

June 2018

COMMITTEE MEMBERSHIP

TITLE: An Evaluation of Ultrasonic Shot Peening and Abrasive Flow Machining as Surface Finishing Processes for Selective Laser Melted 316L

AUTHOR: Rhys Gilmore

DATE SUBMITTED: June 2018

COMMITTEE CHAIR: Xuan Wang, Ph.D.

Professor of Industrial and Manufacturing Engineering

COMMITTEE MEMBER: Kaveh Kabir, Ph.D.

Professor of Aerospace Engineering

COMMITTEE MEMBER: Thomas Pluschkell, M.S.

Lawrence Livermore National Laboratory

ABSTRACT

An Evaluation of Ultrasonic Shot Peening and Abrasive Flow Machining
As Surface Finishing Processes for Selective Laser Melted 316L

Rhys William Gilmore

Additive Manufacturing, and specifically powder bed fusion processes, have advanced rapidly in recent years. Selective Laser Melting in particular has been adopted in a variety of industries from biomedical to aerospace because of its capability to produce complex components with numerous alloys, including stainless steels, nickel superalloys, and titanium alloys. Post-processing is required to treat or solve metallurgical issues such as porosity, residual stresses, and surface roughness. Because of the geometric complexity of SLM produced parts, the reduction of surface roughness with conventional processing has proven especially challenging. In this Thesis, two processes, abrasive flow machining and ultrasonic shot peening, are evaluated as surface finishing processes for selective laser melted 316L. Results of these experiments indicate that AFM can reliably polish as-built internal passages to 1 µm Ra or better but is unsuitable for passages with rapidly expanding or contracting cross-sections. AFM can also polish relatively small passages, but lattice components may prove too complex for effective processing. USP cannot achieve such low surface roughness, but it is a versatile process with multiple advantages. Exterior surfaces were consistently processed to 1.7 to 2.5 µm Ra. Interior surfaces experienced only partial processing and demonstrated high geometric dependence. USP significantly hardened the surface, but steel media hardened the surface better than ceramic media did. Both AFM and USP are recommended processes for the surface finishing of SLM manufactured parts. Good engineering judgement is necessary to determine when to use these processes and how to design for post-processing.

Keywords: Selective Laser Melting, 316L, Abrasive Flow Machining, Ultrasonic Shot Peening, Post-Processing, Surface Roughness, Additive Manufacturing

ACKNOWLEDGMENTS

Much of completing a thesis in any discipling comes down to learning how to do it – and how not to. Countless people have proven indispensable on this journey and I can honestly say that, without them, I would not have reached this destination. My mission to learn what an academic thesis is, and how to do one, has been a tireless effort aided by individuals who have offered me everything from technical advice, funding, and guidance to emotional support and motivation when I needed it most. An exhaustive list of the people that allowed me to achieve my ambitions is probably downright impossible, but I owe acknowledgement it to those who have long stood by me, through thick and thin.

First and foremost, I must thank and applaud my thesis adviser, Dr. Xuan Wang, for his impeccable advice, attitude, instruction, and patience. At the inception of this research, when I hardly knew what Additive Manufacturing was, he expertly guided me towards a well-scoped and relevant subject matter. He has helped me bridge the gap between Industrial Engineering and Materials Engineering, my undergraduate discipline. Eliminating even one of our technical discussions would have had seriously negative impacts on this work. Along with his guidance came trust that I would fulfill my goals independently without hand-holding, something I appreciate considerably. Most importantly, after innumerable funding hiccups, failed builds, scope changes, and seemingly insurmountable failures, his confidence and positive attitude made me optimistic about this research every day.

The expertise of the talented engineers at Lawrence Livermore National Laboratory is woven throughout this entire body of research. Without funding from LLNL, experimental investigation into the post-processing of additively manufactured alloys would have been impossible. But the funding is merely the tip of the iceberg of their contributions. Weekly phone calls with Tommy Pluschkell, Stephen Burke, Stephen Knaus, and Matt Wraith allowed for rapid problem solving and analysis. Specifically, Tommy's endless hours spent solving our printer issues, assisting in sample design, and accommodating all my thoughts and ideas – even the silly ones – deserve special thanks. Aerospace professor Dr. Kabir, the third member of my committee after Tommy and Dr. Wang, deserves recognition as well. I first became

acquainted with Dr. Kabir when he visited the Cal Poly Materials Engineering Student Society all the way from Australia. After he joined Cal Poly the following year, I reconnected with him through the advanced materials research group he runs here. He has certainly earned my respect and admiration for tolerating my dwindling efforts on his carbon foam research project because of mounting thesis work, and I am so glad and grateful he agreed to join my committee. His expertise with cellular structures makes him the perfect individual to understand the relevance of additive manufacturing to produce low-weight lattice structures for the aerospace industry. Dr. Kabir's joyous and welcoming attitude has always brightened my day and encouraged me to search myself for intrinsic motivation, rather than relying on external encouragement.

Extrude Hone in Paramount, California earns distinct acknowledgement for being so much more than just a supplier of Abrasive Flow Machining. Thank you to Will Melendez, a talented, bright, and all-around nice guy for waiving and reducing costs to encourage my own academic research. His thorough understanding of the process and excellent ability to break down and explain the finer details were treasured additions to my thesis. Will understands the potential of a seemingly mundane technology for the rapidly growing world of additive manufacturing and I am thrilled that he chose to bring his company along for the ride. Ghislain Cossio of Empowering Technologies also merits recognition for accommodating my abnormal sample design and goals for Ultrasonic Shot Peening. Without his patience for academic research, this thesis would not exist. A thank you also goes to New York start-up nTopology for providing their incredible lattice design software free of charge for the sake of academics.

The Cal Poly faculty have earned my gratitude, respect, and admiration during my privileged time at the university. From General Physics I to Fracture and Failure Analysis, all my coursework has proven immensely useful to my academic and career pursuits. Specifically, thanks to Dr. Harding to teaching me how to use the SEM and (almost) always tolerating me putting weird samples underneath the electron beam. And without Dr. London, I never would have fallen in love with materials science. As my senior project adviser, he taught me how to endure the unrelenting re-defining and re-scoping of academic projects. Most importantly, he taught me how to work hard and feel proud of my exhaustive efforts after

the dust settles. Dr. Walsh also earns recognition for his expertise in understanding the weird and insane microstructures of selective laser melted alloys. And none of my sample manufacturing would have been possible without the highly skilled SLM machine technicians, Moira Foster and Hajime Yamanaka, for their attention to detail and persistence.

My cherished friends and family earn a special spot amongst those who have helped me along the way. Throughout my life, I have been blessed with the most incredible family and friends who have always encouraged me to keep my chin up, work hard, and achieve my goals. Thank you to my family, my incredible mother, father, and sister (and two dogs!), for providing the love and support I needed to start and finish this Master's program. Ever since I was young, they have always given me independence and freedom to pursue life as I see fit. Every step of the way, through good decisions and bad ones, they have stood by me. Without their honest support, I would be nowhere near where I am today. Special thanks to Julian Lohser – my brother in this thesis madness– for sharing complaints, hopes, and dreams for our research endeavors. Thank you also to Andrew Rudnick, Stanley Lam, Joshua Jacoby and countless others for their priceless and enduring friendships over the years. I could not have done it without them.

TABLE OF CONTENTS

LIST OF TABLES

Table Page

LIST OF FIGURES

Figure Page

Chapter I – Introduction

1.1 Additive Manufacturing

Additive manufacturing (AM), colloquially known as 3D printing, has experienced rapid growth in recent years. According to ASTM F2792, AM is "a process of joining materials to make objects from 3D model data, usually layer upon layer, as opposed to subtractive manufacturing methodologies." Significant progress has been made since the first 3D Printer was invented in 1984 by Charles W. Hull. Now, many types of AM exist, classified into seven groups: binder jetting, directed energy deposition, material extrusion, material jetting, powder bed fusion, sheet lamination, and vat photopolymerization (ASTM International, 2013). Such recent rapid growth is largely due to the expiration of the finsal fused deposition modelling patent in 2009, allowing new processes to be produced without violation of intellectual property (Attaran, 2017). Mohsen Attaran reports a list of applications and respective advantages in his market analysis of additive manufacturing, as shown in Table I.

Table 1: Advantages of Additive Manufacturing in Different Applications

Application	***Advantages***
Rapid Prototyping	Reduce time to market by accelerating prototyping and competitive innovation.
Production of Spare Parts	Reduction of repair times and costly warehousing.
Small Volume Manufacturing	Small batches can be produce cost-efficiently by eliminating tooling investment.
Customized Items	Eliminate penalty for redesign and enable mass-customization at low cost.
Complex Work Pieces	Complex work pieces at low cost.
Machine Tool Manufacturing	Reduction of labor costs and customization costs.
Rapid Manufacturing	Directly manufacture low numbers of finished components.
Component Manufacturing	Shorten supply chain, reduce development costs, and eliminate excess parts.
On-site Replacement Part Manufacturing	Eliminate storage and transportation costs, reduce need for large inventory, allow product lifecycle leverage.
Rapid Repair	Reduce repair time significantly and modify components for new design.

AM is attractive due to its potential to decentralize manufacturing processes. It is especially useful for the production of low-to-mid volume components where mold tooling would be too costly. Because of this effect, additive manufacturing has the potential to instigate a "Third Industrial Revolution" of "decentralized manufacturing" (Hebert, 2016). The decentralized attribute is particularly interesting – small companies can manufacture small quantities without collaborating with large manufacturing facilities. Analysis courtesy of European Powder Metallurgy Association (EPMA) denotes just how additive manufacturing compares to other powder metallurgy processes (Figure 1).

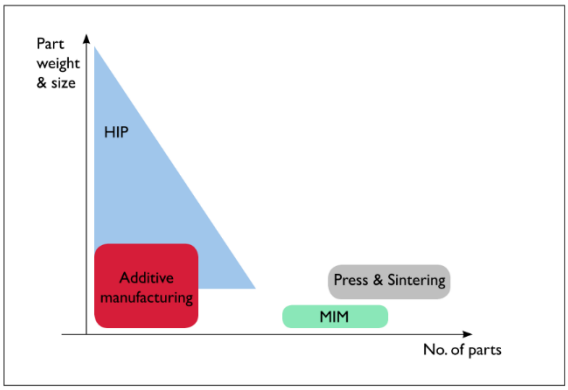

Figure 1: Additive manufacturing is the most effective PM process at low production quantities and part sizes. (EPMA, 2013)

In the past decade, the technology has advanced markedly as new processes have been invented and improved. Selective laser melting (SLM), electron beam melting (EBM), direct energy deposition (DED) and binder jetting are novel processes that can produce high quality metallic components. At first, additive manufacturing, was only used for rapid prototyping. But as technology has improved, use of additively manufactured metals has become more widespread (Attaran, 2017).

Many engineering industries are taking advantage of the benefits of additive manufacturing. The top industries currently utilizing AM are: aerospace, automotive, machine tooling, medical implants, and architecture (Attaran, 2017). Each of these industries makes use of the technology for a variety of different reasons. For architects, AM means rapid production of high quality models directly from computer developed designs. In the automotive industry, AM is too expensive for mass production but is effective for high-end, low volume vehicles and rapid prototyping. The company *Divergent 3D,* for example, has additively manufactured a high-end sportscar as a proof of concept for this technology

("Blade Supercar - Divergent," n.d.). The biomedical and aerospace industries use additive manufacturing technology most often. For implants and prosthetics, SLM is employed to customize the components to the individuals in need. Hip replacements, knee replacements, and prosthetic limbs can now be personalized for its recipients to increase biocompatibility. Additive manufacturing has proven quite useful for the aerospace industry where manufacturing volume is lower than other industries. AM allows for production of geometrically complex parts. And, particularly in aerospace, alloys may be too tough for conventional machining. The mechanical properties of AM alloys are typically better than cast, but not always as good as wrought (EPMA, 2013). Laser beam melting (LBM) is less expensive than conventional manufacturing processes at low volumes (Figure 2). For prototyping and low volume production, LBM techniques are a clear leader. The lack of complexity limitations too, make AM processes attractive. Geometrically complex parts, impossible to manufacture with conventional techniques, are possible with LBM additive manufacturing. Laser melting AM processes, especially SLM, are therefore exceptionally useful to produce high strength exotic alloys at reasonable costs in low volumes (Attaran, 2017).

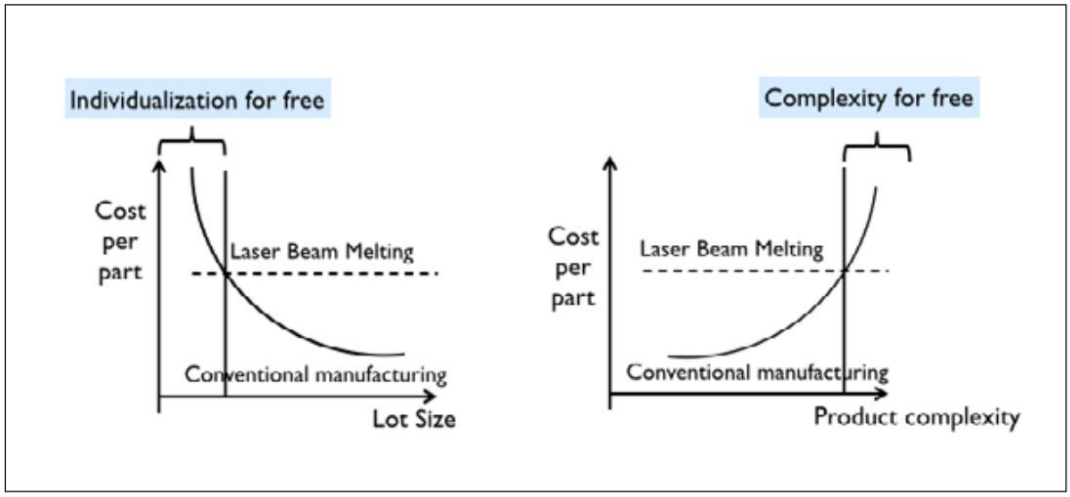

Figure 2: At low lot size, LBM processes have the advantage over conventional manufacturing, which is limited by part complexity, whereas AM processes are not limited (EPMA, 2013).

However, the technological limitations of additive manufacturing typically require post-processing of the as-built components before introduction into the engineering application. The geometric complexity of additively manufactured parts makes post-processing difficult. As a result, to improve the properties (in

particular corrosion, mechanical, and dimensional properties) more research and development is required to identify or invent key post-processing methods. This study focuses on available post-build processes for improving the surface roughness of selective laser melted (SLM) 316 stainless steel. What follows is a comprehensive literature review of SLM technology, its limitations, and candidate processes for surface finish improvement. Following the literature review are the details of the experiment examining the efficacy of two processes, Abrasive Flow Machining and Ultrasonic Shot Peening, in improving the surface finish of SLM 316L components.

Chapter II – Literature Review

2.1 Selective Laser Melting

Selective laser melting (SLM) is a powder bed fusion process that makes use of a high-power laser to melt alloy powders layer-by-layer to form three dimensional parts of complex geometries (Schmidt et al., 2017). Like other 3D printing methods, the process begins with computer assisted design (CAD). The completed CAD file is converted to an STL file, which instructs the SLM computer how to print the component layer-by-layer. As the laser melts the powder of one layer, the build plate lowers, and new powder is fed in by a roller (Figure 3). Typically, the process occurs in an inert atmosphere, such as Argon or Nitrogen, to prevent rapid oxidation of the components printed (Murr et al., 2012). The powder is typically spherical, with a size distribution that ranges from 10 – 100 microns in diameter (EPMA, 2013).

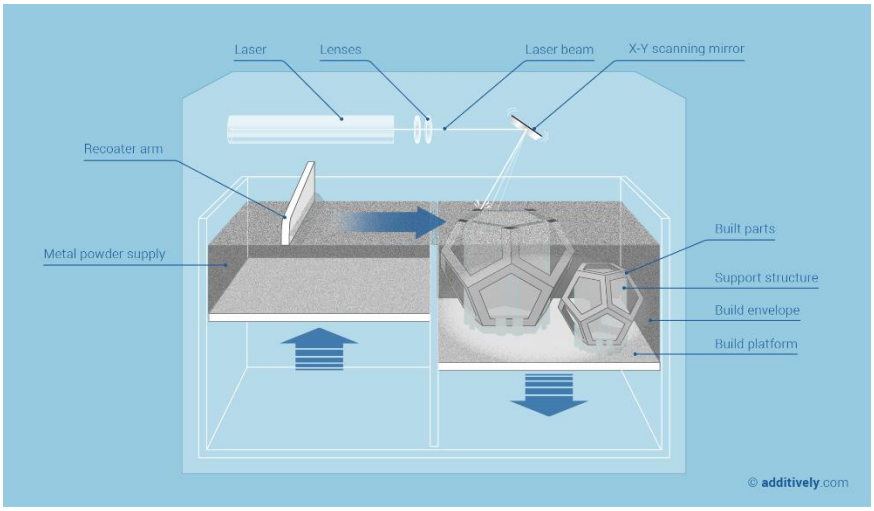

Figure 3: Schematic of SLM process ("Laser Melting - Additively," n.d.).

From a design perspective, additive manufacturing has mostly unlimited potential. However, SLM process parameters have been shown to significantly affect the resulting material microstructure and properties (Liverani, Toschi, Ceschini, & Fortunato, 2017). Common ranges for SLM parameters are indicated in Table II. It has been documented that a minimum 150 W power, 700 mm/s scan speed, and 0.07 mm hatch spacing is required to produce components of at least 98% density. Laser power is reported to have the

most significant effect on density. Ideal power input varies from material to material (Liverani et al., 2017).

Table 2: Process Parameter Ranges for SLM

Parameter	*Typical Range*
Laser Power	100 - 150 W
Laser Scan Speed	700 mm/s
Laser Beam Diameter	100 microns
Hatch Spacing	0.05 - 0.07 mm
Build Direction	45 - 90 degrees

Not all alloys can be processed with SLM. A key requirement is that the alloy must be weldable. Unweldable alloys will experience similar problems with SLM, including cracking, rapid oxidation, and others. Because SLM requires melting by nature, the elements of a particular alloy must also have similar melting points. If alloy constituent elements melt at significantly different temperatures, vaporization of one element can occur before the other element melts. Thus, highly complicated alloys are typically not printed with SLM. Sintering techniques instead may be used for these alloys, like tungsten-iron metals (Xuan Wang, Wraith, Burke, Rathbun, & DeVlugt, 2016). High carbon steels and super alloys can be difficult to produce with SLM due to vulnerability to thermal cracking caused by high cooling rates (Schmidt et al., 2017). The most common alloys printed with SLM, in descending order are as follows: Ni superalloys, Co-Cr alloys, tool and stainless steels, Ti alloys, and Al alloys (Gorsse, Hutchinson, Gouné, & Banerjee, 2017). Commonly, the properties of AM alloys differ from their conventionally produced counterparts (Figure 4).

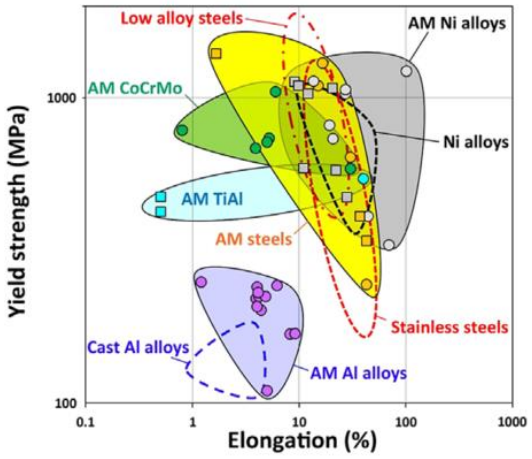

Figure 4: AM alloys compared to their conventional counterparts depict discrepancies (Gorsse et al., 2017).

This difference in properties represents a significant drawback to industrial adoption of selective laser melting. Although AM produced alloys are sometimes better than cast, or even wrought, alloys, the wide variability in properties presents a challenge. Metallurgical limitations, especially relating to the printed microstructure, are an important cause of these property variations. The understanding of design for additive manufacturing is extremely important, as good design can limit some of these drawbacks.

2.2 Design for Additive Manufacturing

The substantial development in additive manufacturing over recent years has largely focused on the manufacturing process itself. Engineering design, to accommodate such radically new and unique processes, must evolve substantially. Many conventional tenants of design for manufacturing and assembly (DfMA) do not apply to design for AM (DfAM). In addition, there exist new constraints that apply exclusively to AM focused design that must be learned and understood by design engineers. A significant theme of additive manufacturing is the freedom it enables designers. Small lot sizes and highly complex parts – uneconomical with conventional manufacturing – are made possible with AM technology. Unique shapes allow for weight and strength optimization and quick production times allow for rapid development. Although these advantages reduce the relevance of conventional DfMA, they also bring about new limitations that must be considered by design engineers (Thompson et al., 2016).

Like most modern engineering design, the process begins with computer assisted design. For AM, CAD is a requirement. Finalized digital CAD files are required by all AM processes to directly convert geometric information into movement of the deposition tool (the laser beam, in the case of SLM). This requirement means that design engineers must develop complete digital models of the final component, which is not always so for conventional manufacturing. Most CAD programs are intended for conventional manufacturing and allow for development of symmetric shapes with ease. These programs, however, do not enable the modeling of organic, complex, or stochastic shapes. New programs, like *Autodesk Fusion 360*, are working toward a solution. AM design engineers must grow comfortable with these new digital requirements to succeed with AM design. In many cases, design for AM actually implies re-designing an existing engineering component. Re-design for AM typically involves topology optimization accomplished with advanced simulation software (Hällgren, Pejryd, & Ekengren, 2016).

Another critical consideration is the build orientation during printing. This concept is important for a multitude of reasons. Parts produced with AM, especially SLM, are known for anisotropy. AN understanding of this anisotropy, from mechanical properties to surface roughness to microstructure, is extremely valuable so that its effects can be limited with careful design. With SLM, it is sometimes possible to re-melt upward facing surfaces by re-scanning the printed layer to improve the surface roughness. Design that aligns critical surfaces so that this technique is possible is necessary. Further consideration of the build direction is important due to required structure for mechanical support during printing. Designers must account for the intense thermal and mechanical stresses exhibited by the printed material by orienting the built component to withstand these forces. Removal of any support structure can be exceptionally difficult and risky after the build is complete.

Process parameters are specific at the material – and sometimes build – level. This means that design engineers must work with the AM technicians to ensure the designed component is possible with material specific limitations. Cooling rate, oxidation rate, and strength of the alloy in question must be considered before finalizing the design.

2.2.1 Lattice Structures

One unique capability of additive manufacturing is its ability to produce lattice structures. These low-weight, ordered components fulfill the criteria of conventional foams but allow for finer control over the processing. Cellular materials have historically provided engineers desirable properties such as high specific strength and high mechanical absorption. These unique materials have found use in many industries and for diverse motivations. In the aerospace industry, cellular materials are used for their low weight and increased area for thermal convection. For biomedical implants, cellular materials can be optimized for compatibility to bone structures (Mazur et al., 2016).

A consistent challenge in the manufacturing of cellular materials is the optimization of cell morphology for the selected application. Additive manufacturing has thus become a major solution to these longstanding issues. Selective Laser Melting can repeatably manufacture geometrically complex lattice structure with a high degree of customization, and at competitive prices. Lattice structures can naturally exhibit a wide range in properties when manufactured with SLM, so it is important to identify the ideal process parameters (Sing, Wiria, & Yeong, 2018).

The morphology of the lattice cells is of paramount importance to the resulting mechanical properties of the entire component. A few different approaches to determining ideal cell design have been pursued, including CAD and topology optimization (Mahmoud & Elbestawi, 2017). The cell design contributes to the plastic deformation mechanism, which is typically either bending or buckling. Traditional ductile stochastic foams are known to deform via the bending mechanism. Compression testing of different lattices have provided evidence that the bending mechanism is best suited to promote ductile behavior. Figure 5 presents a comparison of different cellular designs (S. J. Li et al., 2014).

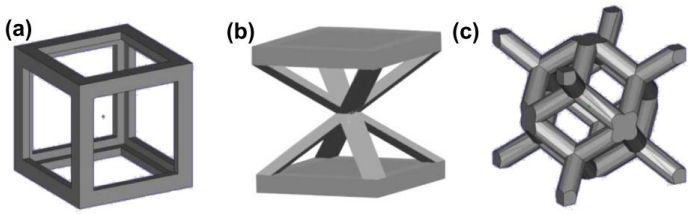

Figure 5: The cubic, G7, and rhombic dodecahedron lattice designs present different mechanical properties.

Angled struts, as seen in figure 5b and 5c, can prevent buckling and promote the bending deformation mechanism instead. This increases the ductility of the structure but comes at a loss of strength as well. Design of macro-sized components composed of these lattice structures can be exceptionally difficult with conventional CAD programs, so new tools are required. Software such as Element by nTopology has appeared in recent years to solve this issue.

2.3 Metallurgy and Microstructure

There are a few key features of the microstructures of metals produced from additive manufacturing that differentiate these components from those built with other processes. As a result of the rapid solidification process, the microstructure tends to be very fine, and anisotropic and metastable structures are common (Gorsse et al., 2017). Fine grains are a result of the fast cooling rates experienced during SLM. Columnar grain growth aligned with the build direction induces slight anisotropy in the z direction. Lastly, AM produced components typically contain a variety of different defects (EPMA, 2013). These defects are discussed in detail in section 1.4.

Because many AM methods use energy sources like those used in welding processes, the resultant structures are similar. The grain structure of printed metals is largely dependent on the geometry of the melt pool (DebRoy et al., 2018). Grain growth occurs perpendicular to the melt pool boundary, so the melt pool shape strongly affects the solidified structure (Figure 6).

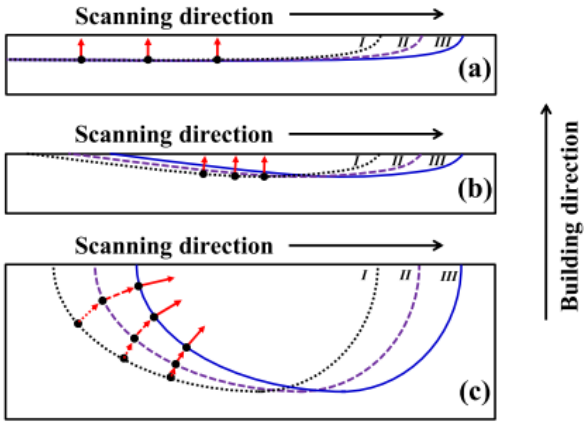

Figure 6: Grain growth depends on the geometry of the melt pool, which depends laser power and scanning speed (DebRoy et al., 2018).

As a result, vertically oriented grains are commonly observed in additively manufactured alloys (Saeidi, Gao, Zhong, & Shen, 2015). As indicated above, grain growth commonly occurs along the building direction, leading to anisotropy along the z axis. For SLM scan rates, the melt pool is nearly rectangular, as depicted in Figure 5a and b. Slower scan rates will produce a melt pool geometry closer to Figure 5c. the short and deep melt pool of 5c is characteristic of DED AM, whereas 5a and 5b are melt pool shapes

observed in powder bed fusion processes like SLM (DebRoy et al., 2018). In SLM processes, no nucleation occurs prior to grain growth if the prior layer temperature drops below the liquidus of the material, as it should with adequate laser power. Thus, grain growth will typically continue in the same direction layer-by-layer: epitaxial (Kou, 2003).

The solidified dendritic structure of Inconel 718 differs within different planes (Figure 7). Along the build direction, nearly vertical columnar grains can be observed. The cores of these dendritic structures are discernible orthogonal to the build direction. As in welding, the processing parameters are responsible for the microstructures that develop during selective laser melting (Figure 8). The laser power and scan speed espcially contribute to the resulting thermal properties during the print process (Figure 9). These properties also control the development of grain size and type. Although columnar grains are common, equiaxed grains are also observed in SLM materials. Mixed grain structures form because equiaxed grains nucleate and grow on partially melted powder while columnar grains grow epitaxially from the base of the melt pool (DebRoy et al., 2018).

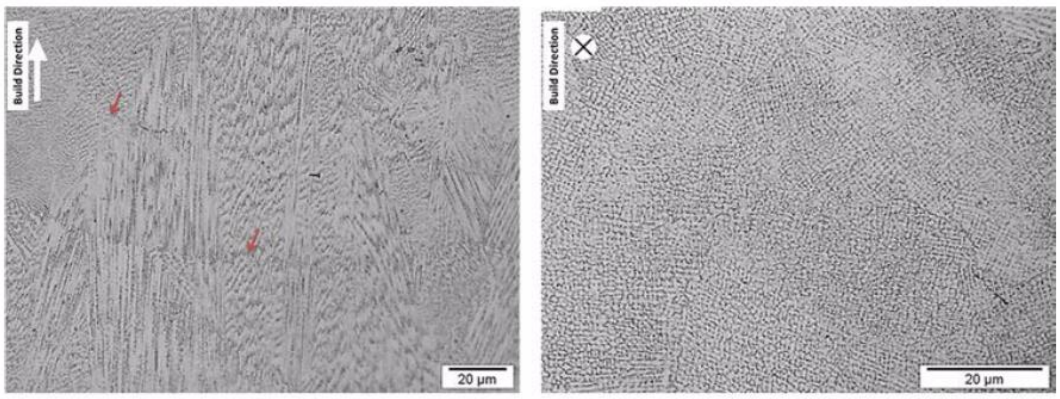

Figure 7: Microstructural images of SLM Inconel 718 reveals the solidification structures (Raghavan et al., 2016).

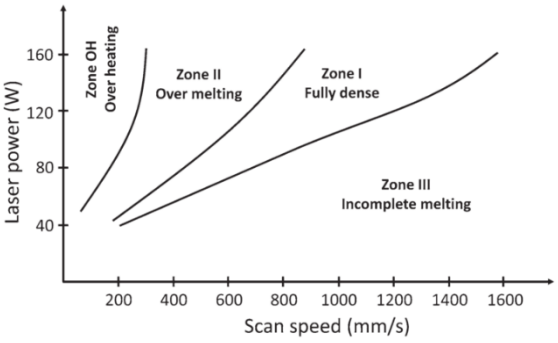

Figure 8: The proper energy input levels for SLM, in this case Ti64, depend on laser power and scan speed. Only the zone I microstructure will be right for the ideal properties. Defects and porosity will occur in zones II, III, and OH (Gong, Rafi, Gu, Starr, & Stucker, 2014).

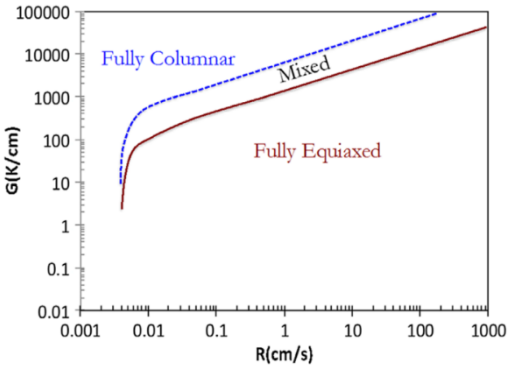

Figure 9: The thermal gradient G and the cooling velocity R are products of the energy input and material printed, also Ti64 here (Kobryn & Semiatin, 2003).

Some alloys, including 316L stainless steel, yield metastable cellular microstructures when manufactured via SLM. The formation mechanisms of these abnormal microstructures are not particularly well understood (Prashanth & Eckert, 2017).

2.3.1 316L Metallurgy and Microstructure

The following experiment concerns the SLM printing and processing of 316L stainless steel components, so a background of both wrought and as-printed properties of the alloy is valuable. 316 is a chromium-nickel-molybdenum austenitic stainless steel that finds use in the marine, medical, and food industries for its corrosion resistance and mechanical properties. The chromium content provides the corrosion resistance and the molybdenum provides the chloride pitting resistance (Table III).

Table 3: 316L Stainless Steel Composition

Cr	Mo	Ni	C	Mn	P	S	N	Si	Fe
16-18%	2-3%	10-14%	0.03%	2%	0.045%	0.03%	0.1%	0.75%	Balance

The addition of Ni to the microstructure stabilizes the austenite phase at room temperature. Austenitic stainless steels are typically vulnerable to sensitization, a phenomenon in which chromium is deleted from the grains and forms chromium carbide at the grain boundaries. This effectively decreases the corrosion

resistance of the material and is commonly encountered during heat treatments and welding operations. Decreasing the carbon content of 316 to produce 316L does mitigate this concern. The L variant of 316 means low carbon (Uns & Nr, 2014). The weldability and corrosion resistance of 316 L thus makes it an excellent candidate for manufacture via selective laser melting.

The microstructure of 316L produced with SLM differs substantially from that of conventional wrought material. Annealed 316L contains large austenitic grains (Figure 10).

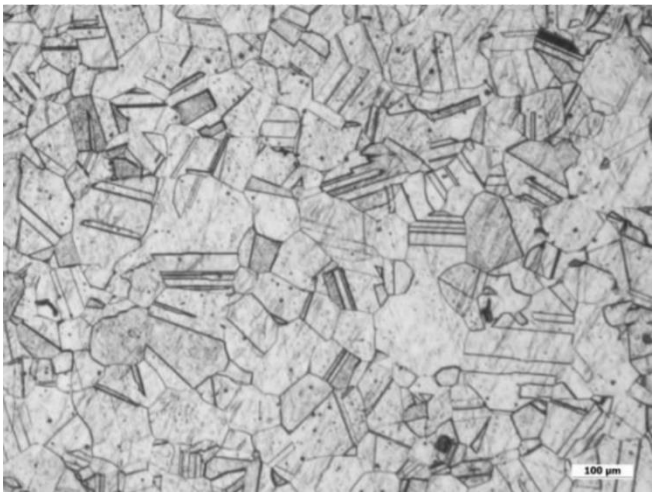

Figure 10: The microstructure of wrought 316 contains large austenitic grains (Dr. Shashank Shektar, 2012).

Several other features are present in the highly complex microstructure of SLM 316, including solidification lines, epitaxial grains, and ferritic phases. Solidification bands are easily observable along the SLM build direction (Figure 11).

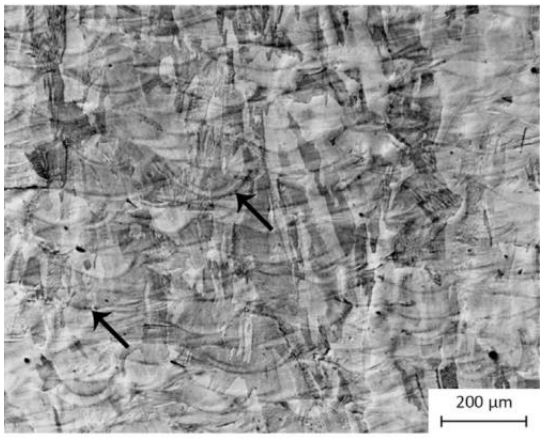

Figure 11: The black arrows indicate the solidification lines from the various weld pools from the laser energy input, layer by layer.

Note that in Figure 11 grains are discernible throughout the structure. The complex sub-grain structure is only revealed at high magnifications, however. The fast cooling rates associated with SLM can yield metastable cellular microstructures, which are complex. These microstructures are common in SLM 316L (Figure 12).

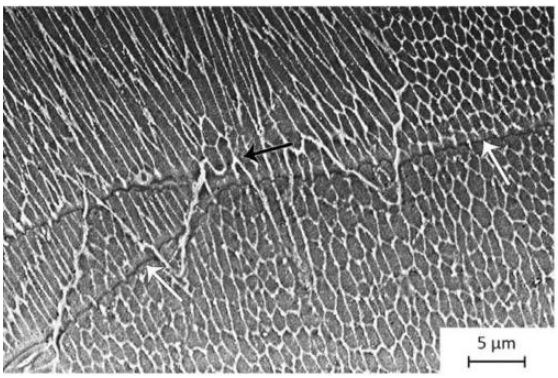

Figure 12: Small cellular austenitic grains are surrounded by delta-ferrite in this backscatter SEM image of SLM 316L (Kurzynowski, Gruber, Stopyra, Kuźnicka, & Chlebus, 2018).

Although a precise explanation for these microstructures has not been established, three key alloy requirements for the formation have been identified. First, binary alloy systems are preferred. In multicomponent systems, only two phases will form in the resulting structure. Second, the solute must have low solubility in the solvent. Last, the solute phase should have a much higher solubility in the solvent (Prashanth & Eckert, 2017). These metallurgical concepts combined with the exceptionally fast cooling rates of SLM can produce intense vortices in the melt pool which segregate certain elements from the primary phase and ultimately form this cellular pattern. The mechanism for this vortex formation has been identified as Benard Marangoni Surface Instability, which is characterized as convection caused by intense surface gradients. For 316L, this means that the ferritic stabilizing elements, like Mo, Cr, and Si, are ejected from the boundaries of the cells during vortex flow.

2.4 Metallurgical Limitations

Like any new and promising technology, limitations exist. Additive manufacturing is no exception. Some reports note the high cost of AM processes for high production while other drawbacks are related to

variations in mechanical properties. However, the mechanical properties of AM produced materials are not always inferior to those produced through traditional techniques. For example, *Lawrence Livermore National Laboratory* has reported SLM produced 316 stainless steel components stronger than common cast or wrought 316 ("Lab researchers achieve breakthrough […]" n.d.). Nonetheless, variation in the properties of SLM alloys from build to build is a concern. Defect formation occurs during the melting, solidification, and cooling periods. The mechanisms during the melt pool are quite complex (Figure 13).

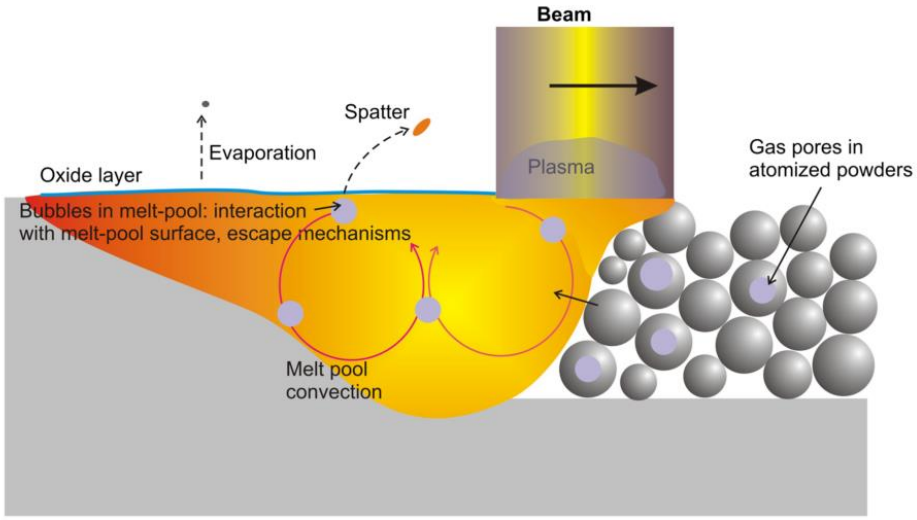

Figure 13: Evaporation, spatter, and trapped gasses are a few ways metallurgical defects can form during the SLM process (Hebert, 2016).

From the materials science standpoint, surface roughness, porosity, and residual stresses represent the most significant metallurgical challenges. Other observed issues, such as cracking and delamination, are results of these three problems (Schmidt et al., 2017). Porosity issues can be solved or mitigated with hot isostatic pressing (HIP) and residual stresses can be removed with heat treatment. The issues of surface roughness, however, have remained particularly persistent. Although traditional methods are possible, complicated geometries limit successful surface finishing (Schmidt et al., 2017).

2.4.1 Surface Roughness

Surfaces of selective laser melted metallic components are commonly irregular due to inherent process limitations (Townsend, Senin, Blunt, Leach, & Taylor, 2016). Two sources of surface roughness are identified from the powder bed fusion process. The staircase effect is a product of the layer-by-layer production process and is exhibited on all surfaces except for flat horizontal features (Figure 14). The other source of roughness is the powder itself, which contributes irregularity due to the shape and size of the spherical powder material (Schmidt et al., 2017).

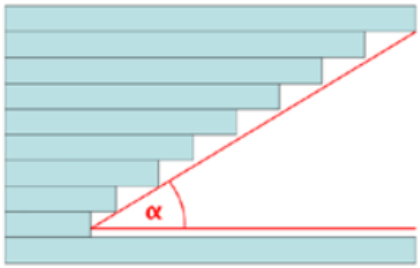

Figure 14: Angled surfaces will produce the so-called "staircase effect" where the layered nature of the built component exhibits a stair-like surface (EPMA, 2013).

Angles between 5° and 30° are typically most vulnerable to forming the stair-like surface morphology (Kaddar, 2010). This pattern contributes to the overall surface roughness and is a result of the component design and SLM process. Careful design can lessen the effect formation, but post-processing is nonetheless typically required to improve the finish.

Unlike the staircase effect, surface roughness due to powder is primarily affected by the process parameters. Unmelted or partially melted powder particles cause the development of high surface roughness. The particle size distribution and laser beam energy are significant factors in this effect. If the laser power is too low or particles too large, powder particles may not melt completely, leaving behind surface defects. Completely unmelted particles might adhere to the softened laser beamed surface. This phenomenon is more pronounced on downfacing surfaces due to the effect of gravity causing partially melted powder to droop. The balling phenomenon too can occur if power is too low. However, if laser power is too high, vaporization of powder material can occur due to high temperatures. This produces the so-called “keyholes”, which yields spattering and porosity issues (Hebert, 2016). Balling and keyhole

phenomena are discussed in detail in section 1.4.2. Surface roughness has shown to negatively affect mechanical properties, especially strength and elongation at break (Schmidt et al., 2017).

There are different numerical indicators of surface roughness, including R_a, R_z, and R_q. R_a, commonly used for its resistance to outliers, is the arithmetic average of the profile heights and valleys. R_q is the root mean square of the topography and R_z is the distance between the maximum and minimum peaks (Precision Devices, Inc., 2013). Typical R_a surface roughness measurements of SLM built alloys are 10-12 μm (Sachdeva, Singh, & Sharma, n.d.). Numerous varied surface roughness measurement techniques exist, too. These techniques are either tactile or optical, with optical methods yielding more accurate surface images but tactile methods producing more repeatable measurements at a faster pace. As a result, tactile methods using a contact needle to measure the surface profile are most common (Launhardt et al., 2016).

2.4.2 Porosity

Porosity is typically observed in SLM manufactured parts with near-spherical pores of diameter 100 μm or less (B. Zhang, Li, & Bai, 2017). Porosity defects are produced from a variety of different mechanisms. Common sources of porosity are entrapped gasses, powder pores, and keyhole collapse (Figure 15). Trapped gasses between particles or within particles generate pores as indicated in Figure 4. Lack of fusion defects (LOF) are usually classified as a separate issue due to their non-spherical shapes (Tang,

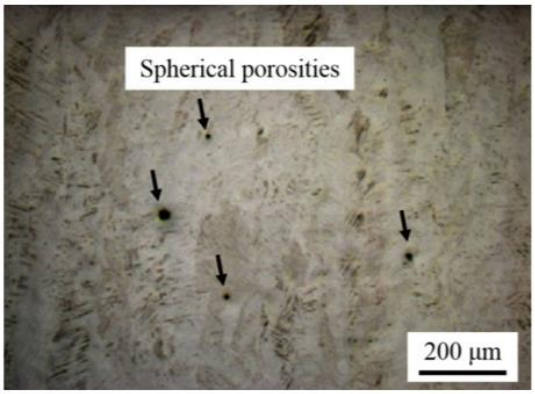

Figure 15: Pores are typically roughly spherical in shape, caused from gasses that are produced or trapped from a variety of different mechanisms (B. Zhang et al., 2017).

2017). LOF defects occur when the energy input is too low and areas between scanning tracks of the laser cannot melt completely (Figure 16).

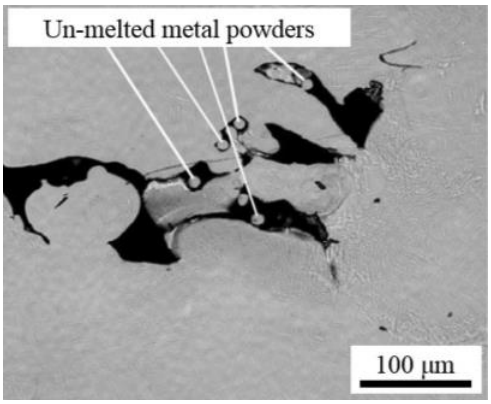

Figure 16: Lack of fusion defects form when energy is insufficient to completely melt powder particles (Q. C. Liu et al., 2014).

Hot isostatic pressing (HIP) post-processing can increase the density of the printed component (EPMA, 2013). The two laser-related sources for the formation of voids within SLM built components are excessive energy density and insufficient energy density (Kasperovich, Haubrich, Gussone, & Requena, 2016).

Excessive laser energy density can vaporize powder, producing pores from the keyhole effect, which is also observed in laser welding processes. The keyhole effect is complex and not particularly well understood due to its difficulty to directly observe. Experiments with transparent materials, such as glass and ice, have yielded insight however. Pores form from bubbles that separate during the keyhole collapse cycle (Figure 17). Figure 18 depicts the resulting defect after solidification. Laser power and scanning speed are largely correlated with keyhole-induced porosity. Experiments have indicated that increased laser power and decreased scanning speed increase the probability of pore formation from the keyhole effect (Xu, Rong, Huang, Wang, & Wang, 2018).

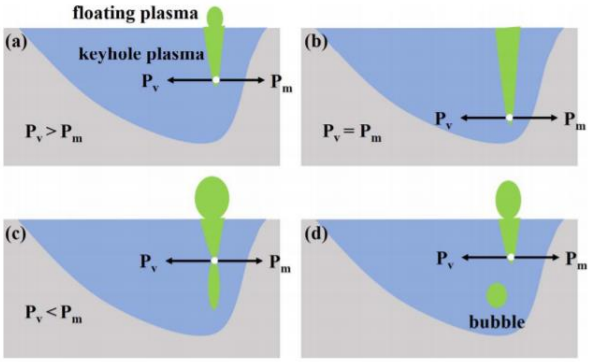

Figure 17: The keyhole collapse cycle causes the formation of a bubble as the keyhole vapor pressure (Pv) rises, but is then overcome by the molten pool pressure, Pm (Xu et al., 2018).

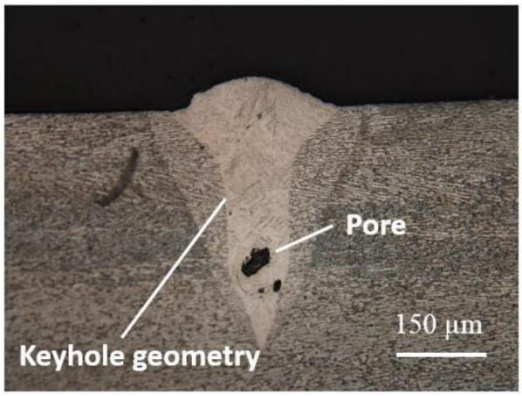

Figure 18: Microscopy image of Ti64 indicates a pore formed from the keyhole mechanism (Gong et al., n.d.).

Pores that form from the keyhole affect can develop ripples that act as stress concentrators (Figure 19). These pores develop this particular shape due to intense surface tension and shear forces on the rapidly cooling liquid (Kasperovich et al., 2016).

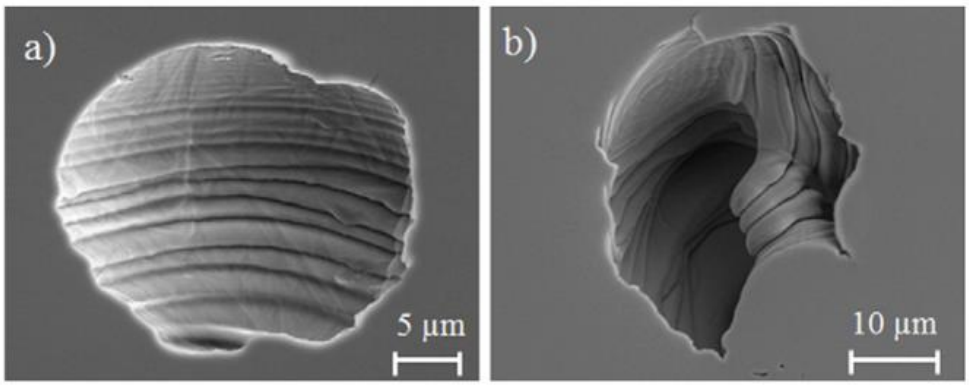

Figure 19: The rippling effect in these circular pores is a product of the shear forces induced from excess laser energy (Kasperovich et al., 2016).

Similarly, low laser power and fast scanning speeds produce porosity. LOF defects result from these parameters as well. Balling, another defect mechanism, is a source of both porosity and surface roughness. The balling effect can be caused by insufficient energy input (Gong et al., n.d.). Balling is driven by surface tension; under the right conditions, the melt pool will transition from a half-cylinder bead to a sphere to reduce surface energy (Sames, List, Pannala, Dehoff, & Babu, 2016). This mechanism forms melt balls, which induces cavities within the structure and roughness on the surface (Figure 20).

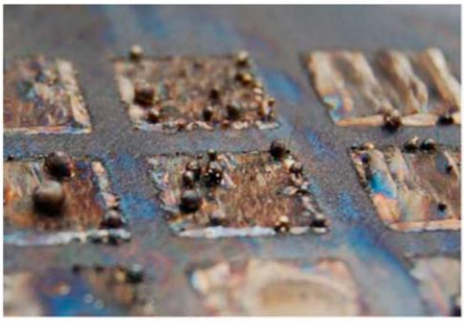

Figure 20: Balling is a phenomenon driven by surface tension wherein the melt pool transitions into a sphere to reduce surface energy (Sames et al., 2016).

Although keyhole-induced pores can be detrimental to mechanical properties due to ripple formation, pores caused from insufficient energy density are typically less spherical, producing more significant negative effects on mechanical properties (Kasperovich et al., 2016). Balling promotes the formation irregularly shaped microscopic cavities, yielding porosity, and also contributes to surface roughness and further delamination and cracking issues (Zhou, Liu, Zhang, Shen, & Liu, 2015).

2.4.3 Residual Stresses

The development of residual tensile stresses between printed layers in SLM produced components is an often-reported limitation of the manufacturing process. These stresses form due to two different mechanisms: thermal gradient and cooling phase (Simson, Emmel, Dwars, & Böhm, 2017). Laser processes, such as SLM or soldering, induce high temperature gradients that lead to residual stress formation. These mechanisms are similar to those observed in stress development in welds. During the SLM process, when the heat source (the laser) is removed, the heated material cools and contracts, while

the surrounding material does not, causing thermal stresses to develop into residual tensile stresses (Salmi, Atzeni, Iuliano, & Galati, 2017). This process is schematically detailed in Figure 21.

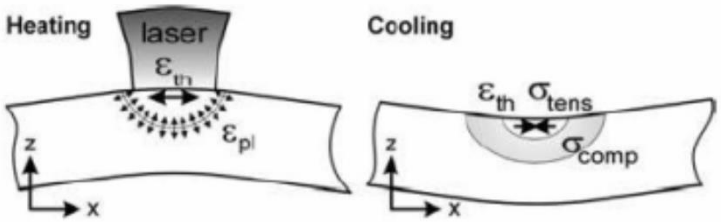

Figure 21: The Thermal Gradient Mechanism (TGM) and cooling times produce the residual stresses observed in SLM built components between layers (Mercelis & Kruth, 2006).

The development of residual tensile stresses is not only detrimental to the mechanical properties of SLM components, but can also lead to part warpage, cracking, and delamination during printing (C. Li, Liu, & Guo, 2016). Delamination and cracking during printing prevents use of the component and is thus a significant boundary to additive manufacturing technology (Figure 22).

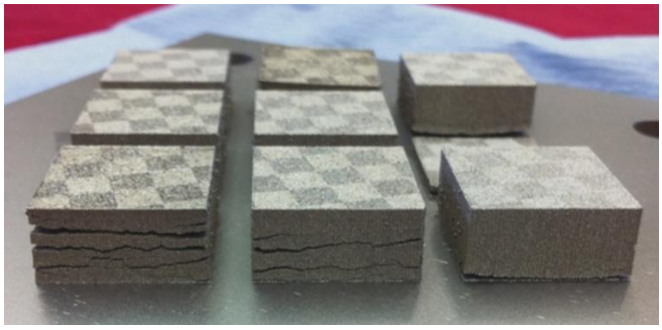

Figure 22: An experiment on the effect of base plate heating on preventing delamination of M2 high speed steel reveals significant differences (Kempen et al., 2011).

2.5 Post-Processing

The post-processing of SLM components is required for a multitude of reasons. Post-processing operations range from simple powder removal via compressed air to component heat treatments (Hebert, 2016). Due to the aforementioned metallurgical issues, heat treatments and surface finishing

operations are exceptionally important. Some techniques exist that can improve the surface roughness, release residual stresses, or collapse pores within the structure. Hot isostatic pressing is commonly used to reduce porosity (Lavery et al., 2017). Laser polishing, electropolishing, and peening are a few adopted solutions for improving surface roughness (EPMA, 2013). The AM surface roughness issue has nonetheless proven difficult to unilaterally solve, so new potential solutions are in development. Two aspects of the problem require attention: the polishing of interior surfaces, and the development of a single process to solve all defect related post-processing concerns. Chemical-abrasive flow polishing, tested on Inconel 625 components, has proven useful for finishing of interior surfaces (Mohammadian, Turenne, & Brailovski, 2017). A more conventional process, known as abrasive flow machining (AFM), has also gained recognition for aerospace and automotive components and may be a new asset to the additive manufacturing post-processing toolset. Ultrasonic surface treatments, such as ultrasonic shot peening (USP) and ultrasonic nanocrystal surface modification (UNSM) partially solve numerous defect issues, leading the development of a universal post-processing method. Each of these processes are explored in detail in the subsequent sections.

2.5.1 Ultrasonic Shot Peening

Ultrasonic shot peening is a variation of the conventional shot peening process. The primary difference from conventional shot peening is the way the energy is translated to the peening media. Rather than air, gravity, or turbine rotation, USP accelerates the media by vibrating a surface at ultrasonic frequencies of 20 kHz or more (Tricoire, 2016). USP can be used with a handheld device or with a larger chamber (Figure 23).

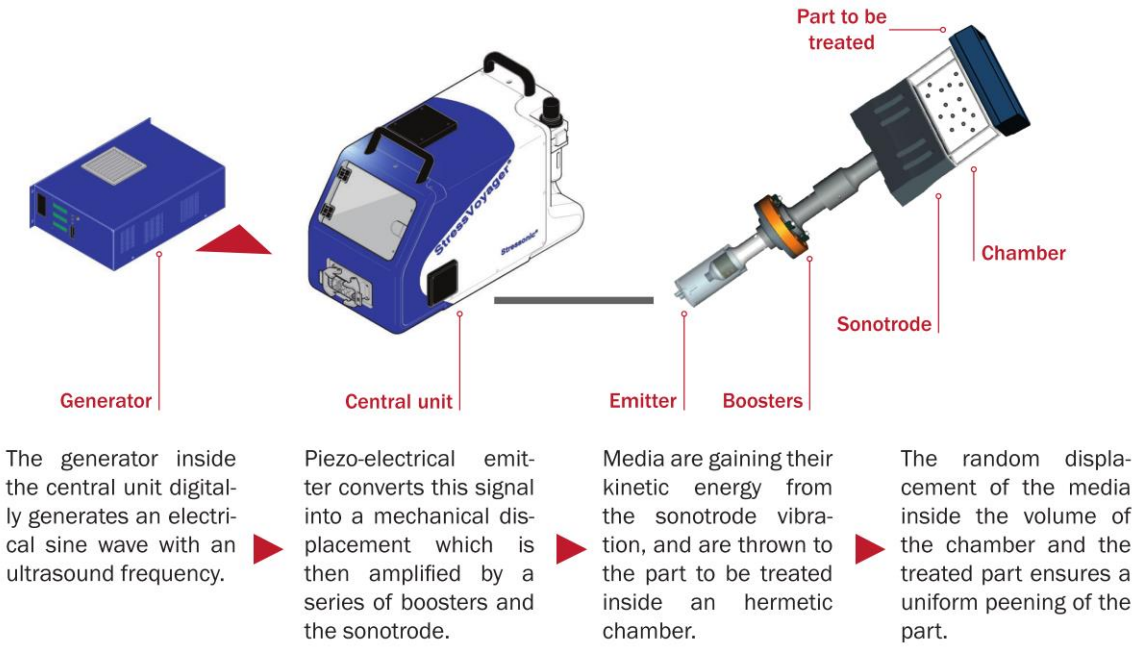

Figure 23: The USP process begins with the generation of ultrasonic frequencies, which are converted to mechanical displacement via a piezo-electrical emitter (Tricoire, 2016).

The USP process can be used to improve the surface roughness of SLM fabricated parts (Figure 24). The effects of the process on surface roughness is controlled by shot diameter and peening duration (Zhu et al., 2017). In addition to improving the surface roughness to some extent, USP is useful for its ability to produce nanocrystalline grains through severe plastic deformation (G. Liu, Lu, & Lu, 2000). After USP treatment, grains near the surface are smaller (Figure 25). USP can also convert residual tensile stresses into compressive stresses, making the process historically useful for improving the strength of welds (Presentation, n.d.).

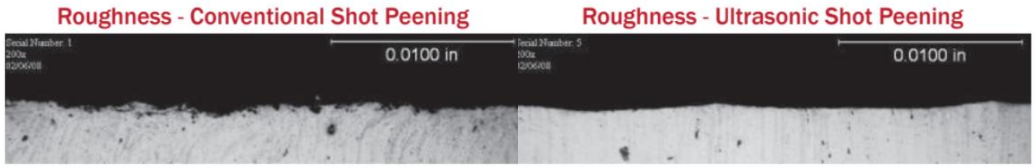

Figure 24: Empowering Technologies' USP technology finishes the surface better than conventional shot peening does(Presentation, n.d.).

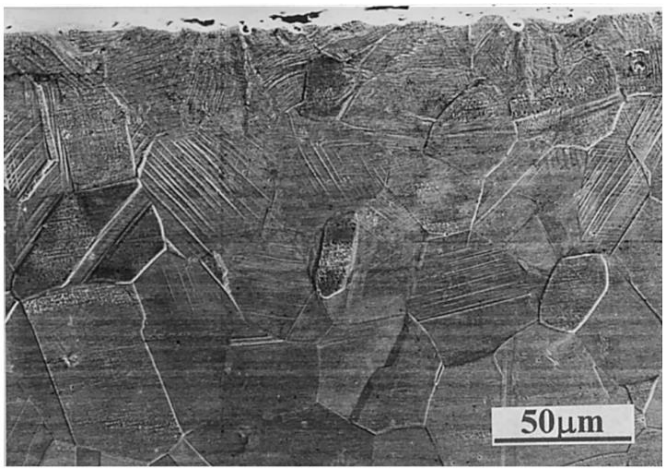

Figure 25: Grains near the surface of this USP treated 316 stainless steel are significantly smaller due to severe plastic deformation (G. Liu et al., 2000).

According to the Hall-Petch effect, smaller grain size yields higher strength – so USP induces a hardening effect on the surface layer of the treated component (Hummel, 1999). Nanosized grains form through severe plastic deformation (SPD) and subsequent recrystallization. This mechanism is similar to a traditional cold work and annealing process, but USP transfers enough energy to initiate the recrystallization phase (M. Zhang et al., 2016). Ultrasonic nanocrystal surface modification is a similar process to USP, but makes use of a scanning workpiece tip, instead of shot media (Figure 26).

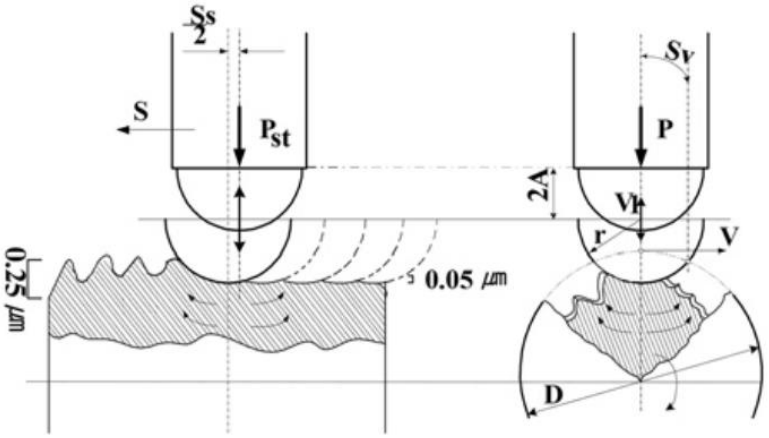

Figure 26: The hard tip of the UNSM device scans across the surface of the material, improving roughness (Amanov & Pyun, n.d.).

The UNSM process attracts industry and academic attention due to its precise control via process parameters. Typical UNSM process parameters are shown in Table III (Amanov & Pyun, n.d.).

Table 4: UNSM Processing Parameters

Parameter	*Typical Range*
Frequency	20 kHz
Amplitude	100 microns
Impact Load	200 Newtons
Tip Diameter	1 to 6 mm
Tip Material	WC, Silicon Nitride

Like USP, UNSM induces nanosized grains through severe plastic deformation. The precisely scanning tungsten carbide or silicon nitride tip supposedly improves surface roughness more significantly than USP does (Figure 27).

The UNSM device has even been used during the SLM fabrication process, to prevent columnar grain growth, collapse porosity, and convert residual tensile stresses into compressive stresses (Figure 28).

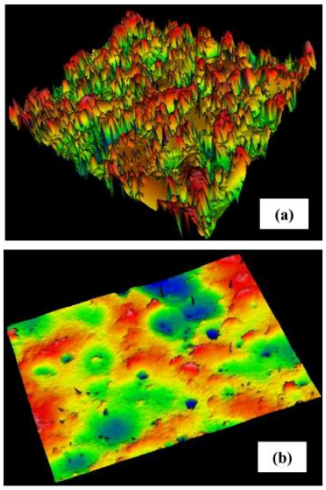

Figure 27: UNSM treatment of an aluminum alloy improved the surface roughness from a) 18 µm Ra to b) 3.5 µm Ra (Ma, Dong, & Ye, 2016).

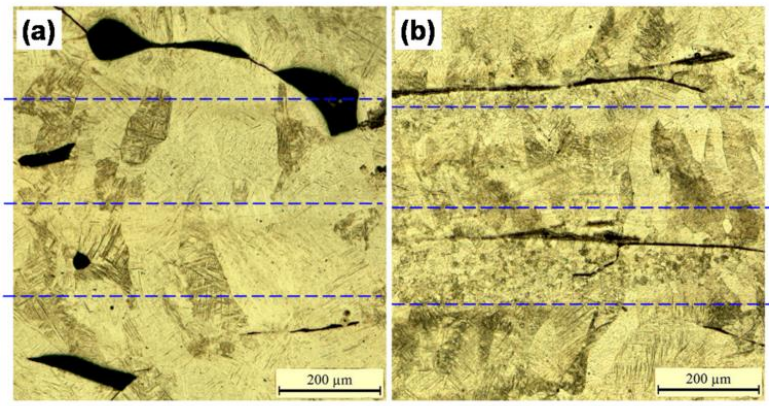

Figure 28: UNSM assisted SLM collapses pores between layers and improves the grain structure of the printed material (M. Zhang et al., 2016).

UNSM has shown particular usefulness in the treatment of titanium alloys, where it has allowed for the precipitation of α in β-type Ti-Nb-Ta-Zr (Kheradmandfard et al., 2017). The primary drawback of UNSM compared to USP is its inability to access interior component surfaces. If UNSM is conducted during the SLM process between layers, however, this issue may be solved. UNSM likely requires further development before it is close to feasibility for industry-wide post-processing of AM components. USP, however, may be ready for wide implementation.

2.5.2 Abrasive Flow Machining

A major limitation for most surface finishing technologies is lack of accessibility for interior surfaces and geometrically complex features. Advanced finishing processes, like abrasive flow machining, are thus required to solve these issues. The process was first invented by *Extrude Hone Corporation* in the 1960s. Today, the finishing method is commonly used for the aerospace and automotive industries, where surface finish is critical (Kumar & Hiremath, 2016). For additive manufacturing, a technique that promises components of complex geometries, AFM has proven to be a potential solution that can handle intricate interior surfaces (Xuanping Wang, Fu, & Gao, n.d.). Surface finish can be improved dramatically with the AFM process (Figure 29).

Figure 29: A fully AFM finished part ("ABRASIVE FLOW MACHINING (AFM) - Extrude Hone").

The three aspects of the abrasive flow operation are the machine, tooling, and abrasive medium (Rhoades, 1991). Three main categories of AFM exist: one-way, two-way, and orbital AFM. These categories refer to the motion of the abrasive media, either in one or two directions, or through orbital vibrations. A general schematic of the two-way finishing technique is shown in Figure 30.

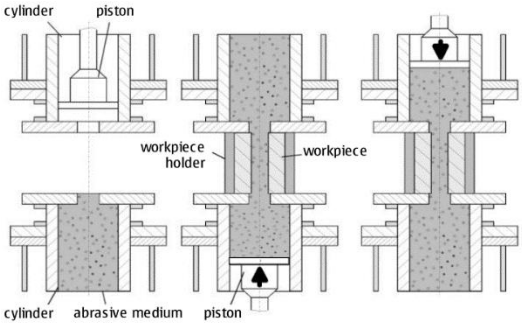

Figure 30: Abrasive media is pushed through the workpiece with a piston, gradually polishing the workpiece until desired finish is achieved (Uhlmann, Schmiedel, & Wendler, 2015).

The AFM process can be relatively fast but requires many cycles to reach the desired surface finish requirements. The material removal rate is dependent on the following factors: media flow rate, viscosity, abrasive size, abrasive concentration, workpiece hardness ("ABRASIVE FLOW MACHINING (AFM) - Extrude Hone").

After a few passes, the surface roughness improves significantly, but complete finishing requires many passes (Figure 31). Key AFM process parameters are shown in Table V (Kumar & Hiremath, 2016).

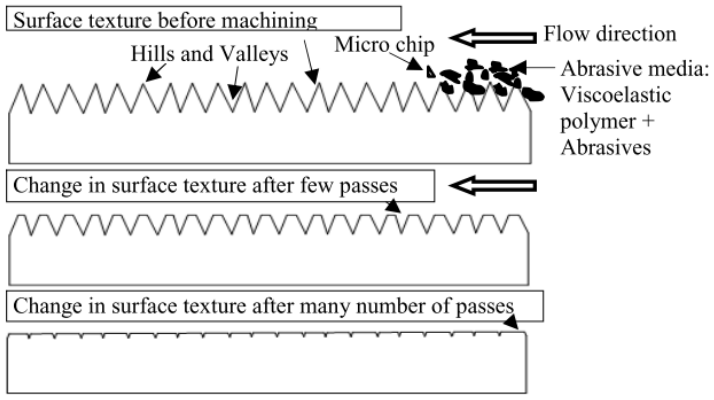

Figure 31: The hills and valleys that contribute to poor surface roughness are quickly cut down after a few passes, but many passes are required to reach the desired finish (Kumar & Hiremath, 2016).

A valuable attribute of abrasive flow machining is its ability to remove the peaks of the surface texture to improve the finish without deepening the valleys. This fact implies that it may be possible to achieve an ideal finish by removing only Rz, that is, the distance from the peaks to the valleys. If this is accurate, the material removal from AFM may prove predictable enough for mechanical design purposes.

Table 5: AFM Process Parameters

Machine	***Medium***	***Workpiece***
• Extrusion Pressure • Number of Cycles	• Rheological properties of media • Type of abrasive • Abrasive mesh size • Concentration of abrasives and carrier • Types of polymer carrier • Additives	• Material • Hardness • Geometry • Initial surface finish • Surface texture

An *Extrude Hone* two-way AFM machine is shown in Figure 32. It is a simple machine to operate but may require fixtures to properly polish certain areas. Plastic fixtures can be quickly machined or 3D printed to properly position the metal component to be finished. The high hardness and angularity of SiC particles mean that these particles are suitable for polishing of a wide variety of different metals, including steel, copper, nickel, and titanium alloys (Figure 33).

Figure 32: A two-way Extrude Hone AFM machine at the Extrude Hone facility in Paramount, CA. Note the abrasive media resting on the base plate.

Abrasive Media

The abrasive media utilized for the AFM process affects the processing time and effects. The medium is a viscoelastic polymer containing abrasive particles, which remove material from the workpiece via cutting action. AFM media is commercially available from *Extrude Hone Corporation* and *Kennametals*, but various researchers have also developed advanced abrasive media for the finishing technique (Kumar & Hiremath, 2016). AFM media compositions are indicated in Table VI.

Table 6: AFM Abrasive Media Compositions

Source	***Polymer***	***Abrasive***	***Abrasive Concentration***
(a. C. Wang, Liu, Liang, & Pai, 2007)	Silicone Rubber	SiC	50%
(Kar, Ravikumar, Tailor, Ramkumar, & Sathiyamoorthy, 2009a)	Natural Rubber	SiC	68%
(Kar, Ravikumar, Tailor, Ramkumar, & Sathiyamoorthy, 2009b)	Butyl Rubber	SiC	68%
(Ravi Sankar, Jain, Ramkumar, & Joshi, 2011)	Styrene Butadiene Rubber	SiC	NA*

* Not reported in this study.

SiC is the most common abrasive used in AFM media, as indicated above. SEM imaging shows the sharp edges of a SiC abrasive particle that yield the cutting action of the polishing process (Figure 33).

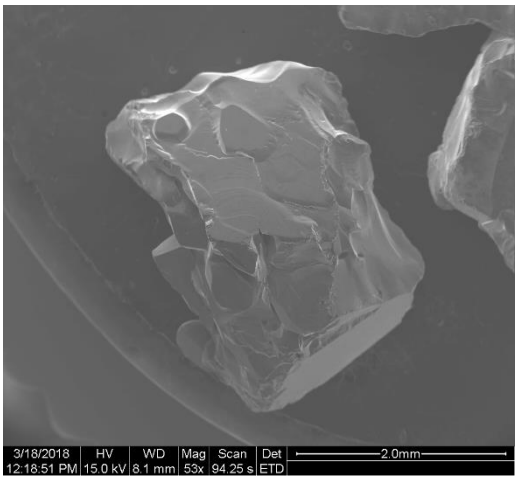

Figure 33: An 8-grit SiC particle, provided in a sample courtesy of Extrude Hone.

The polymer base is typically a type of rubber. Media compositions can commonly be used for different alloys and specific media batches are sometimes suitable for re-use on different components ("ABRASIVE FLOW MACHINING (AFM) - Extrude Hone"). AFM finishing, with the proper composition and processing parameters, has proved the possibility of reducing roughness to below 1 μm Ra (Venkatesh, Sharma, singh, & kumar, 2014).

Chapter III – Experiment Methodology

3.1 Scope

The goal of this thesis in Industrial Engineering is to investigate processes able to improve the surface condition of SLM built alloys. Abrasive flow machining and ultrasonic shot peening, detailed in the Literature Review, are explored in this study. AFM was pursued due to its ability to precisely polish complex interior surfaces whereas USP was explored for its directional versatility and superiority to conventional peening processes. All prints were built with stainless steel 316L powder with the SLM Solutions 125 machine. Results of this study can and should be extrapolated to other alloys, where appropriate. More information on 316 is given in section 2.3.1. The primary surface property measured herein is surface roughness, in both Ra and Rz form. Dimensional measurements must also be conducted to understand how much material is removed from each process. Designing adequate test coupons to evaluate these processes was challenging, as there exists no accepted coupon design standard for additive manufacturing evaluations. In addition, for abrasive flow machining, the ability to remove excess and parasitic powder particles from an internal lattice design, without compromising strength, was investigated. This concept is tangentially related to improving the surface finish. The goal is a reduction of mass by removing parasitic powder particles without compromising the strength of the lattice. For ultrasonic shot peening, the change in hardness from as-built samples was also examined. Lastly, the ability of USP to remove support structure stubs from supported downfacing surfaces is also of interest.

3.2 Primary Sample Design

Test coupon designs from literature were investigated prior to initial sample design conceptualization (Townsend et al., 2016). Figure 34 depicts four unique designs that each presented advantages and disadvantages for the context of this experiment.

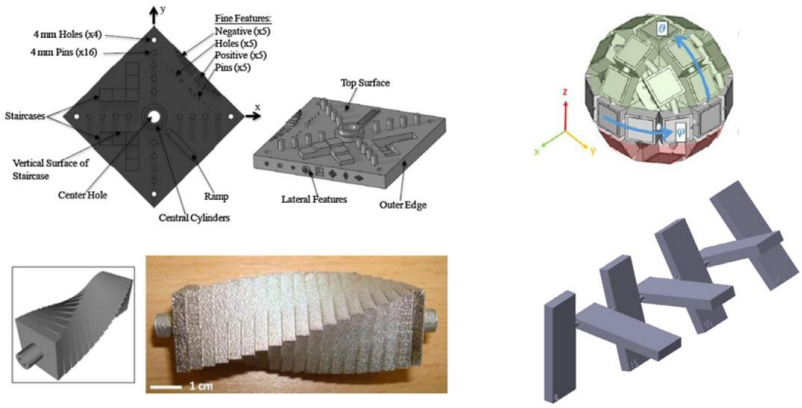

Figure 34: Clockwise from Top-Left: NIST, Faceted Sphere, Surface Inspection, Truncheon

These four coupons each represented different benefits and drawbacks. The NIST proposed design is excellent for its wide variety of small external and interior features, but there is hardly any investigation into angled surfaces or complex internal passages. The faceted sphere would yield excellent data for the surface roughness as a result of build angle but includes no internal features. For this study, it is important that internal features are thoroughly investigated, as it is known that that is the primary advantage of AFM. The surface inspection design allows for a look at angled features, and its sparing use of material mean the print will be rather quick. The truncheon design, of the four designs, was advantageous for its variety of surface angles, along with a large area on either face for internal passages. The truncheon design thus served as the primary inspiration for the development of the first test coupon.

The first and second iterations of the design were quite simple (Figure 35). The use of rotating shapes allowed for the incorporation of different angles, without the large mass required by the longer truncheon design. An internal passage through the center of each face allowed for the investigation of internal features.

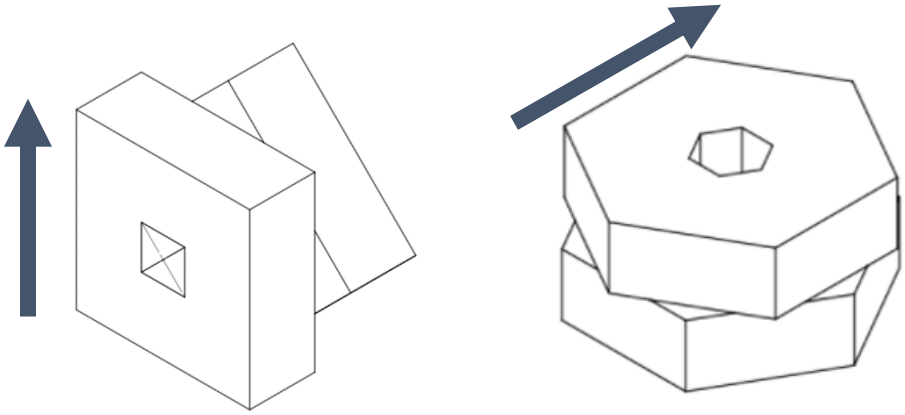

Figure 35: First iteration (left) included three different angles (0, 90, 45) along with an internal passage. The second iteration (right) utilized hexagonal features to replicate the first design, but with more angles. Note the arrows denoting the build direction for each.

An issue with both designs is the lack of a flat base for resting on the build plate. With only one internal feature, the potential data set from AFM testing is too small compared to USP testing. Thus, it became known that further iterations of the design would require more internal passageways. In a study on abrasive flow machining of additively manufactured material, a grille surface design was utilized (Figure 36).

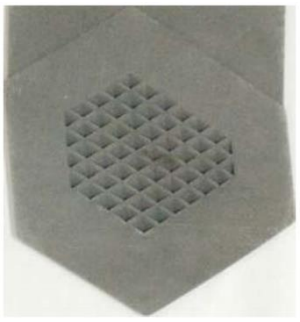

Figure 36: SLM as-printed grille to be polished with abrasive flow machining (Xuanping Wang et al., n.d.).

Although these interior features are not complex, the grille design does present an excellent use of surface space. This design yields substantial internal area for surface analysis. So, the hexagonal second iteration design was adapted to include a flat bottom for printing, a grille-like face design, and complex internal features (Figure 37).

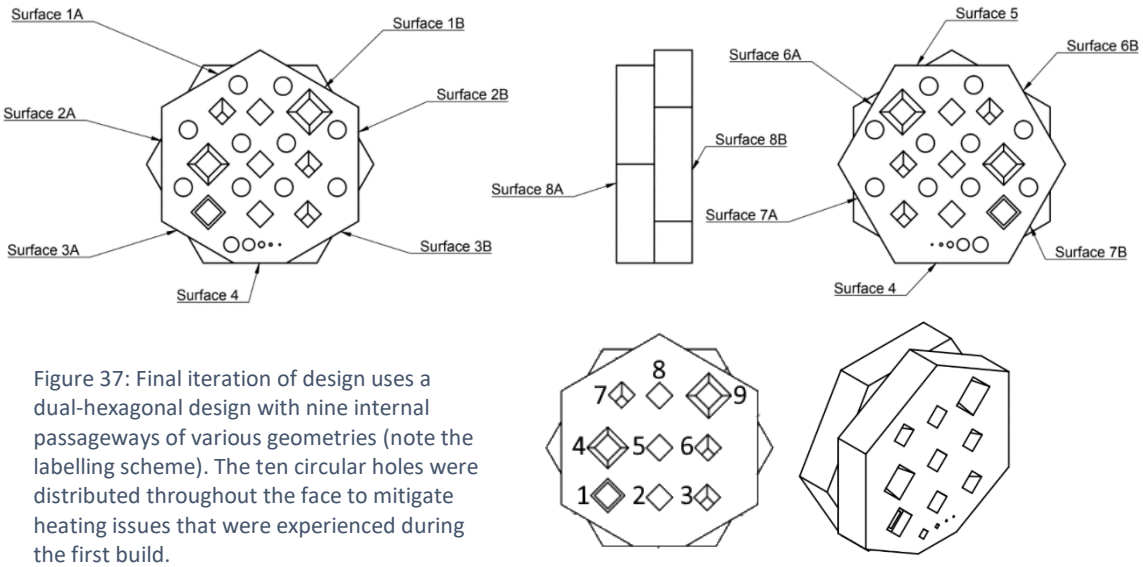

Figure 37: Final iteration of design uses a dual-hexagonal design with nine internal passageways of various geometries (note the labelling scheme). The ten circular holes were distributed throughout the face to mitigate heating issues that were experienced during the first build.

The final design incorporates eight different surface types, denoted 1-8. Where replicate angles are present, A and B are used for the naming convention. The 30^{o} downfacing surfaces (surfaces 3A and 3B) require support material for mechanical support. Surfaces 7A and 7B initially did not use any support structure, but this was added later after a failed build to serve as a heat sink. For reference, the height of the build is 1.8 inches, and the thickness is 1 inch. A detailed part drawing is included in the appendix. There are nine different internal passageways that use contracting, expanding, bent, straight, or stepped geometries. Some include internal cavities. Figure 38 depicts all nine of these features in detail.

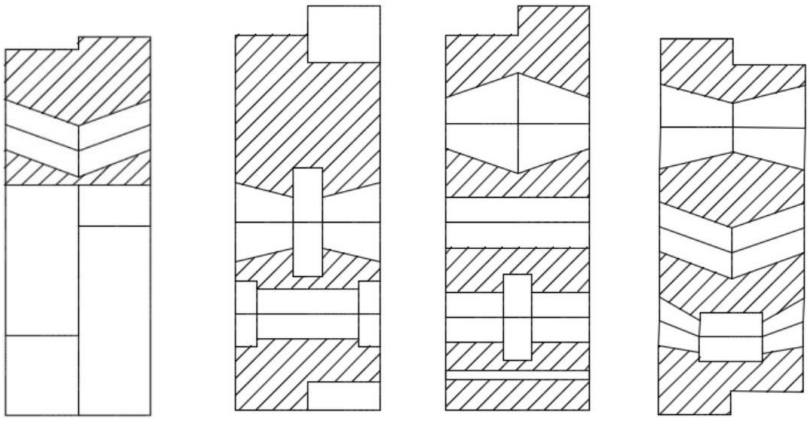

Figure 38: Section views for all nine passageways show the variety of internal features.

These nine passageways were designed to challenge post-processing techniques by incorporating varying cross-sectional areas and difficult to reach internal chambers. After the test coupon design was finalized, a first build was attempted. Three test coupons were printed on one build plate, along with a 1 in^3 cube for a different study. The build failed due to recoater arm error, meaning the recoater arm impacted the part at some point during the build. Upon investigation of the failed components, it is clear that the failure was a result of thermal distortion caused by excessive heating (Figure 39).

Figure 39: Recoater arm impacted the curled-up area indicated by the circle. Recoater movement direction is indicated by the arrow. There is incomplete fill past the curled-up edge due to the inability of the recoater arm to push powder into this region of the build area.

To solve this issue, a few adjustments were made to prevent thermal distortion. Ten holes with support structure were distributed throughout the component. The support structure was not required for mechanical support, but rather to provide heat conduction channels down to the build plate. Because the conductivity of powder material is so low, the build plate must serve as a heat sink during the printing operation. The same methodology was applied to 60^{o} surface that was initially unsupported. Support structure was added here to increase thermal conduction. Lastly, recoater arm delay was increased by ten seconds, giving the material time to cool before the deposition of the next layer. The second build of just one test coupon (and a rectangular prism for a different study) was completed successfully (Figure 40).

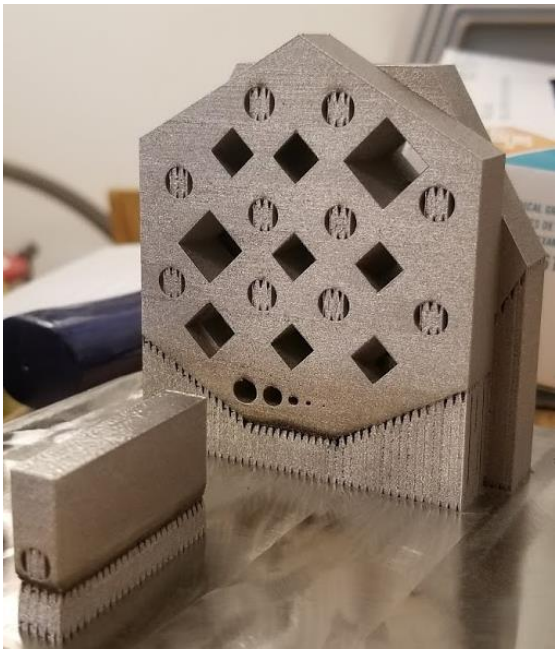

Figure 40: Successful completion of the first test coupon. No defects were observed, but there is a slight burning signature near the base of the build. This is due to the "up-skin" setting turned on for the rectangular part (for an unrelated study) leading to increased temperature on the double hexagon part.

After these necessary processing parameters were decided, the remaining test coupons were printed. All builds were removed from the build plate via band saw. Support structure was removed with hammer, chisel, and pliers. This sample is known as the double hexagon design and is one of two sample designs for the experiments of this thesis.

3.3 Thin Disk Lattice Fill Sample Design

A potential benefit of AFM worth investigating is its capability to process lattice filled structures. The use of lattice, rather than solid material, has been used to significantly reduce component weight while increasing the overall strength-weight ratio. In fact, lattice components can be seen as technology impossible without additive manufacturing production techniques. However, processing lattices can be especially challenging. The removal of excess powder and parasitic powder particles is a challenging issue. Removal of trapped powder is valuable for reducing the weight of the lattice component. Abrasive flow machining may be able to easily remove this trapped powder without damaging the struts that make up the lattice. Parasitic powder – powder partially melted or sintered to the surface of the lattice struts – may prove a bit more challenging to remove without damaging the lattice. For this specific experiment, surface roughness reduction is not of interest; the primary goal is to reduce weight by eliminating parasitic and excess powder without jeopardizing the strength of the lattice.

An adequate test coupon for this experiment will allow for the repeatable measurement of mass before and after AFM processing, as well as mechanical testing on polished/unpolished samples to evaluate any damage to the lattice struts. Because mass measurements are inherently repeatable, the difficulty in designing such a component comes from the need to produce reliable mechanical test measurements.

For the mechanical testing requirements, both tensile and compressive testing were considered. The advantage of tensile testing is that the design of standardized rectangular test coupons is inherently suitable for internal polishing. Thus, a first sample design iteration was produced (Figure 41). The most significant issues with this design were the potential inaccuracies introduced by the poor surface roughness of the exterior, and the long build times of such a tall component.

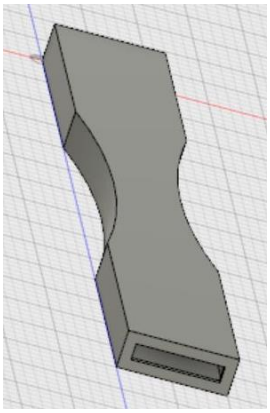

Figure 41: Basic tensile coupon design with hollow structure, allowing for lattice fill and AFM polishing.

Due to the drawbacks of the above tensile coupon design, coupons for compressive testing were also investigated. The ASTM compression testing standard requires cylindrical design with at least a one-inch height. However, thin disk specimens are best for this experiment, so the standard cannot be precisely followed. By incorporating the cylindrical shape, lattice fill, and orifices on each side for AFM media flow, the following design was produced (Figure 42).

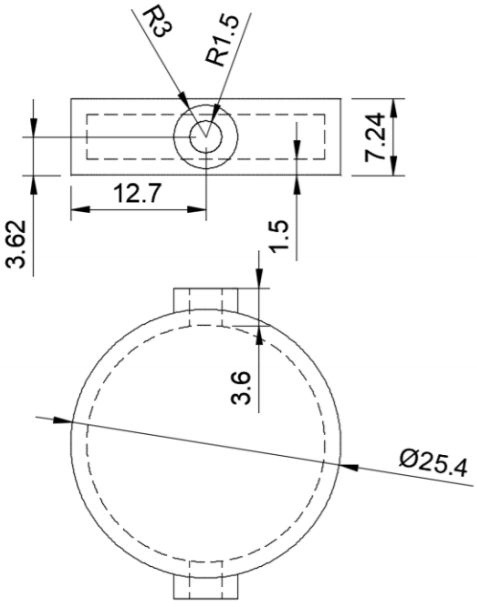

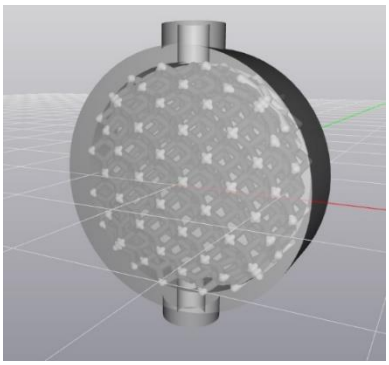

Figure 42: The thin hollow disk design incorporates lattice fill. The holes on either side allow for powder removal and AFM processing. Compression testing can be conducted on the parallel flat sides of the disk.

Although this design is not standardized, it is suitable for comparative datasets between the polished and unpolished samples. The surface roughness of the exterior is less of an issue for compression testing than it is for tensile testing. The disk area of the sample was filled with cubic fluorite lattice structure, generated with the Element Pro software from nTopology. The lattice strut diameter is 0.4 mm, leaving a 1 mm gap between struts. This lattice type was selected because its preferred failure mode is bending, rather than buckling – as detailed in section 2.2.1.

3.4 Experimental Design

Several variables are of interest in the evaluation of AFM and USP as finishing processes for SLM built materials. The reduction of surface roughness is of course of interest. Especially how the reduction relates to the surface angle and specific feature is of interest for this study. The literature review strongly suggests that AFM will reach a far lower Ra roughness than USP will, but there are other variables to consider. USP can finish external features well, and partially finish internal features. However, AFM finishing works best for internal features, so no attempt was made to polish external features.

Besides roughness, another important variable is the dimensional stability of the process. This analysis is somewhat subjective, as it is based not solely on the quantity of material removed, but also on the predictability of the material removal required for an ideal finish. A key distinction between AFM and USP here is that AFM removes material whereas USP merely compresses material on the surface. To compare dimensional stability, a computational measurement machine (CMM) was used to measure material removal from the surface after processing. Another key aspect of dimensional stability is potential morphology altering by the processes. AFM, as a flow driven process, may struggle to polish angular surfaces without rounding corners. Similar effects may be observed with USP processing of external corners. These characteristics will be investigated principally after processing.

Due to the differing nature of these two processes, there are some unique variables that are investigated for only one of the two processes. For AFM, the removal of excess powder and parasitic powder particles

from internal lattice features will also be investigated. This test requires the thin disk lattice filled part, which is only used for AFM testing. All other tests used the double hexagon component. For USP, the polishing of support structure stubs, left behind after support structure removal, is also of interest. This capability was not investigated with AFM due to the lack of support structure in the internal features of the double hexagon component.

In addition to the aforementioned testing, pre and post scanning electron microscopy (SEM) was conducted on the components to gain a visual understanding of the process effects at the microscopic level. Metallography in both the XY and XZ planes, where Z is the build direction, was performed to verify that the base microstructure is as expected for an SLM printed 316L stainless steel component. The results of these experiments follow in the next chapter – a preliminary experiment was first conducted on an as-built double hexagon to provide comparisons, while preserving time and resources, to the results of the AFM and USP experiments.

Chapter IV – Results

4.1 Preliminary Results

SEM images, CMM dimensional measurements, and profilometry surface roughness measurements were conducted before processing with either USP or AFM. In addition, optical and scanning electron microscopy was conducted on metallography specimens to verify microstructure. The results of this preliminary investigation are detailed in section 4.1 and used for baseline comparisons for the vast majority of the following experiments with both USP and AFM.

4.1.1 Profilometry

The surface roughness was measured with a Mitsuyo profilometer equipped with a needle stylus, using a cut-off length of 2.5 mm. The profilometer yielded two types of surface roughness measurements, Ra and Rz. Ra and Rz measurements were recorded for each of the surfaces of the hexagon, excluding the base and supported overhangs (3A, 3B, 7A, 7B, 4). Table VII presents the mean Ra and Rz measurements for each of these surfaces.

Table 7: Surface Roughness Measurements for Double-Hexagon Design

	1A	1B	2A	2B	5	6A	6B	8A	8B
Ra (µm)	14.76	13.20	16.08	12.91	5.16	16.02	16.25	13.45	13.45
Rz (µm)	98.14	88.01	98.19	79.66	25.54	100.87	100.57	82.70	78.94

It is immediately clear that surface 5, with a measured roughness of 5.16 µm Ra, is far less rough than the other surfaces. Because surface 5 is the top surface, it does not encounter the staircase effect and thus typically yields a better finish than the rest of the component. Additionally, the double hexagon coupons were built with the up-skin setting on, which re-melts top facing surfaces after the build is complete. The other observable differences are likely due to differences in surface angle, as well as differences in the relationship to the recoater direction. The roughness range (not including 5) is 12 to 17 µm Ra, which is

typical for as printed SLM components. One-way ANOVA, with surface type as the factor and surface measurement (both Ra and Rz) as dependent variable, indicates that there is a significant difference in surface roughness for different surface types. Fisher's Least Significant Difference method indicates how surface types should be grouped based on their surface roughness (Table VIII).

Table 8: Fisher LSD Grouping for Ra and Rz at 95% Confidence Level

Surface	Mean Ra (µm)	Grouping			Mean Rz (µm)	Grouping		
6B	16.25	A			100.57	A		
2A	16.08	A			98.19	A		
6A	16.02	A			100.87	A		
1A	14.76	A	B		98.14	A		
8A	13.45		B		82.70		B	
8B	13.45		B		78.94		B	
1B	13.20		B		88.01	A	B	
2B	12.91		B		79.66		B	
5	5.16			C	25.54			C

Slightly different grouping can be observed for Ra and Rz measurements. In both, surface 5 resides in its own group. However, there are statistically significant differences between groups of surface types. It is not clear from the results if the differences are a result of part angle or recoater angle. For this study, Ra data is the primary source of analysis. However, Rz measurements are particularly useful because these values can approximate the material removal requirements to achieve a good surface finish. This information is thus relevant for the forthcoming AFM experimentation.

Profilometry measurements were also conducted on interior passages of the as-built double hexagon test coupon. The part was first sectioned to allow for access to the walls of the passageways. Of the nine passages, only four were measured completely to preserve resources. All four sides of these four diamond-shaped passages were measured, yielding data points for two upward facing surfaces and two

downward facing surfaces. As predicted in the literature review, the surface roughness of the downward facing surfaces was significantly higher than that of the upward facing surfaces, as determined with ANOVA. The effect of passage type was also investigated and determined to not be significant. A boxplot representing these data is indicated in Figure 43.

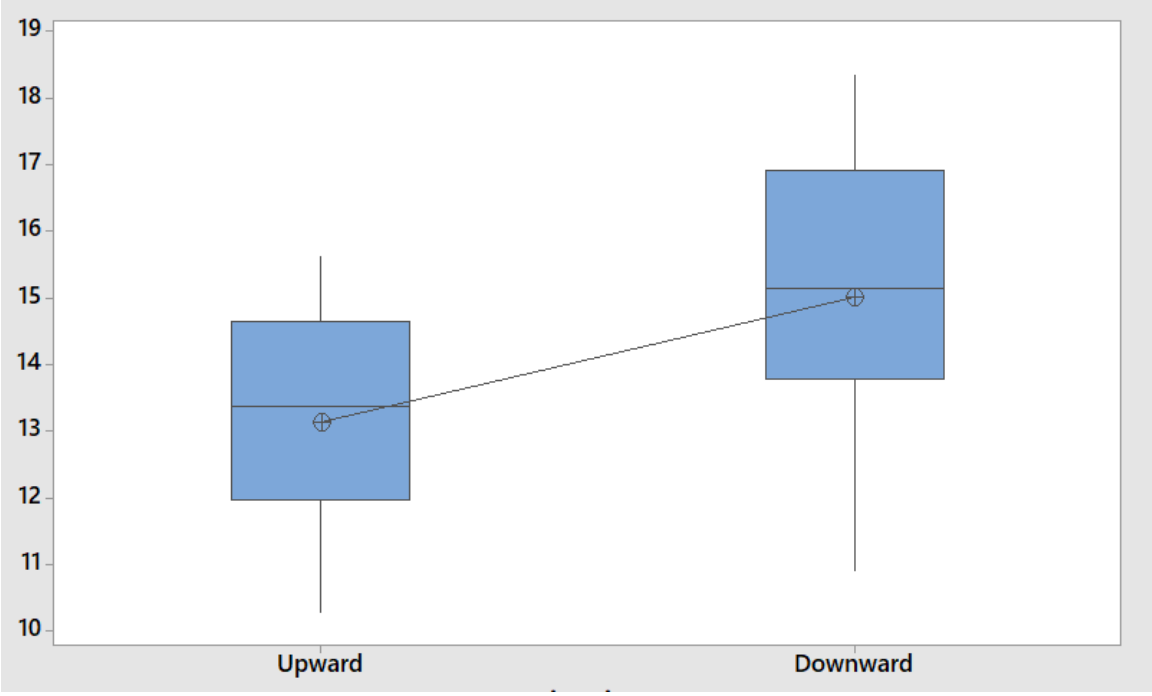

Figure 43: The downward facing surfaces indicate a higher surface roughness, 15.01 µm Ra, than the upward facing surfaces, 13.13 µm Ra. With a p-value of 0.001, this difference is statistically significant.

So, downward facing surfaces indeed yield a rougher surface than upward facing surfaces do and the location of the passage on this part (or its type or size) do not affect the roughness. These results are not unexpected, but to present an interesting challenge to overcome with AFM and USP processing of these internal passages. Because the upward and downward facing surfaces are significantly different, the polishing of these passages to a uniform surface finish without removing substantially different material from upward and downward surfaces will be exceptionally difficult.

4.1.2 Imaging

Scanning electron microscopy of the as-built double hexagon sample was conducted to investigate sources of surface roughness – overhanging powder particles and the staircase effect. As indicated by profilometry measurements, microscopy confirms the rougher surface of the downfacing surfaces (Figure 44).

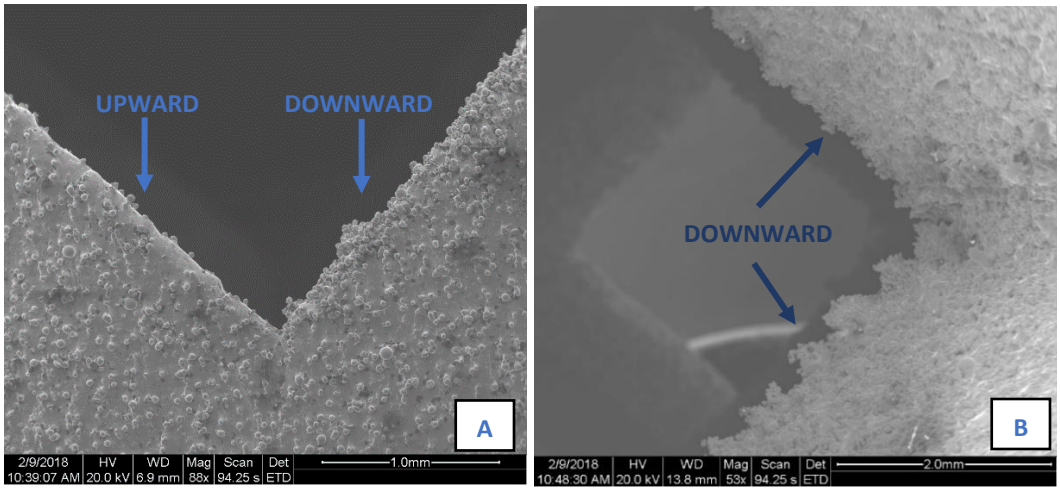

Figure 44: The staircase effect is not directly visible here. More parasitic overhanging powder particles exist on the downfacing surface, contributing to a rougher surface. Two different internal as-built passages are presented here to demonstrate the source of surface roughness, as well as the difference in roughness between upward and downward facing surfaces.

From these SEM images, it is difficult to conclude that the staircase effect is the source of this roughness. A slight staircase-like pattern can be observed on the upward facing surface, but on the downward facing surfaces, overhanging powder particles dominates as a source of surface roughness. In 44A, partially melted or sintered particles can also be seen on the forward-facing surface, 8A. The removal of these particles is of paramount importance in improving the surface finish these passages.

The computational measurement machine was also used in an attempt to accurately measure the critical dimensions of these passageways before processing. However, reliable and repeatable measurements on a component with this scale of roughness was not impossible. Image data was gathered instead to provide a source of qualitative comparison after processing with either AFM or USP.

Characteristic CMM images of two passages are provided (Figure 45)

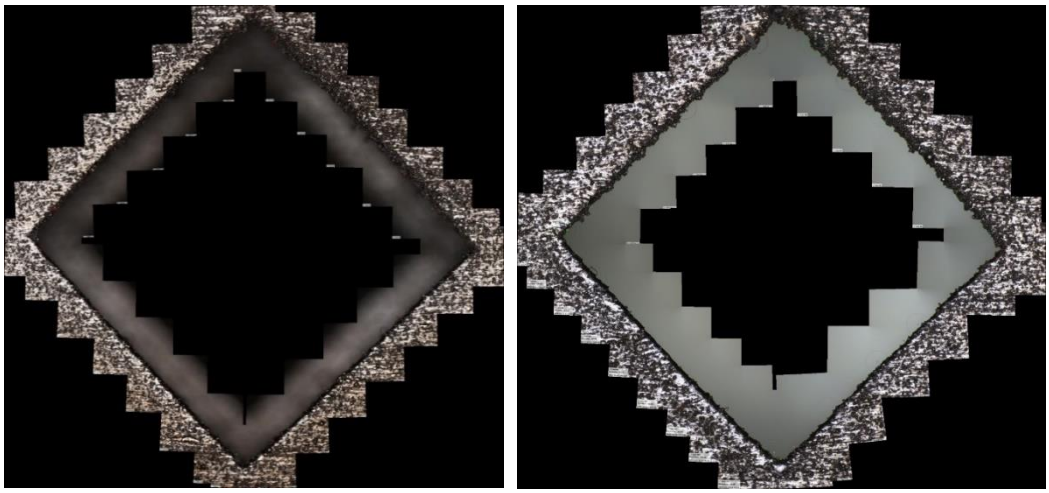

Figure 45: From these images, it is clear why accurate dimensional measurements were not possible. The particles clinging to the surface hide the location of the true base material.

Arc measurements at the corners of these diamond shaped passages was also attempted; again, these measurements proved unreliable as a result of the parasitic particles clinging to the surface. It is not explicitly clear from these images to what extent the corners meet at a precise point. There does appear to be some rounding that occurred as a natural result of the SLM process.

4.1.3 Microstructure

Metallography was conducted on two specimens cut from a double hexagon test coupon to investigate the microstructure of the as-printed material. The XZ and XY planes were both examined to inspect the layered microstructure and microstructure within the layer, respectively (Z is the build direction). Polished Bakelite samples were electro-etched with 10% oxalic acid and a power supply set to 5V. The amperage varied between 0.5 and 0.7 amperes, depending on the area of the specimen. At low magnification in the XZ plane, the layered structure is visible (Figure 46).

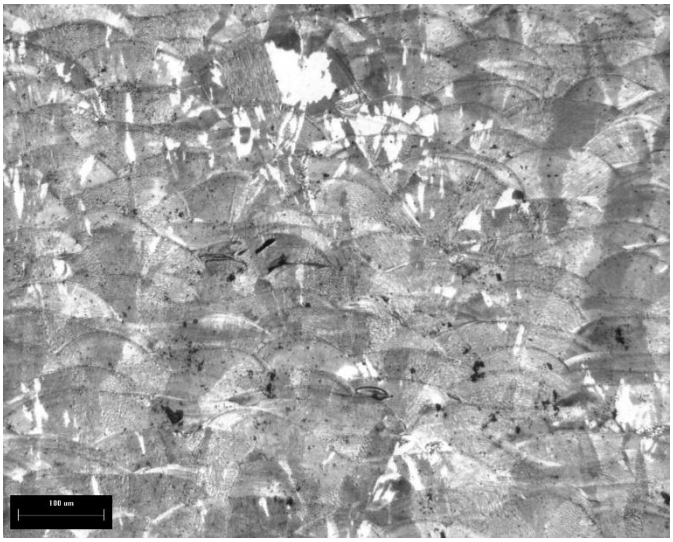

Figure 46: The layered structure of the SLM built material is visible in the form of semi-elliptical melt pools bordered by melt lines. Small dark areas denote LOF defects and pores. At 100x, individual sub-grains are not visible.

The semi-elliptical melt pool barriers are clearly visible here. The sub-grain size of SLM printed components is typically quite small; it is impossible to observe individual sub-grains at this magnification. Dark patches near the center of the image denote lack of fusion (LOF) defects. These are identifiable by their irregular shape – if they were pores, they would be circular. A closer look at one of these LOF defects is presented in Figure 47.

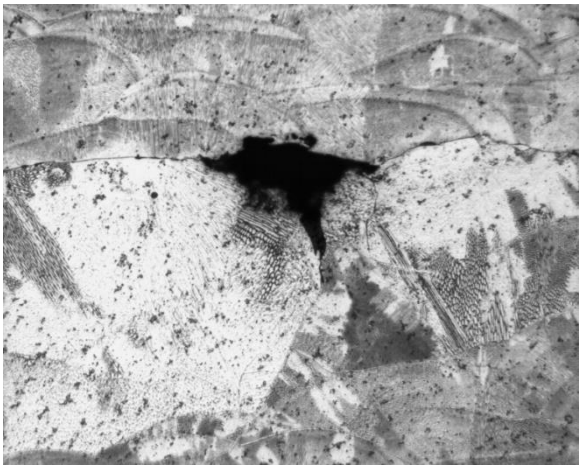

Figure 47: Cracks emanate from either side of the lack of fusion defect, which is ostensibly a stress concentration. At 200x magnification, the small cellular grains are slightly visible.

The irregular shape observed here signifies that this void must be due to lack of fusion. These are fairly common throughout a metal additively manufactured material and occur because of insufficient energy input or powder particles to form totally contiguous material. At this magnification, the cellular sub-grain structure begins to present itself. At even higher magnifications, the cellular microstructure is increasingly apparent (Figure 48).

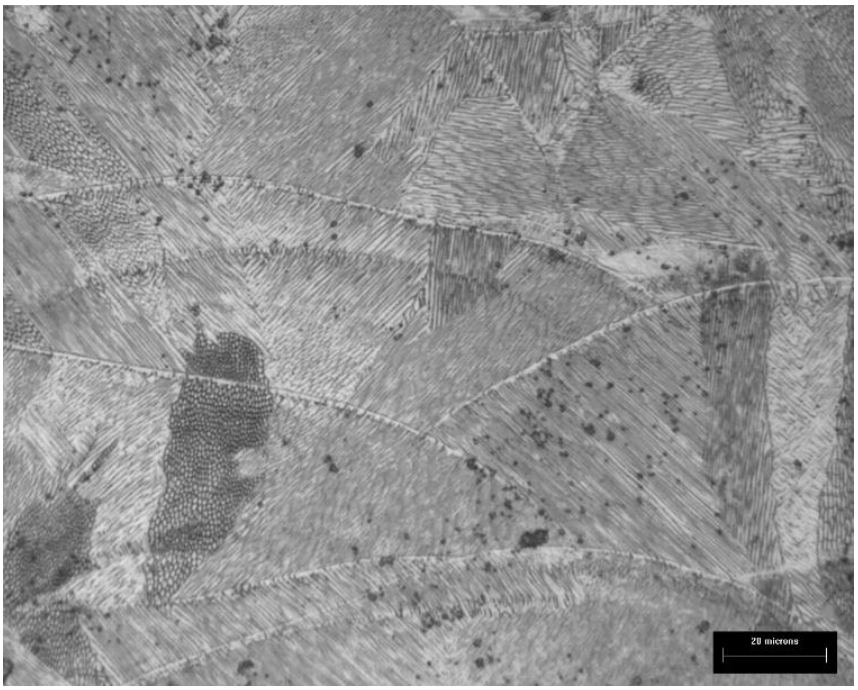

Figure 48: At 500x, the sub grain structure is clearly visible. Grains contain numerous sub-grains of equal orientation. Some epitaxial growth can be observed crossing melt lines, but epitaxial growth is not always the case.

Sub-grains are plainly visible at the 500x magnification. Interestingly, many elongated sub-grains group together to form larger grains. The metastable cellular microstructure, common for SLM 316L, is observable in these images. It is not explicitly clear which phases are present in these images, but the clear majority of the structure is surely austenitic, with ferrite stabilizers likely residing at grain boundaries. As discussed in section 2.3.1, this separation of the austenite phase from ferrite stabilizing elements is a result of intense vortex flow in the melt pool caused by surface tension gradients that are initiated from the high-power input and fast travel speed of the laser.

With SEM imaging at much higher magnifications, the sub-structure is even more apparent. A variety of SEM images were produced on the same sample (Figure 49).

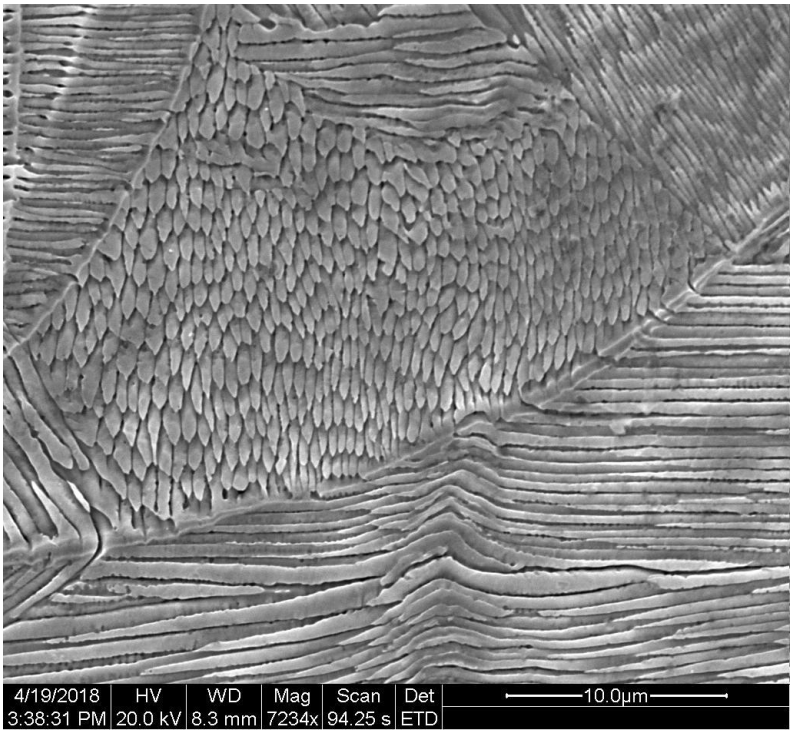

Figure 49: At 7234x, the sub-grain structure is finally fully visible. The grains are quite small in width - about 1 micron - but quite long. There are a variety of orientations, and grain colonies tend to be bordered by solidification lines from the laser path.

The dark areas between the grains represent the ferritic stabilizing elements that were ejected from the cooling austenite in the melt pool. The etch process most likely eliminated the delta ferrite, so the dark regions are actually areas where the ferrite material would have been. The cellular structure is reminiscent of a typical cast dendritic structure, but the SLM microstructure is nevertheless unique. Grains always contain many parallel elongated cellular sub-grains and adjacent grains always contain a

sub-grain structure of different orientation. In other areas of the same sample, epitaxial growth is apparent (Figure 50).

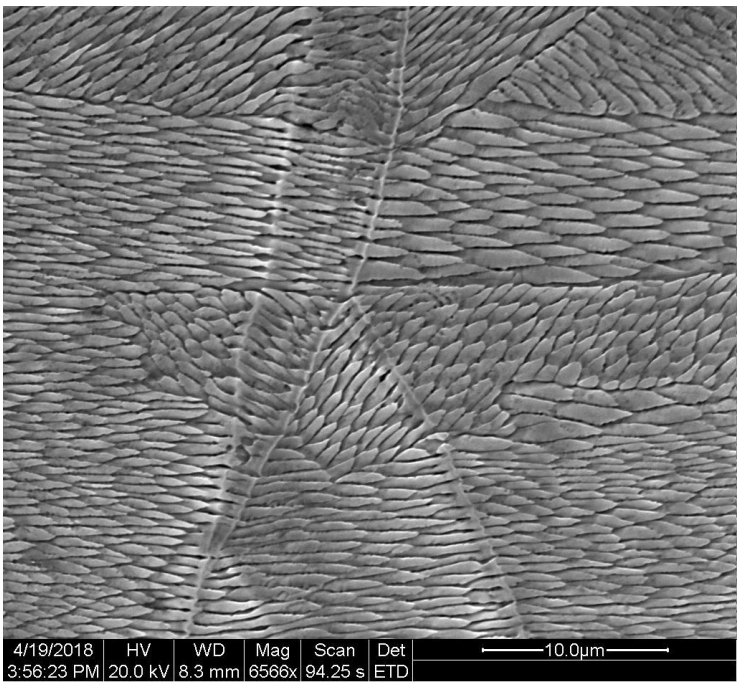

Figure 50: Epitaxial growth can be observed crossing solidification lines from layer to layer. Again, the grains here are about 1 micron in width, visible at 6566x.

Epitaxial growth of long, narrow grains is common in SLM alloys due to the energy input into the last solidified layer when a new layer of powder is melted. In the above images, there is epitaxial growth across nearly every solidification line, but this was not consistent across the entire microstructure.

A sample from the XY plane (within the layer) was also mounted, polished, and etched for metallography. The microstructure in the XY plane is similar to that of the XZ plane, but there is a notable lack of solidification lines, as these are only easily observable in the XZ and YZ planes (Figure 51). There also seems to be a higher degree of grains pointed out of the image (along the build direction for the XY plane). A higher concentration of build direction oriented grains is a phenomenon commonly observed in SLM manufactured alloys. The microstructure of SLM alloys contributes to its anisotropy. To illustrate this anisotropy, one image from the XY plane and two images from the XZ plane were modified to depict a three-dimensional micrograph of the selective laser melted 316L at about 4000x magnification (Figure 52).

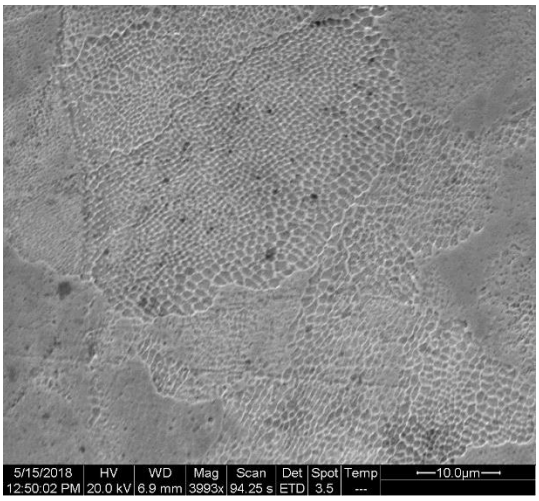

Figure 51: At 3993x, grains oriented along the Z direction are visible grouped into large colonies, much like the structure of the XZ plane.

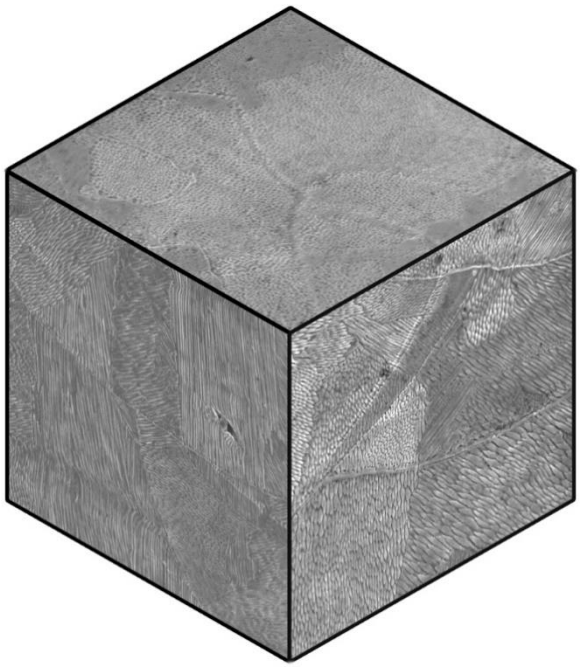

Figure 52: Three-dimensional micrograph at approximately 4000x.

Although the XY plane sample was also etched, the etching was performed at a shorter duration. Unlike the XZ plane samples, the areas between grains appear white, rather than dark. This indicates the presence of a ferritic phase or ferritic stabilizing elements at these boundaries. Over-etching of the XZ sample caused the disappearance of this phase, but in the XY sample, it remains.

4.2 Abrasive Flow Machining Results

Upon conclusion of the preliminary testing, a double hexagon sample coupon was sent out for abrasive flow machining at *Extrude Hone* in Paramount, California. For the double hexagon and thin disk lattice designs, process engineers at *Extrude Hone* decided on a particular resin type and abrasive particle size to fulfill the requirements of the part. For the double hexagon test coupon, AFM was performed with 856-54 resin with SiC abrasive particle. This resin is slightly more elastic than the typical resins for AFM and was used due to its ability to handle complex interior passages. Instead of polishing each internal passage at a

time, all nine passages were polished simultaneously to investigate effects of flow changes between the nine cavities. It would be possible to specifically tailor the process flow parameters for each passage, but that was not the goal of this study. Three thin disk lattice fill parts were polished with a medium-low viscosity resin with abrasive particles. Of these three, two were compression tested and one was sectioned for optical inspection. Three unfinished disks were compression tested and one unfinished disk was sectioned for comparison.

4.2.1 Double Hexagon Test Coupon

For this test, all nine passageways were polished at once. Due to the changing cross sections and differing sizes, each passage experienced a different flow rate. The component was fixtured such that the center holes were centered to the flow of the resin. Processing lasted about 45 minutes, when the technicians deemed it completed.

Computational Measuring Machine

Dimensional measurements of the processed sample were conducted with the MicroVu computer measuring machine to produce both quantitative measurements as well as image data. For each of the nine passageways through the double hexagon test coupon, diagonal measurements were produced and compared to the CAD digital model measurements. The deviation from the model measurements is reported with a series of boxplots (Figure 53).

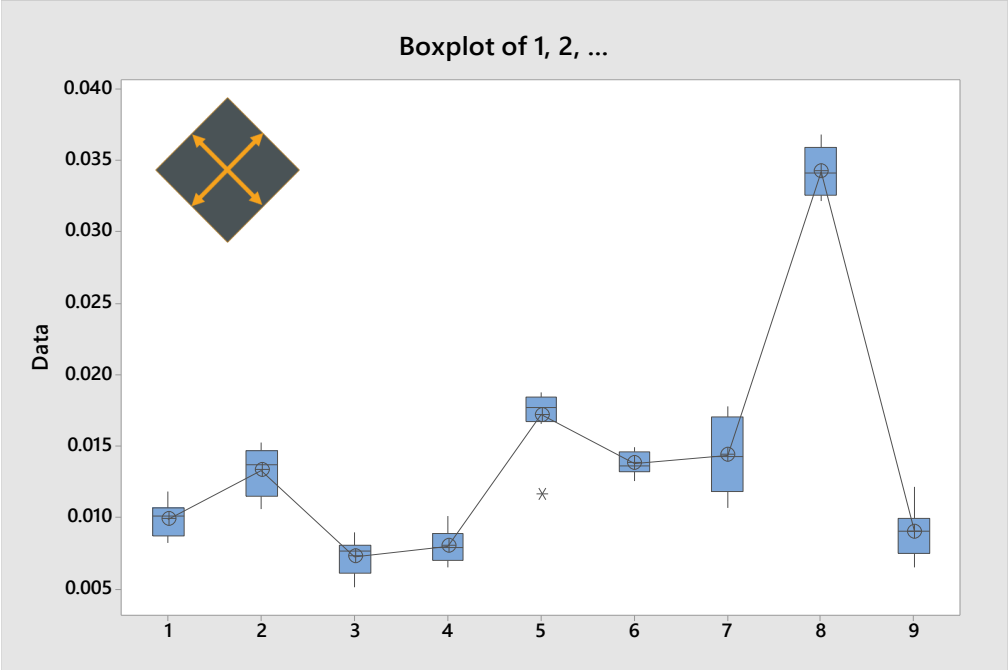

Figure 53: These boxplots depict the average deviation from the model after AFM processing.

All nine passages expanded in size as a result of AFM processing. The centerline holes, 2, 5, and 8 expanded the most, with the left and right aligned holes expanding less. The minimum material removed occurred at passage 3, with a mean removal of 0.0072 inches. The maximum material was removed at passage 8, with a mean removal of 0.034 inches. The maximum material removed was nearly five times

the minimum. Since the flow of the resin must have been primarily directed toward the center holes, it makes sense that these holes encountered the highest material removal rates.

Imaging was also conducted with the CMM to compare to the images recorded during the preliminary study. The CMM dimension measurements were compared only to the model data, because no dimensional data of the as-built model was successfully obtained with the CMM.

In an attempt to illustrate the material removal from the surface during AFM, an image overlay was produced (Figure 54).

Figure 54: The red area denotes parasitic powder particles and surface material that was removed from this particular passage during AFM processing.

The overlay illustrates to what extent AFM removed material from the surface. CMM images of the passages were also stitched together to form full composite images of the surfaces (Figure 55).

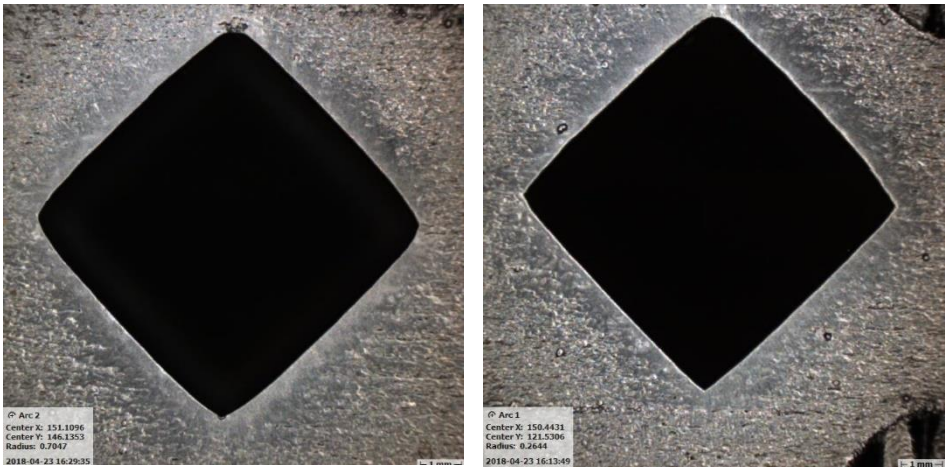

Figure 55: CMM image of passage 5 (Left) and CMM image of passage 8 (Right).

Rounding of the corners of these passages is clear in these images. Spill-out polishing of the edges of the interior passages can also be observed here.

Profilometry

The AFM processed double hexagon test coupon was sectioned with a metallography saw to perform profilometry on each of the nine passages. Profilometry was performed with a cut-off length of 2.5 mm where possible, but due to the restrictions of some of the passages, 0.8 mm was sometimes used. All four sides of the diamond shaped cavities were measured three times each to produce a total of twelve data points per passage. Again, upward and downward facing surfaces were compared to investigate how polishing handled the discrepancies in as-built roughness. Table IX depicts the mean roughness values for each processed passage, for both the upward and downward facing surfaces.

Table 9: Mean Roughness for Each Processed Passage

Passage	*Mean Upward Facing*	*Mean Downward Facing*
	µm Ra	*µm Ra*
1	0.278	1.673
2	0.370	1.217
3	0.167	2.117
4	0.362	1.410
5	0.375	0.692
6	0.297	1.298
7	0.293	1.875
8	0.730	4.332
9	0.510	1.217

From these data, it is immediately clear that AFM processing dramatically reduced the surface roughness of the as-built test coupon. On average, AFM reduced the surface finish from 14.07 μm to 1.07 μm. On the upward facing surfaces, all finishes were below 1 μm. There does indeed appear to be a discrepancy between upward and downward facing roughnesses even after polishing, albeit more slight than in the as-built conditition. There also exists more variability of the downward facing surfaces (Figure 56).

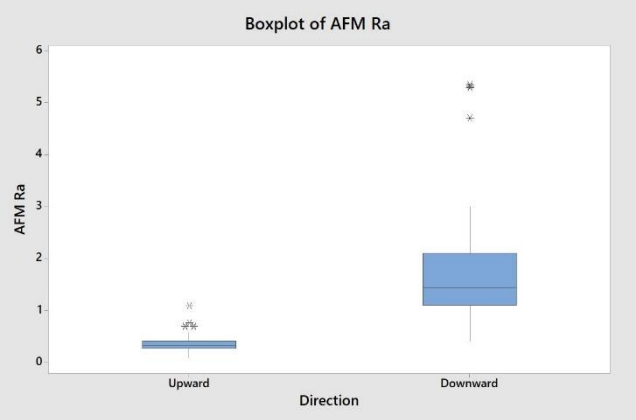

Figure 56: Boxplot of processed passages reveals a discrepancy in both the mean and deviation of the upward and downward facing surfaces.

Outliers are pressent for both the upward and downward facing profilometry measurements and these boxplots clearly indicate that the roughness experiences larger variation on the downward facing surfaces. To investigate the effect of specific passage type – and interaction with surface direction – a two way ANOVA statistical analysis was conducted (Table X).

Table 10: ANOVA Results for Direction and Passage

Source	DF	Adj SS	Adj MS	F-Value	P-Value
Direction	1	51.65	51.6537	237.34	0.000
Passage	8	31.96	3.9954	18.36	5e-16
Direction*Passage	8	22.27	2.7837	12.79	4e-12
Error	90	19.59	0.2176		
Total	107	125.47			

Although Direction and Passage both yield low p values, the interaction effect is indeed significant and thus the best way to explain the data as a whole. The signifcant interaction implies that a different level of polish was achieved depending on both the surface angle and passageway type, not one or the other. A potential correlation between the material removed, measured with CMM, and profilometry data was investigated. However, an R squared of 0.54 indicates that no such linear relationship exists. More material removal did not imply a lower surface roughness. In fact, the best fit line implies the opposite may be true; this is likely a coincidence as a result of the relatively high roughness and material removal at passage 8.

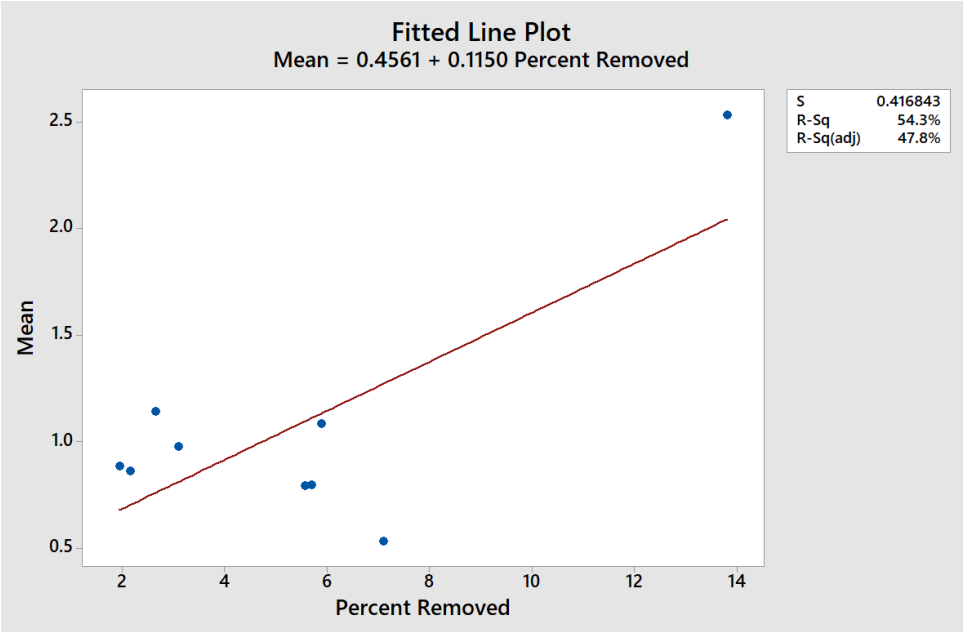

Figure 57: The line of best fit for surface roughness and material removal indicates, with R squared equal to 0.543, that there is no linear correlation between these two variables.

These results imply that, with the resin flow set-up for this test coupon, maximum polish was achieved. Because there exists no correlation between material removal and surface roughness, there is no evidence that further AFM cycles would have decreased the roughness further. Specifically targeting one chamber at a time, instead of polishing all nine at once, may have yielded a better polish. A further study

to investigate the effect of such a test set-up is recommended. Polishing all passageways at once produced data that highlights the geometric difficulties of the AFM process, including the changes in roughness, as well as rounding of angular features. Microscopy was conducted to examine how the geometry was modified as a result of polishing.

Some further profilometry was conducted on the passageways with internal cavities (Table XI). In general, these areas were difficult to measure with contact profilmoetry, so only a few data points were obtained. As expected, the surface roughness of the internal cavities was typically higher than the roughness in areas of smaller cross section. In addition, passages with expanding cross sections typically exhibited a higher roughness.

Table 11: Profilometry Measurements of Internal Features

Passage	*Mean Upward Facing µm Ra*	*Mean Downward Facing µm Ra*
1 (ends)	9.80	
2 (middle)	10.02	15.90
3 (cavity)	1.50	7.46
9 (ends)		0.50

The middle chamber of passage 2, for example, experienced hardly any improval in surface roughness after polishing. As expected, the expanding passages and internal chambers limited the beneficial effects of the AFM processing. A lower viscocity resin may be better able to reach thse geometrically offset regions.

Scanning Electron Microscopy

After AFM, scanning electron microscopy was conducted to investigate the effects of polishing on the geometry of the internal features. One of the primary reasons angular geometry was used in the design of the nine passageways was to investigate to what extent abrasive flow machining rounds corners. Figure 58 clearly depicts rounding at the corners of processed internal passages resulting from the abrasive flow.

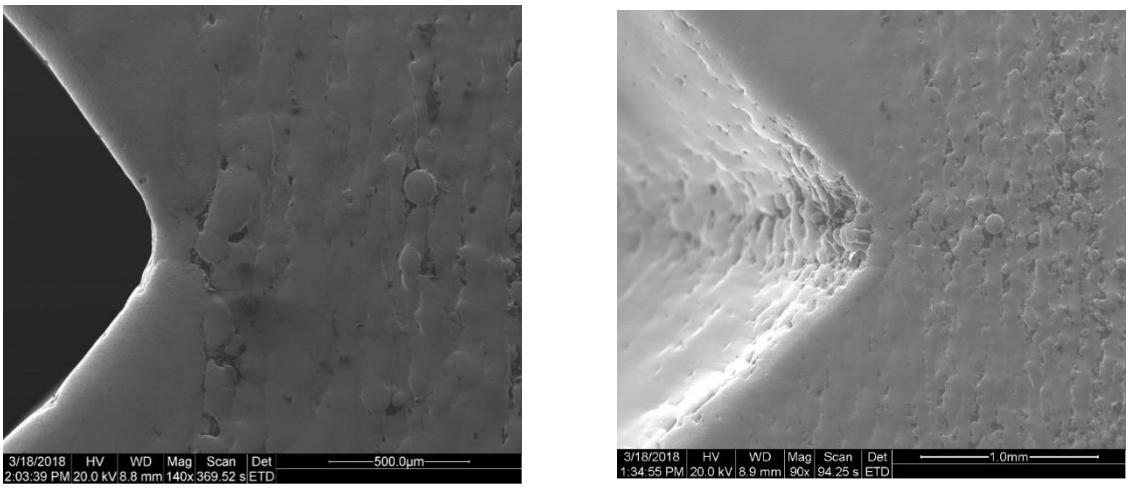

Figure 58: SEM images at 140x and 90x depict rounding at corners of internal features likely as a result of the abrasive resin flow pushed against the corner during processing.

It is not explicitly clear to what extent this rounding is a result of the AFM processing or if it existed – at least somewhat – before processing occurred. Although helpful, preliminary CMM and SEM do not present clear proof that the as-built components contained perfect 90 degree angles. Images of the as-built passages depict numerous instances of overhanging powder particles that make discerning the true surface of the component impossible. Nonetheless, it is reasonable to conclude that AFM contributed to this rounding effect or at least did not help the issue.

SEM of these surfaces corroborates the evidence put forth by the profilometry measurements (Figure 59, 60). The surface of the internal passages is certainly smooth, and free of any severe defects or lodged SiC particles.

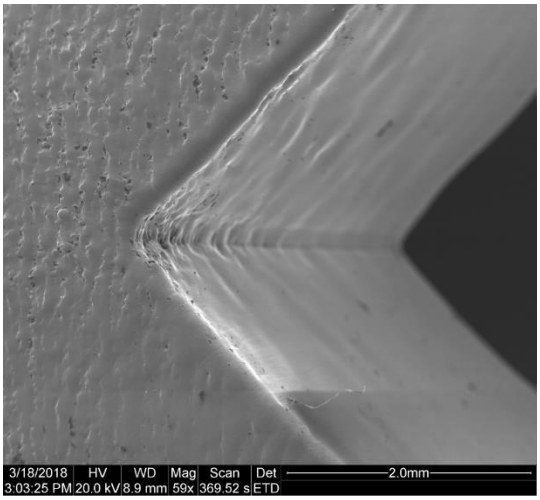

Figure 60: SEM Image 59x.

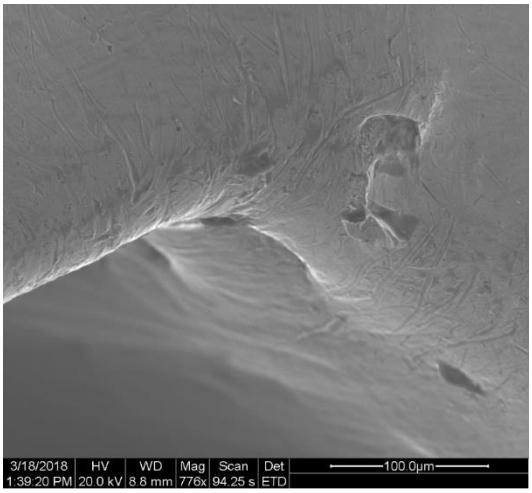

Figure 59: SEM Image 776x.

At the top corner of the passages, some overhanging powder particles remain, as indicated in Figure 59 (right). There is also a slight patterned texture to these corners, as shown in Figure 58. The cutting action of the SiC – the mechanism through which the component is polished – is visible in Figure 59.

4.2.2 Thin Disk Lattice Fill Test Coupon

The experimental design for the thin disk test coupon differs from that of the double hexagon test coupon because each sample was designed for different purposes. No profilometry or CMM was performed on the thin disk specimens. Rather, mass was recorded in the as-built condition and in the post-processed condition to investigate mass difference. In theory, abrasive flow polishing should remove parasitic powder particles and residual powder from the lattice, thereby decreasing mass. In addition, compression testing was performed on two un-processed samples and two AFM polished samples. Before compression testing, samples were waterjet cut as shown. The waterjetting was necessary to ensure the compression testing primarily tested the lattice, rather than the side walls of the cylinder. The goal of this particular experiment is to investigate to what extent AFM can remove residual and parasitic powder from the

lattice without compromising strength. A total of eight thin disk lattice coupons were printed for their respective purposes (Figure 61).

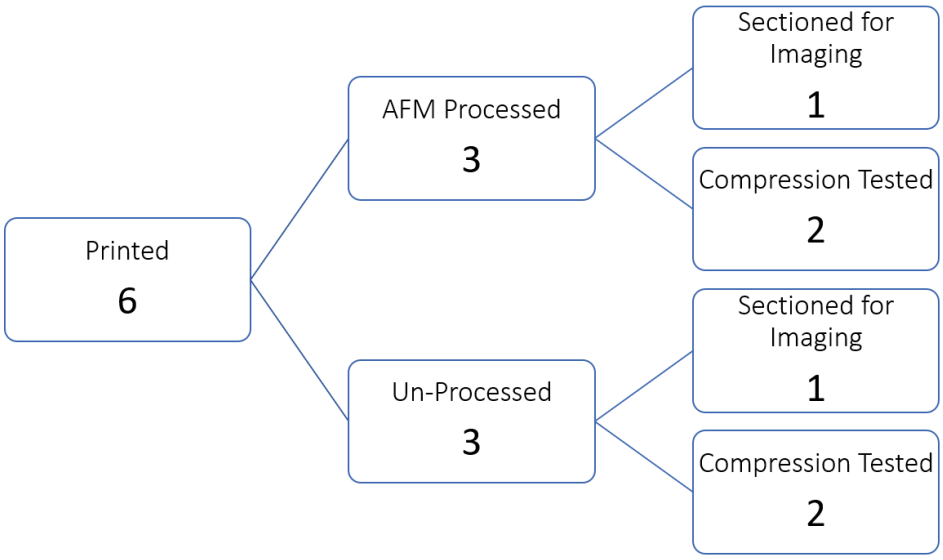

Figure 61: This experimental set-up was best as it allowed for the preservation of resources and variety of data gathering. Ideally, more samples would be compression tested for statistical reliability, but this would have been time and cost prohibitive.

Control Testing

SEM images of sectioned un-processed samples indicate why lattice processing would be valuable (Figure 62). Even more difficult to remove than excess powder, parasitic powder can sinter to the surface to the struts and prove especially problematic.

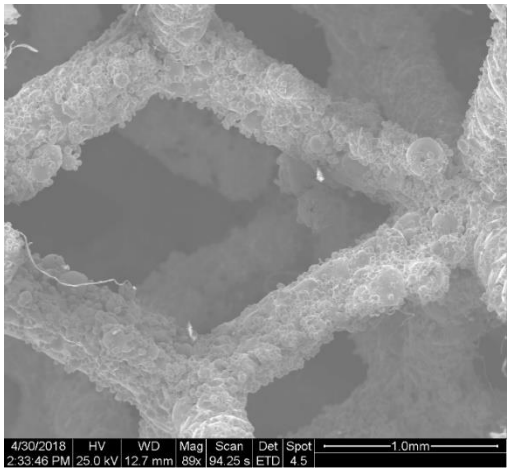

Figure 62: At 89x, parasitic particles are easily observed on lattice struts. These masses contribute mass without contributing any strength. In addition, excess powder can easily become trapped in the small spaces between struts.

To isolate the properties of the lattice from the relatively thick walls of the disk design, sectioning was required prior to compression testing. 0.5 inch by 0.5 inch cubes were cut from all four samples via water-jet equipped with garnet abrasive (Figure 63).

Figure 63: Plywood with a water-jet cut stencil to support the disk samples was used.

Figure 64: Shimadzu compression test was set-up as such for these tests.

Compression testing was performed with a Shimadzu mechanical compression test machine equipped with steel platens (Figure 64). The strain rate used for the tests was 1 mm/min. All tests were manually stopped once the lattice was sufficiently crushed and stress began to rise rapidly, indicating the sample began to perform as solid material. Load-displacement curves are presented in Figure 65 for all three control test specimens. An extra control test specimen was obtained from another study.

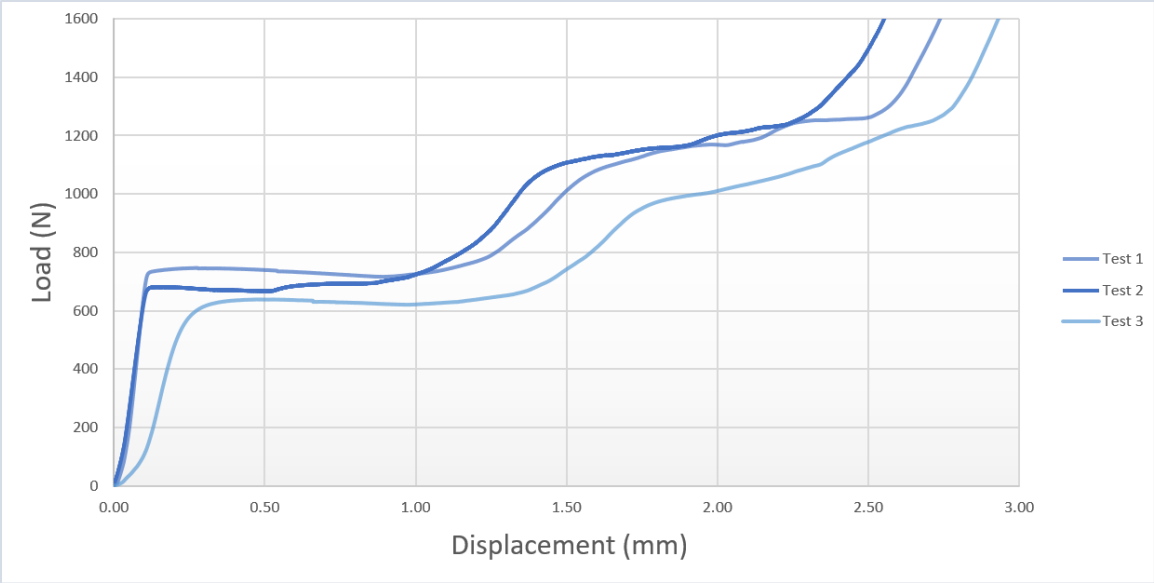

Figure 65: All three tests presented similar responses. Yield occurs within the 600 N to 800 N range, at which point a long period of strain is encountered before a second peak.

The above curves can be divided into three regions from low to high displacements: elastic, primary displacement, and secondary displacement. In the initial area of the curve, only elastic deformation occurs. After the yield point, the lattice begins to plastically deform during the primary displacement region. The plastic deformation mechanism for these lattices is likely bending, not buckling, because these plots indicate a progressive failure and not sudden and catastrophic failure. After 1 to 1.5 mm of displacement, the stress again rises to a secondary peak where secondary displacement begins. At this point, a new area of lattice begins to bend until it is totally compressed. After the lattice has failed completely, stress rises rapidly as the sample begins to perform as a block of solid material: the densification region. The tests were stopped once densification was reached.

Relevant mechanical properties were derived from these compression tests (Table XIII).

Table 12: Mechanical Properties of Control Thin Disk Specimens

	Elastic Modulus (MPa)	Yield Strength (MPa)	Load at Yield (N)	Strain at Yield (mm)
Test 1	405.94	4.88	740.06	0.488
Test 2	351.97	4.41	669.58	0.418
Test 3	194.27	4.10	622.92	0.906
Average	**317.39**	**4.46**	**677.52**	**0.604**

Considerable variability exists for both elastic modulus and strain at yield for the three test specimens but yield strength and maximum load are both fairly consistent. Fully crushed control test specimen is indicated in Figure 66. After compression testing, one of the test specimens was investigated with the SEM to confirm lattice strut bending as the failure mechanism (Figure 67).

Figure 66: Control test specimen 2 was fully crushed during compression testing.

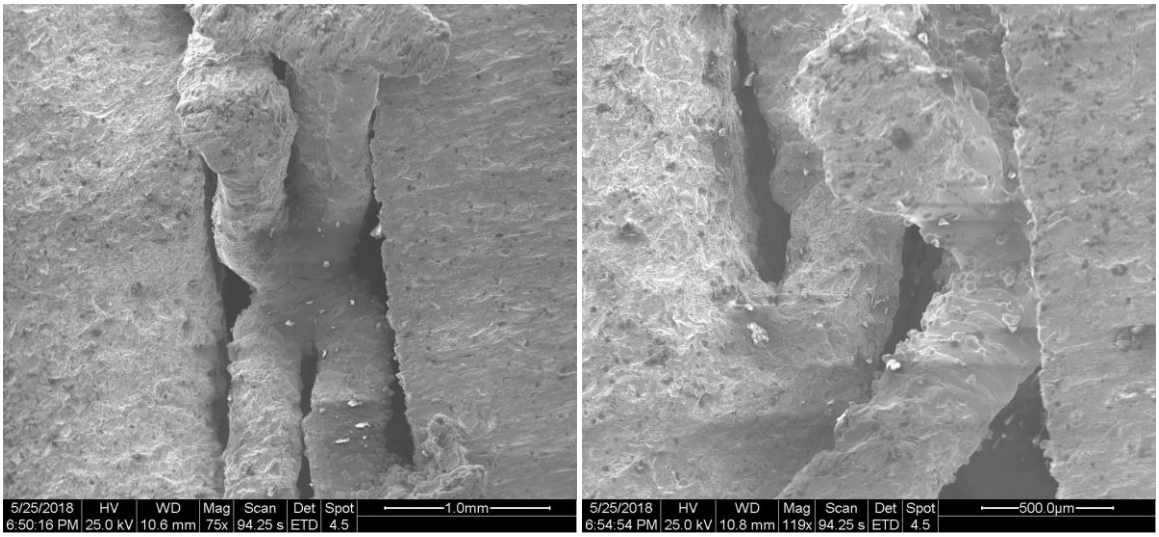

Figure 67: SEM of compression tested sample indicate strut morphology typical of a bending failure, rather than a buckling failure.

AFM Processed Sample Testing

Three of these samples were processed with AFM to measure mass difference, compressive mechanical properties, and surface quality. Mass measurements were used to indicate the parasitic particle mass removed from the lattice struts. Compression testing of polished samples was conducted to conclude if polishing affected the strength of the lattice. Microscopy of the polished samples was compared to that of the unpolished samples to investigate the difference in surface quality. All three components were processed with the same parameters and for the same duration. *Extrude Hone* reported issues with completely removing the media from the lattice after processing, however. Their typical method of

solvent and compressed air blasting was unsuccessful. So mass measurements of the AFM processed samples actually indicated an increase in mass after processing (Table XIII).

Table 13: Mass of Abrasive Flow Machined Thin Disk Samples

Sample	Mass Before	Mass After
1	17.0661 g	17.9027 g
2	17.0438 g	17.8153 g
3	17.0726 g	17.6109 g
AVG	**17.0608 g**	**17.7763 g**

On average, the mass increased by 0.715 grams after polishing due lattice entrapment of the media. If AFM were to be used for the polishing of lattice components, the removal of the trapped media is a problem that must be solved. Two un-sectioned samples and one sectioned sample were soaked in acetone for several hours in an attempt to dissolve and remove the media. After this process, the two un-sectioned samples were weighed once again (Table XIV).

Table 14: Media Removal with Acetone Soak

Sample	Mass Before Soak	Mass After Soak	Mass Removed
2	17.8153 g	17.4748 g	0.3405 g
3	17.6109 g	17.3141 g	0.2968 g

Moderate success was encountered with the acetone soak strategy. 0.3405 grams and 0.2968 grams were removed from samples 2 and 3, respectively. Although this represents a good start, the samples are still heavier than before processing; media remains inside. Acetone soak of the sectioned sample seems to have been much more effective, due to easier access to the interior lattice. SEM imaging was conducted on the sectioned polished sample to investigate the surface characteristics. Additionally, the acetone-soaked section was compared to the un-soaked specimen (Figure 68).

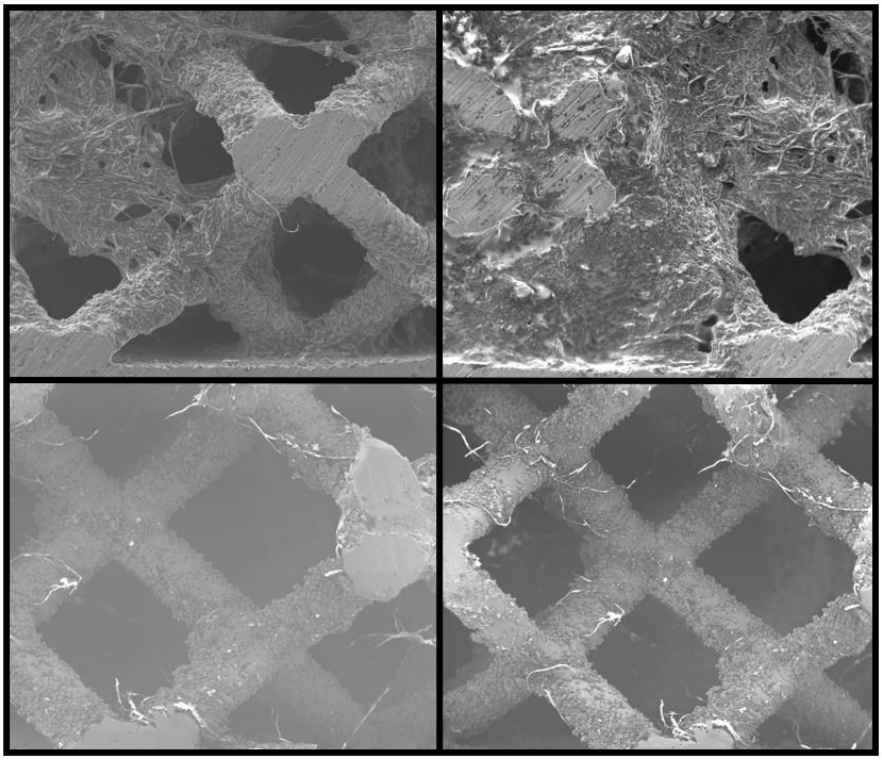

Figure 68: The top images are unsoaked lattice and the bottom images are soaked lattice. All images at 55 to 60 x magnification.

It is immediately clear from these SEM images that the unsoaked sample is contaminated with media and unusable as-is. The soaked sample appears much better, with little to none media observable within the lattice. In both samples, however, non-metallic stringy material can be observed clinging to the part surface. It is not apparent exactly what the source of this debris is, but this material is likely polluted material from the media. This may be eliminated if freshly made media is used in the *Extrude Hone* machine, rather than recycled media. These strings may also be remnants of the rubber media, partially degraded from the acetone soak.

SEM was also conducted to evaluate the surface finish the polished lattice. From Figure 67, the polishing effects are far less noticeable on these samples than observed in the double hexagon test coupon test. *Extrude Hone* reported that the lattice design significantly restricts the type of resin and abrasive particle size that can be used. As a result, polishing is much less effective. At higher magnifications, polished areas can be observed (Figure 69).

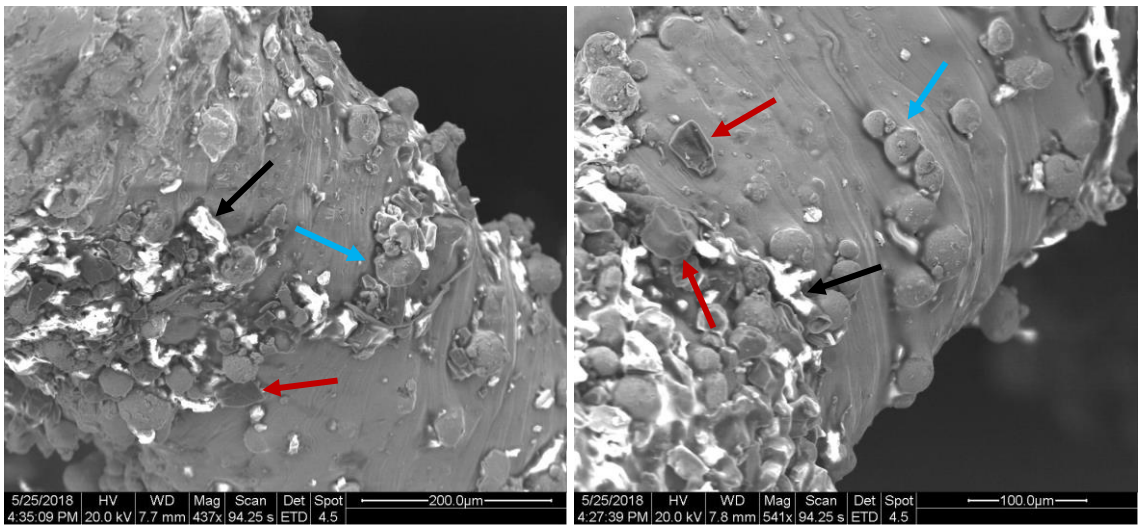

Figure 69: The lattice strut surfaces depict inconsistent polishing as well as adhered media and abrasive particles.

In the above image, adhered media (which appears white here, due to charging from the microscope electron beam), SiC abrasive particles, and parasitic powder particles can be observed. Media, abrasive particles, and powder are denoted by black, red, and blue arrows respectively. Compared to Figure 62, much of the parasitic powder particles have been removed. However, the polishing is incomplete. The complex geometry of the lattice also means that polishing cannot occur consistently across all surfaces. The surface has been improved somewhat, but new pollutive material, including media and abrasive particles, has been introduced in exchange.

The two un-sectioned AFM processed lattice coupons were prepared for compression testing. Just like the unpolished samples, these specimens were waterjet cut into 0.5 inch by 0.5 inch cubes for compression testing. Unfortunately, one of these samples was lost in the waterjet tank due to inaccuracies from a worn nozzle. Subsequent testing was again performed with the Shimadzu device, with a strain rate of 1

mm/minute. The tested AFM processed sample was overlaid upon the original control compression testing data (Figure 70).

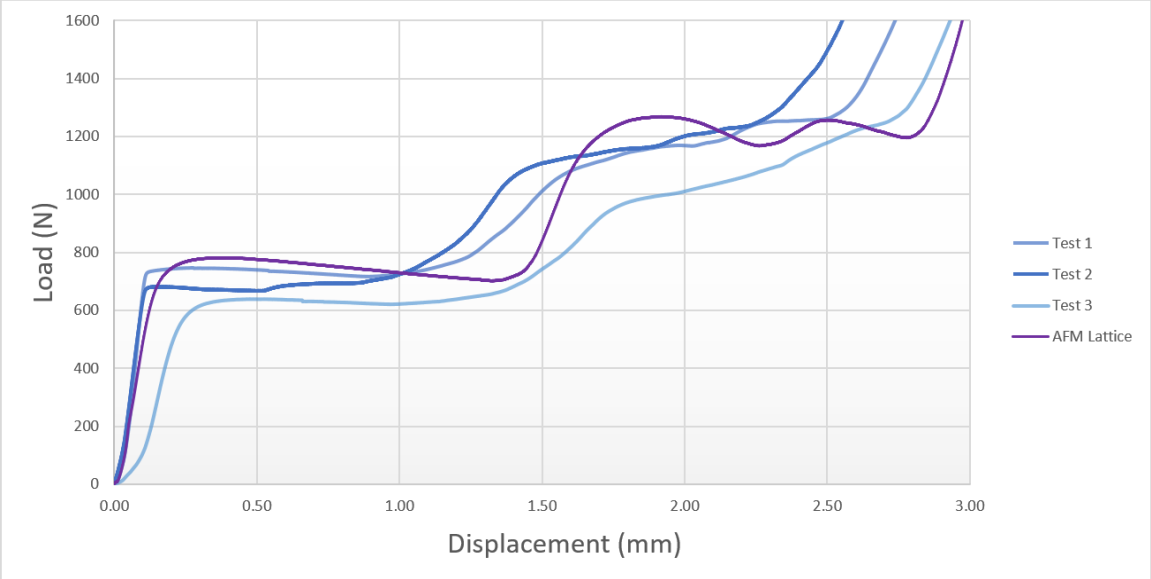

Figure 70: Compression testing of control samples with AFM processed sample does not indicate any dramatic differences.

Compared to the control samples, the AFM processed sample slightly better yield strength (Table XV). However, it is not clear if this difference is due to variability, AFM processing, or other factors.

Table 15: Compression Testing of AFM Lattice Compared to Control

	Elastic Modulus (MPa)	Yield Strength (MPa)	Load at Yield (N)	Strain at Yield (mm)
Test 1	405.94	4.88	740.06	0.488
Test 2	351.97	4.41	669.58	0.418
Test 3	194.27	4.10	622.92	0.906
Average	**317.39**	**4.46**	**677.52**	**0.604**
AFM	**271.14**	**5.19**	**780.94**	**0.372**

The slight difference between the AFM lattice and the control lattices may be a result of varying build quality – these samples were not all built on one build plate at once. The sample size is too small to conduct a statistical analysis so conclusions on mechanical properties are difficult to draw. However, the evidence does seem to imply that AFM, at the very least, does not significantly decrease the compressive

strength of the lattice. Likely, this should not be a significant concern for AFM lattice processing – the major concerns are achieving complete polishing of the lattice and removing all media and debris.

4.3 Ultrasonic Shot Peening Results

Ultrasonic shot peening was conducted at *Empowering Technologies* in Birmingham, Alabama. Two double hexagon test coupons were treated, each with the same processing parameters except the type of media (Table XV).

Table 16: USP Treatment Processing Parameters

	Specimen 1	**Specimen 2**
Media Diameter	1.8 – 2.0 mm	2.0 mm
Media Material	Ceramic	100C6 Steel
Quantity	7.5 g	10.1 g
Amplitude	70 μm	70 μm
Treatment Time	90 seconds	90 seconds

Specimen 1 was peened with ceramic media and Specimen 2 was peened with steel media; the diameter of both media types was 2.0 mm. Unlike AFM, all surfaces of the part were treated, including the interior passages. Complete processing of the internal surfaces would be impossible as a result of the loss of kinetic energy of the media. Dimensional changes are less of a concern for USP because the process does not remove material; it only compresses the material at the surface. The ability of the process to improve the roughness of surfaces with support structure stubs is also of interest. The support structure was

removed from the downfacing surfaces of the hexagon with hammer, chisel, and pliers, leaving behind an undesirable surface that requires processing (Figure 70).

Figure 71: Removal of the support structure from the base of the hexagon leaves behind a surface too tough for any profilometry measurements.

Besides profilometry, metallography was also performed on samples obtained close to the peened surface. Due to the high energy input of the peening media, it is possible that that surface may have encountered severe plastic deformation (SPD) and even recrystallization. In addition, hardness data of material in the untreated state was compared to hardness data of the peened samples.

The peening of these samples required development of two unique enclosures, one for the peening of surface 8A and 8B and another for the peening of the edges. The edges were treated first for 90 seconds each and rotated clockwise until all surfaces were peened. Then, the sample was removed from the edge fixture and placed into the face fixture and peened for 90 seconds on each face (Figure 71).

Figure 72: Enclosures were developed by Empowering Technologies for the peening of these specimens.

The customized enclosures are a significant driver for the cost of USP, and custom enclosures are required for most parts. Empowering Technologies processed these specimens as described with the following set-up (Figure 72).

Figure 73: USP treatment set-up at Empowering Technologies with A: StressVoyager Central Unit, B: Ultrasonic Generator, and C: Enclosure Base.

After USP treatment, the surface finish appears much better than in the as-built condition (Figure 73).

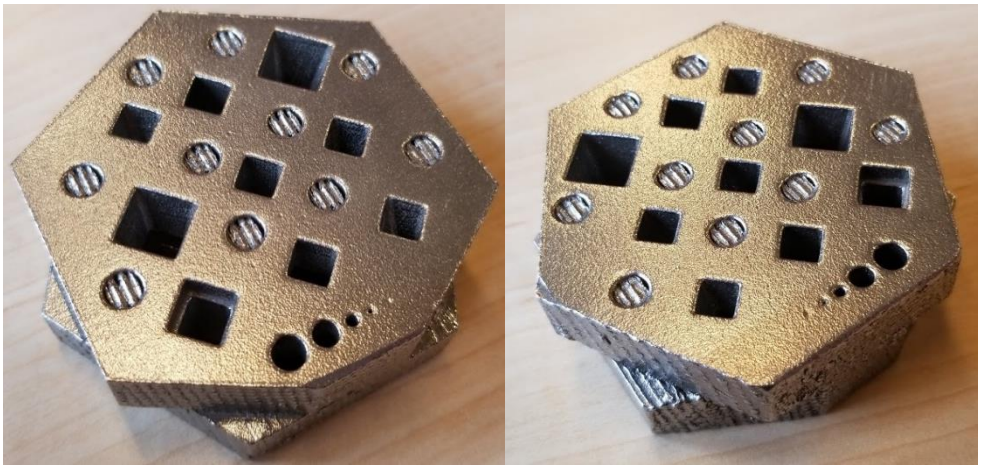

Figure 74: The USP treated samples (Left: Specimen 1, Right: Specimen 2), from appearance, indicate a much better surface finish than in the as-built condition.

Visually, a few observations can be made. Slight burring can be noted around the edges of the part and passages. The treatment did indeed dramatically improve the surface of the supported downfacing surfaces; evidence of support structure stubs remains after processing. Further examination with profilometry is required to verify these observations.

Profilometry

Just as in Section 4.1.1, profilometry was performed on each of the external surfaces of the double hexagon coupon for both samples 1 and 2. Average Ra and Rz values for each surface, excluding the supported surfaces, are reported for sample 1 in Table XVI and sample 2 in Table XVII.

Table 17: Profilometry Results for USP Specimen I

	1A	1B	2A	2B	5	6A	6B	8A	8B	$\bar{x}$
Ra (µm)	2.31	2.07	2.34	2.34	1.90	2.47	2.42	1.96	2.20	2.22
Rz (µm)	10.38	10.58	12.89	13.87	8.13	9.01	12.93	10.06	11.55	10.98

Table 18: Profilometry Results for USP Specimen II

	1A	1B	2A	2B	5	6A	6B	8A	8B	$\bar{x}$
Ra (µm)	2.00	1.81	1.84	2.51	2.36	1.71	2.19	2.13	1.94	2.06
Rz (µm)	9.15	10.42	9.17	12.09	11.38	8.90	11.19	10.45	9.39	10.34

Immediately, it is clear that USP treatment significantly improved the surface finish of both specimens. Mean surface roughness for specimen 1 is 2.22 Ra and 2.06 Ra for specimen 2. Compared to the 13.47 Ra average roughness of the as-built specimen, USP treatment dramatically improved the surface roughness. Statistical analysis into the effect of media type and surface type was conducted to investigate the significance of these data. Simply evaluating the significance of the difference in roughness between the

two samples is inadequate, so a more complex statistical model must be constructed. A two-way ANOVA, with Specimen (2 levels) and Surface (9 levels), produced interesting results (Table XVIII).

Table 19: Two-Way ANOVA for USP Roughness

Source	*DF*	*Adj SS*	*Adj MS*	*F-Value*	*P-Value*
Specimen	1	0.3750	0.37500	5.40	0.026
Surface	8	1.0099	0.12624	1.82	0.106
Specimen*Surface	8	1.6858	0.21072	3.03	0.010
Error	36	2.5003	0.06945		
Total	53	5.5709			

The ANOVA results indicate that the Specimen and Surface interaction effect was significant with a p-value of 0.010. Thus, from the model it can be concluded that there is no evidence that a significant difference in surface finish exists only because of the media material (ceramic or steel). However, significant differences exist when specimen and surface type are combined as an interaction term. This result implies that ceramic and steel media have varying effectiveness on different surface types. It is unclear if this result is truly indicative of the USP process, or more a product of variability introduced from the printing process. Due to time and resource constraints, profilometry was not conducted on every test coupon – the preliminary experiment results are shared as comparisons for the subsequent experiments. Thus, there is no rational, practical explanation of the significance of this interaction effect. The most valuable piece of information from the result of this ANOVA is that there is no statistically significant evidence that 2.0 mm ceramic media affects the surface roughness of this part any more than the 2.0 mm steel media does.

Another key investigation of this USP experiment is to evaluate the ability of the process to improve the finish of supported surfaces. The stubs left behind from support structure removal produce a macro-roughness that requires finishing. This surface is so rough that profilometry measurements are impossible, but after USP, these downward facing supported surfaces were reliably measured (Table XIX).

Table 20: Surface Roughness Measurements for Supported Surfaces

	3A	3B	7A	7B
Ra (µm)	7.52	6.70	5.91	5.47
Rz (µm)	41.26	33.25	11.55	29.00

The roughness on these surfaces is certainly much higher than the roughness on the non-supported surfaces, but even this represents an achievement of the technology. This surface finish is likely still unacceptable for many engineering applications, however. Nevertheless, the difference between the as-built (after support structure removal) surface and the USP processed surface is plain to see (Figure 74).

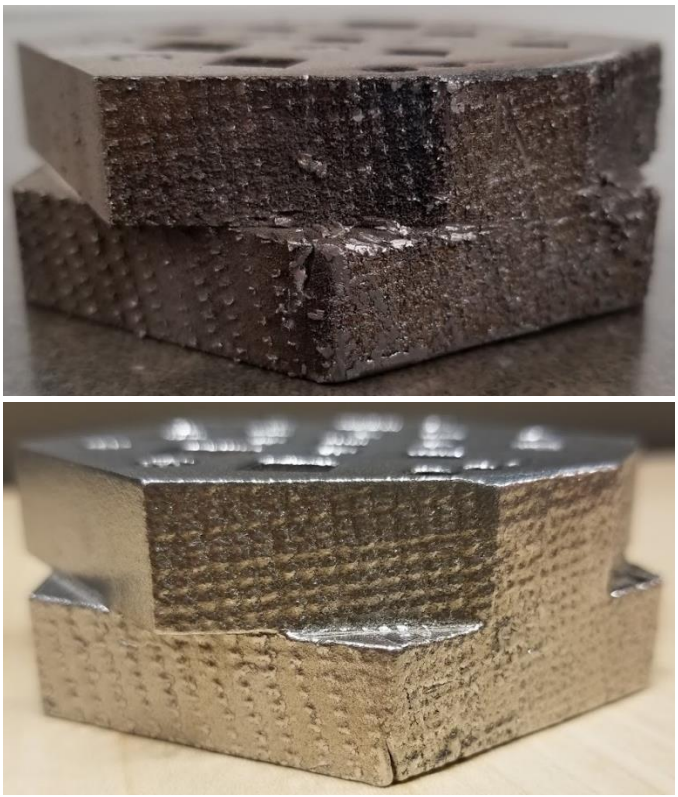

Figure 75: (TOP) As-built Specimen 2 after support structure removal via hammer, chisel, and pliers. (BOTTOM) USP treated specimen 2 reveals an albeit rough, but much improved surface.

The forming of a rounded crease at the sharp corners can be observed on the USP processed specimen in the figure above. From one perspective, this represents dimensional instsability. But from a mechanical design perspective, this slight rounding reduces the stress concentration factor of that sharp corner.

Only partial peening was possible for the interior surfaces, but profilometry was nonetheless conducted on all nine internal passages to investigate its effectiveness. Specimen 2 was sectioned, just as the AFM double hexagon test coupon, to perform these measurements. Due to geometric constraints and issues from this build, passage three was not measured successfully. Again, a deviation between mean roughness of upper and lower surfaces is observable (Table XX).

Table 21: USP Specimen 2 Internal Profilometry

Passage	*Mean Upward Facing* *µm Ra*	*Mean Downward Facing* *µm Ra*	*Average* *µm Ra*
1	3.80	8.33	6.065
2	3.37	13.28	8.325
3	***	***	***
4	2.65	6.19	4.420
5	4.63	13.51	9.070
6	5.37	7.86	6.615
7	4.36	8.76	6.560
8	5.41	13.88	9.645
9	2.17	4.82	3.495

The discrepancy between upward and downward facing surfaces proves a fairly stubborn difference to eliminate with USP processing. However, the roughness for both upward and downward facing surfaces depicts a significant reduction, even with only partial peening. Passages 4 and 9 depict the lowest average, upward, and downward roughnesses. For some passages, such as 5 and 2, there are large discrepancies between the upward and downward surfaces. For others, like 6 and 7, the roughnesses are similar for upward and downward facing surfaces. Thus, two-way ANOVA was performed to investigate the effects of passage type, surface direction, and the interaction effect (Table XXI).

Table 22: ANOVA Results for USP Interior Profilometry

Source	*DF*	*Adj SS*	*Adj MS*	*F-Value*	*P-Value*
Passage	7	196.77	28.110	26.44	1.36e-11
Direction	1	377.89	377.890	355.49	0.00000
Passage*Direction	7	94.13	13.447	12.65	1.18e-7
Error	32	34.02	1.063		
Total	47	702.80			

ANOVA results indicate that the interaction effect of Passage and Direction is statistically significant. So, there is no individual relationship for passage or direction; the combination of these two factors determines how well the surface will be peened. This matches well with earlier analysis above – some passages show large differences between upward and downward facing surfaces whereas others are quite close in value. Looking at the geometries of both cases provides the practical explanation for this phenomenon (Figure 75).

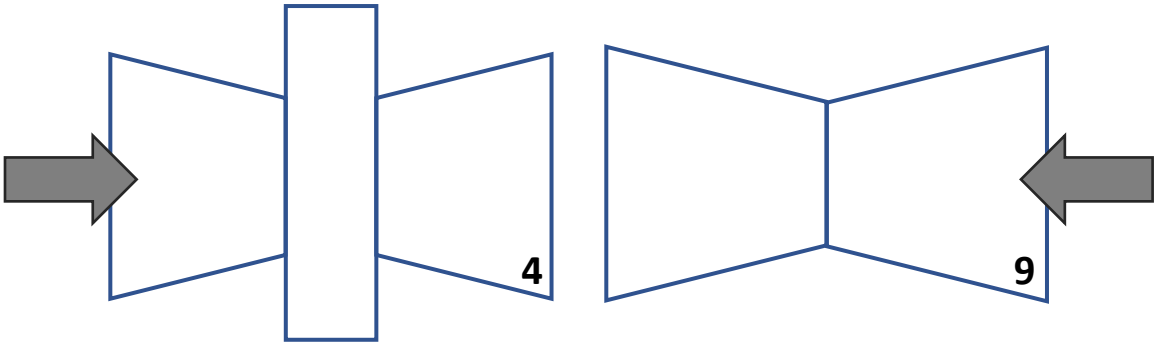

Figure 76: Passages 4 and 9 are both funnel-shaped designs which can effectively channel and amplify media movement during the peening process. Peening direction is indicated by the arrows here.

USP was highly effective for passages 4 and 9 because of their geometries. The converging geometry design funnels media through the passageway, achieving high contact area percentage throughout the

entire process. The geometry of passages 6 and 7 also reveals why the disparity between upward and downward facing surfaces was so minimal compared to the other passages (Figure 76).

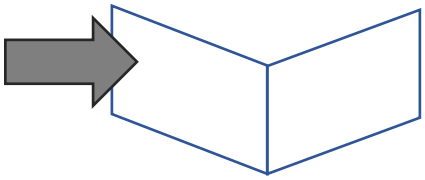

Figure 77: The bent angle design of passages 6 and 7 means more media will impact the downfacing surface than the upfacing surface, yielding a final finish that is similar for both surface types.

The angled geometry here actually preferentially orients the downward facing surface for the peening operation. The upward facing surfaces had a much lower roughness in the as-built condition, before USP processing. As a result, the final surface finish for these surfaces are fairly similar. Lastly, the geometry of passages 5 and 8 reveal why peening was so unsuccessful for both upward and downward facing surfaces (Figure 77).

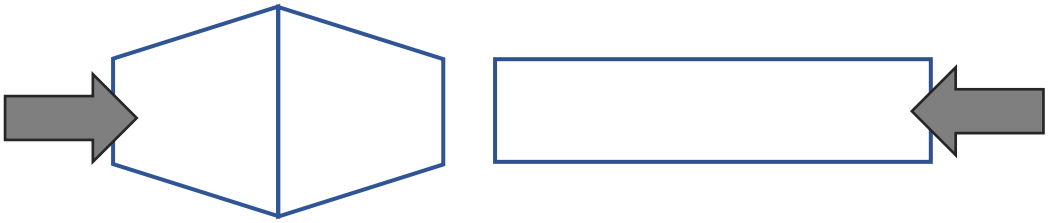

Figure 78: Passage 8 has an expanding shape which is not conducive to effective peening. Passage 5 has a straight-through geometry which prevents contact of most peening media.

Both passages 5 and 8 experiences little reduction in surface roughness from the USP operation. The geometry of these passages virtually eliminates all contact from the media. In passage 8, the expanding geometry means media will lose most of its kinetic energy before impacting the expanded middle section. In both passages, media is more likely to simply pass through, hardly contacting the walls of the passage. Thus, the effectiveness of USP for internal features is exceptionally dependent on the geometry. Unlike AFM, more complex passages do not necessarily inhibit USP effectiveness. Complex, preferentially oriented passages can certainly be effectively processed with USP but straight through passageways present a challenge.

Hardness Testing

A hardening effect is expected from the mechanical energy input to the sample surfaces during peening. Rockwell B hardness measurements with 1 kg load were conducted on a variety of as-built samples for comparison against the peened samples. 12 measurements yielded a mean hardness of 105.67 HRB with a standard deviation of 2.661. After peening, specimens 1 and 2 were hardness tested with identical parameters for 10 repetitions. Surfaces 8A and 8B were tested 5 times each in a variety of locations. Specimen 1 (ceramic media) yielded 109.00 HRB with a standard deviation of 3.060. Specimen 2 (steel media) yielded a higher hardness of 112.74 HRB with a narrower standard deviation of 2.162. ANOVA was conducted to determine the statistical significance of these differences (Table XXII).

Table 23: ANOVA Results for As-Built, Specimen 1, Specimen 2 Hardness Measurements

Source	DF	Adj SS	Adj MS	F-Value	P-Value
Factor	2	273.0	136.499	19.37	4.55e-6
Error	29	204.4	7.047		
Total	31	477.4			

With a low p-value of 4.55e-6, it is reasonable to conclude that the hardnesses of the as-built sample, specimen 1, and specimen 2 are indeed different. The Fisher LSD method was then used to determine which of the differences are significantly different (Table XXIII)

Table 24: Fisher LSD for Hardness with 95% Confidence

Factor	N	Mean	Grouping		
Specimen 2	10	112.740	A		
Specimen 1	10	109.000		B	
As-Built	12	105.667			C

The results of the Fisher pairwise comparison analysis indicate that all differences are statistically significant with 95% confidence. So, the hardness of specimen 1 differs statistically significantly from

specimen 2; both specimen 1 and 2 are statistically different from the as-built sample. Thus, the peening with steel media produced a higher hardness than the peening with ceramic media. This fact combined with the result that no surface roughness difference exists between same-sized ceramic and steel media implies that steel media is likely best when surface hardness and surface roughness are important considerations.

Computational Measuring Machine

Diagonal measurements of all nine passages of USP processed specimen 1 was conducted just as in section 4.2.1 for the AFM processed double hexagon component. Ultrasonic shot peening slightly burred or rounded the edges of these passages, so careful measurements were required to accurately measure these diagonals. Boxplots for the deviation from the model measurements were again produced (Figure 78).

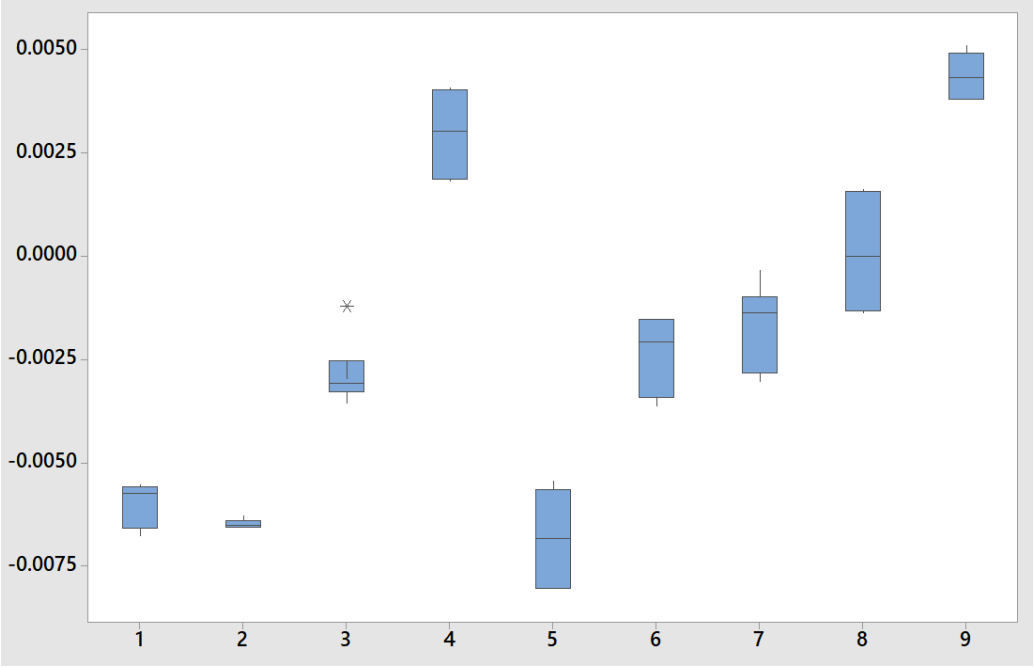

Figure 79: Boxplots of dimensional measurements after USP indicate a fairly wide dispersion of data that does not suggest material was actually removed after processing. The y axis corresponds to inches removed and the x axis corresponds to the passage number.

The boxplot data does not reveal universally that the processing enlarged the passages after processing. On average in fact, diagonal measurements of the USP processed component are 0.0021 inches smaller than the model measurements. Because ultrasonic shot peening does not directly remove material and instead compresses the surface, it makes sense that the passages are not dramatically enlarged after processing. In the as-built condition, partially sintered and unmelted powder adheres to the surface making it unclear precisely where the part surface is located, as discussed in the Preliminary Results. During peening, the media strikes this surface and compresses or removes the adhered particles. Thus, the USP processed dimensions are much closer to the actual CAD model than the dimensions of the as-built condition.

Nonetheless, statistically significant variation exists between the deviation of each processed passage. It is not precisely clear if this variation is a product of the peening, the CMM image recognition software, or SLM manufacturing variability. ANOVA results confirm that these discrepancies are statistically significant (Table XXIV).

Table 25: ANOVA Results for USP Passages

Source	DF	Adj SS	Adj MS	F-Value	P-Value
Factor	8	0.000780	0.000097	105.20	0.00000
Error	45	0.000042	0.000001		
Total	53	0.000821			

The p value is nearly zero, so there indeed exists a significant variability in the dimensional stability of passage to passage. Certain geometries, as described in the profilometry section, are more receptive to media impact which decreases surface roughness and may indeed also affect the dimensional stability of these passages. Thus, just as for AFM, a regression model was developed to investigate any correlation between dimensional measurements and surface roughness (Figure 79).

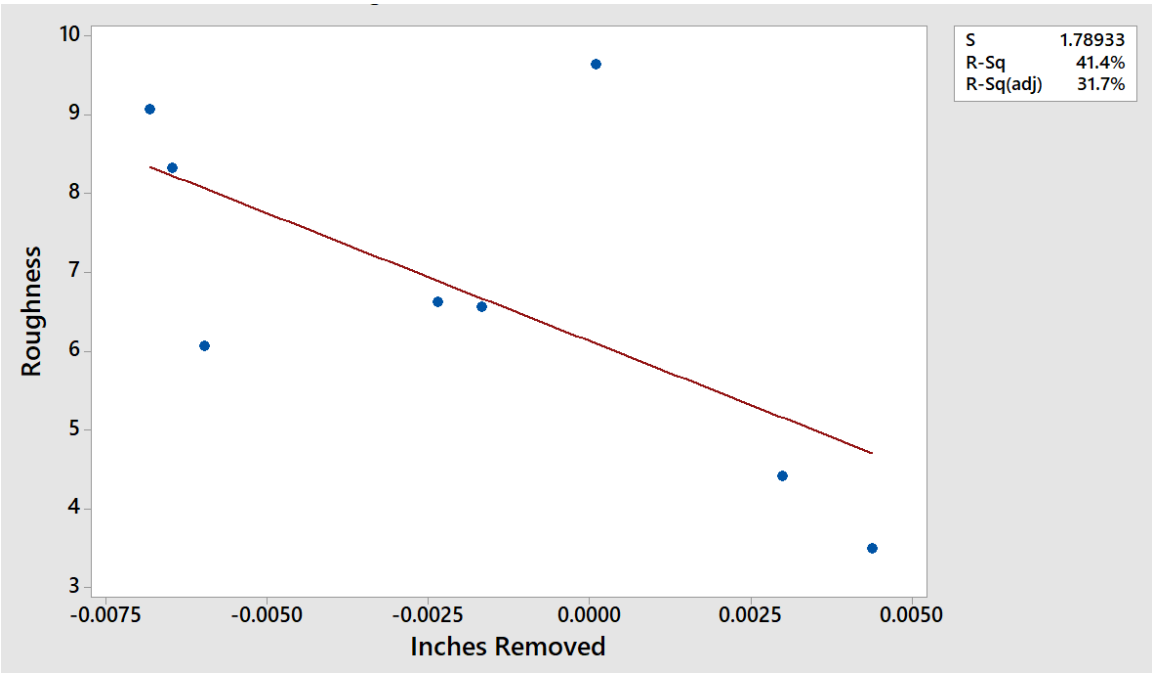

Figure 80: Linear regression model depicts a potential correlation with a relatively low R squared value of 0.414.

The model suggests that a lower roughness is only achieved by further compressing surface and increasing the distance of the passageway diagonal. However, the R squared value is only 0.414, so it remains unclear if these variables remain correlated. Practically, this correlation does have a reasonable explanation. The geometry of the passages either allow peening or prevent it. If the media can indeed contact the surface, the surface roughness will reduce as the surface compresses.

Imaging

Scanning electron microscopy was conducted on both USP specimen 1 and 2 to examine the surface and morphology changes associated with the peening process. Specimen 1 was left un-sectioned. Images of the surface morphology of surface 8A were produced (Figure 80).

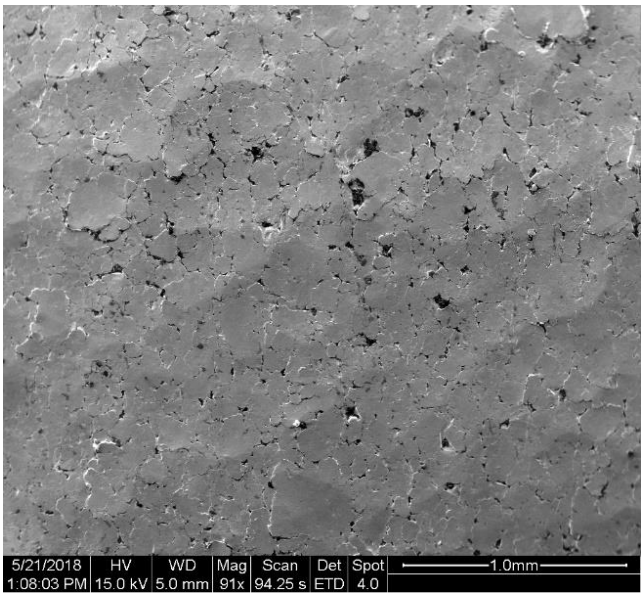

Figure 81: Dimples and cracks mark the peened surface at 91x magnification.

Figure 80 provides insight into the mechanism of USP processing. Every time a media particle strikes the surface of the component, a dimple is left behind. With enough peening, enough dimples will form to sufficiently decrease the surface roughness of the component. However, the morphology of these dimples represents the surface finish limit of USP. Ultrasonic shot peening, even with enough time, will likely never produce a mirror-like finish because of these overlapping dimples. Cracks and voids can also be observed in Figure 80. These are a product of the high kinetic energy input from the media during the process. Seemingly, these features may not be cracks at all. Rather, gaps between crushed parasitic powder or partially melted powder appear as cracks but in fact are likely not so. The geometry of the peened internal passages was also investigated with SEM (Figure 81).

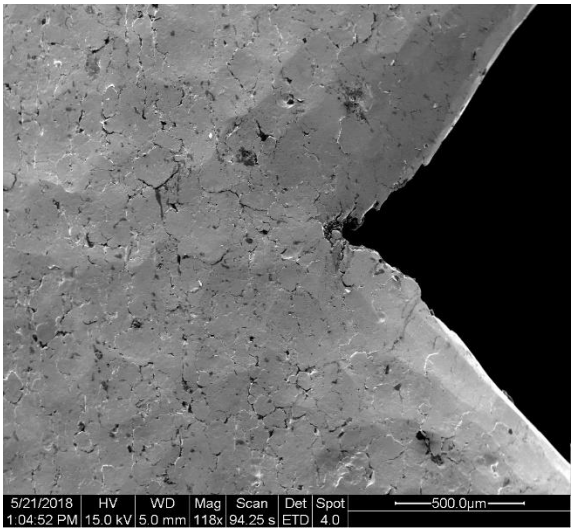

Figure 82: Corner of USP processed passage indicates potential preferential attack of this region.

Angular features such as corners may be vulnerable to USP media during processing, the above image implies. The corner here is not particularly rounded; however, it does appear deepened by the USP processing. It is likely that media striking of the seam expanded the geometry into a valley-like shape. This effect is certainly a consideration for USP processing. Special attention to these types of features is required for industrial adoption of USP.

After USP specimen 2 was sectioned for profilometry, a small section was used for metallography. The sample was mounted in Bakelite, grinded and polished to a 0.5 µm finish, then electro-etched with oxalic acid, just as other metallography samples were processed. The goal of metallography was to investigate the surface effects from the peening process. Specifically, it is known that USP significantly increased the hardness of both specimens. SEM images were obtained to explore precisely how USP hardened the surface of the as-built sample. Grain deformation can be observed on the as-peened surface (Figure 82).

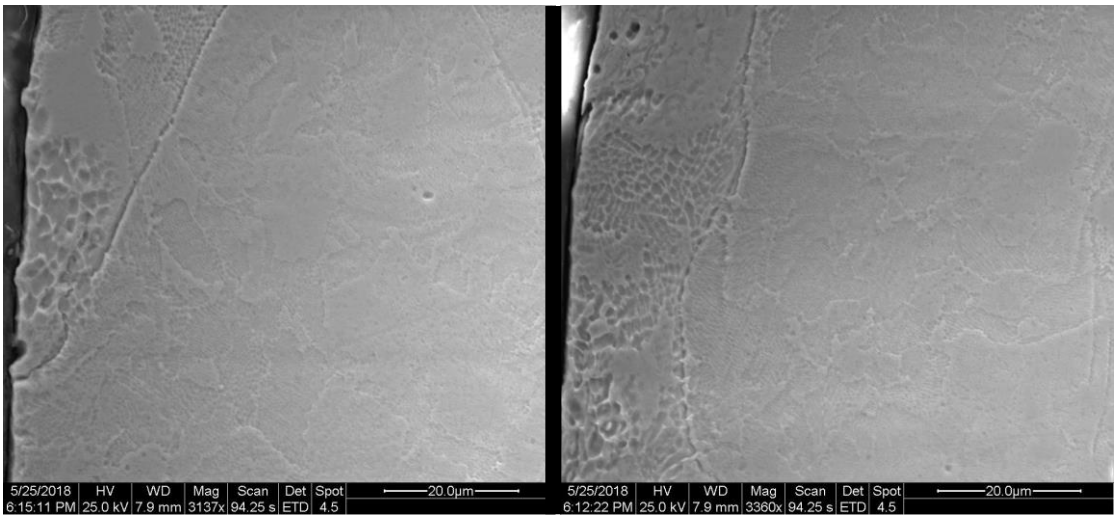

Figure 83: No signs of SPD induced nanocrystalline grains are present, but USP deformed the microstructure on the surface.

From SEM imaging, it does not seem that USP severely plastically deformed the surface. SPD can yield ultrafine nanocrystalline grains, but no such phenomenon is observed here. USP did deform the microstructure on the surface of the component, but actually enlarged the grains. Recrystallization most likely did not occur. Another advantage of USP is its ability collapse any near-surface pores (Figure 83).

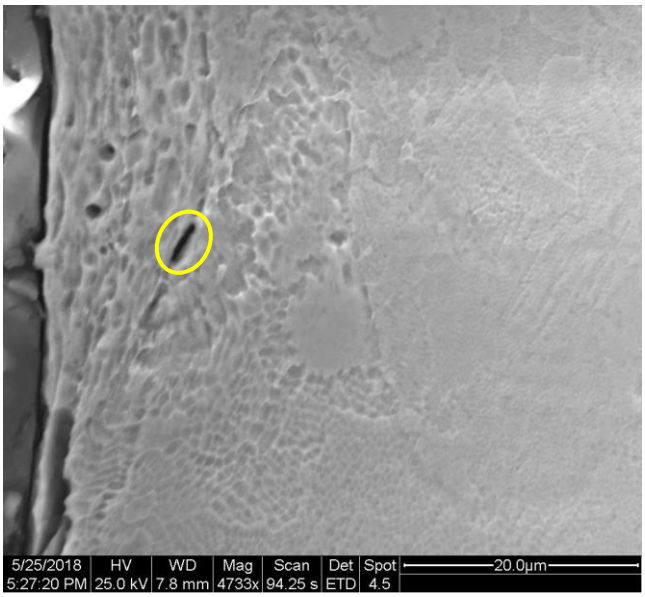

Figure 84: Grain deformation and near-surface pore collapse (yellow circle) can be observed here, at 4733x.

The collapse of near-surface porosity is not as significant of an advantage as the hardening or surface roughness reduction effects, but a valuable benefit for the processing of additively manufactured components. According to the Hall-Petch effect, strength is inversely proportional to grain size. Although the grains were enlarged by USP, the hardness increased significantly. Thus, the dislocation density compressive stresses on the surface must have increased substantially to yield an increase hardness. AT even higher magnifications, the grain deformation is even more apparent (Figure 84).

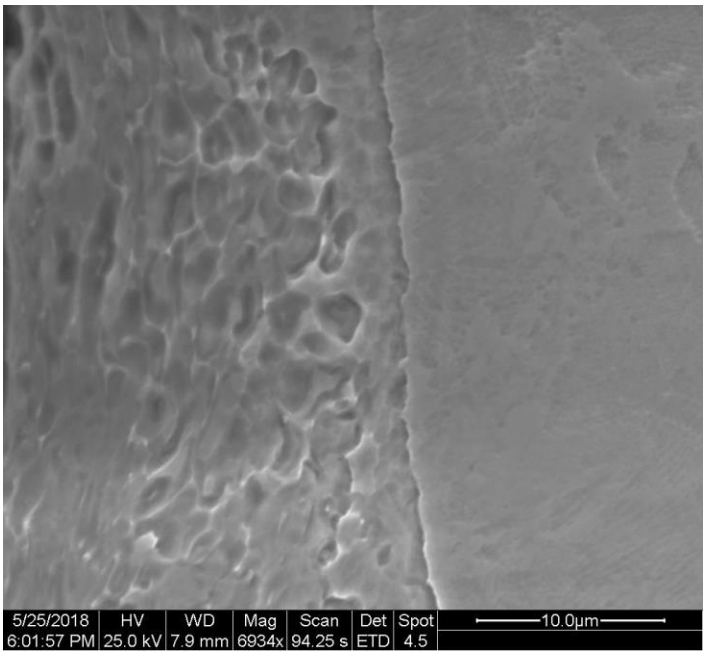

Figure 85: Deformed grains comprise a layer distinct from the base material.

Chapter V – Discussion and Conclusions

At the onset of this research, the invention or discovery of a universal post-processing technique for SLM alloys was the goal. It quickly became apparent that the likelihood of the existence of one process to unilaterally solve all material issues with SLM is extremely low. The nature of engineering requires careful selection of processes that match specific requirements. This concept is especially important for solving the issue of post-processing additively manufactured components. As such, it is paramount that engineers become exposed to the library of available processes for additively manufactured components. Rather than process development of one universal technique, engineers must shift their focus to understanding the breadth and variety of post-processing solutions available. Abrasive flow machining and ultrasonic shot peening accomplish similar post-processing goals but achieve these feats in radically different manners. As such, the goal of the experimentation of this Thesis has been to evaluate these processes as tools for improving the as-built properties of selective laser melted alloys. Significant focus has been placed on surface finish, but other effects such as material removal, dimensional stability, and hardening effects have been considered as well. Numerous advantages and disadvantages of each process has been identified herein; all results of this research must be synthesized to produce relevant and rational recommendations for these processes as tools for the additive manufacturing industry.

Compared to virtually any other process, abrasive flow machining excels at the polishing of interior surfaces. The achievement of 1 μm Ra or less on internal features represents a significant victory for the process. When geometry is not prohibitive, SLM manufactured components can be polished to mirror-like finishes in minutes or hours. This polishing also comes without significant cost; there are few dangers of this process as it relates to the mechanical or corrosion properties of the alloy. As a flow driven process, it struggles with the uniform polishing of complex passages, especially passages that contain internal chambers and expanding cross-sections. Angular features will experience rounding and significant variability in final finish will exist for internal features of changing cross-sectional area. From the dimensional measurements of this study it is clear that material removal can be predictable for a specific

flow rate and passage geometry. When multiple passages are processed at once, however, the determination of the material removal rate can be challenging. Parts with multiple passages in need of polishing should thus be processed one at a time. AFM is also entirely unsuitable for the polishing of exterior surfaces. Therefore, for most AM applications, AFM is not a potential solution for finishing of the entire component. Nonetheless, for additively manufactured components with internal passages, especially passages designed for fluid flow, AFM is a clear frontrunner (Figure 85).

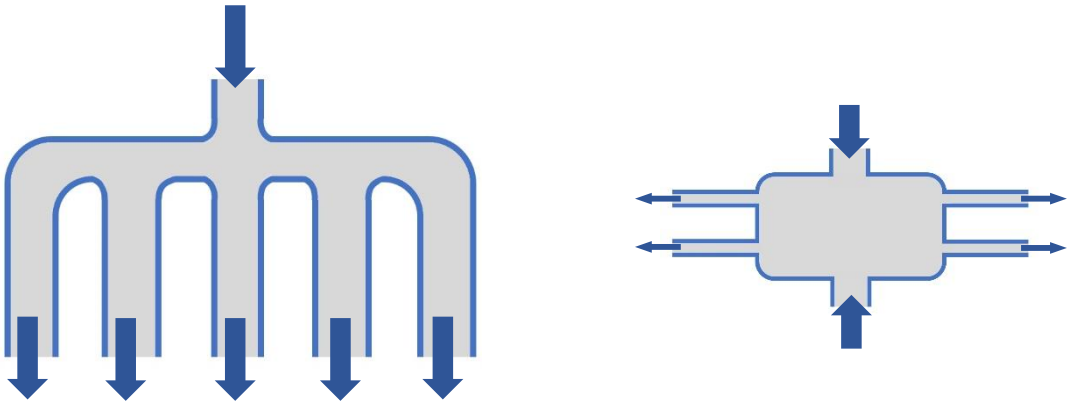

Figure 86: Left: An SLM produced manifold like this represents an ideal geometry for AFM polishing. Right: This combustion chamber design would achieve successful polishing of inlets and outlets, but the chamber itself may be difficult to polish entirely. The manifold design would be polished with one-way AFM whereas the combustion chamber could be polished with two-way AFM.

Abrasive flow machining balances its ability to achieve sub-1 µm finishes with reasonable cost and ease of use. The results of the lattice polishing study are inconclusive. The entrapment of polishing media within the lattice structure severely limits its potential use for this application. For lattice components without a surrounding solid skin, AFM will perform better according to *Extrude Hone*. Removing entrapped media with an acetone soak also proves simple yet effective for exposed un-skinned lattice geometries. No evidence suggests AFM damages the compressive strength of the lattice. Additional testing may reveal that the process indeed improves the strength of the lattice because of parasitic powder removal. Further study on the applicability of AFM, or required process modifications, to polish complex lattice components is recommended.

Although ultrasonic shot peening cannot reach the sub-1 μm surface finishes AFM can, USP is a much more versatile process. In addition to surface roughness reduction, USP can also induce beneficial compressive stresses to collapse near-surface pores and increase hardness. USP can process both exterior and interior surfaces. Although the process does have some line-of-sight constraints, ricochet of media can allow for the finishing of complex internal features in some circumstances. Features, however complex, must be properly angled so the media can strike the surface. The hardening effect formed because of high dislocation density on deformed grains of the peened surface. Steel balls, due to higher mass and kinetic energy, are more effective at hardening than ceramic media is. The lack of material removal, too, makes USP competitive. Because its finishing mechanism relies on the compression of material at the surface, the dimensions of the part after USP are close to the digital CAD model dimensions.

Overall, AFM and USP have both been concluded to be suitable post-processing solutions for additively manufactured alloys. When employed properly, these techniques can dramatically improve surface finish. A comparison of these processes' advantages, disadvantages, and capabilities is presented (Table XXV)

Table 26: Process Capability Summary

Capability	AFM	USP
Exterior Surfaces	Not Applicable	$\bar{x}$=2.06 μm Ra, s= 0.20 MIN= 1.71 μm, MAX = 2.51 μm[1]
Standard Interior Surfaces	$\bar{x}$=1.07 μm Ra, s= 1.08 MIN= 0.17 μm, MAX = 4.33 μm	$\bar{x}$=6.77 μm Ra, s= 3.87 MIN= 2.17 μm, MAX= 13.88 μm[2]
Dimensional Stability	0.010" to 0.035" removed from passages after processing. Highly geometry and flow dependent.	0.0050" to 0.0075" deviation from CAD model after processing. Geometry dependent. Material not removed but compressed.
Hardening Effect	Not Applicable	As Built: 105.7 HRB USP: 112.7 HRB[3]

Support Structure Stubs	Not Investigated	Partial Removal
Lattice Processing	Inconclusive	Not Applicable

1: Data from USP Specimen II (Steel Media)
2: Data from USP Specimen II (Steel Media)
3. Data from USP Specimen II (Steel Media)

The consistency of these processes is another valuable characteristic to consider. The low variation of USP processing is certainly worth noting. With a standard deviation of only 0.20, the process consistently peened various external surfaces to similar final finishes, even though the starting roughnesses were not equal. The geometric dependence of USP, however, means that internal passages experienced much larger variation with a standard deviation of 3.87. AFM, with a standard deviation of 1.07, yielded consistent results for simple geometries, but struggled to polish expanding passages or offset cavities.

Both processes are not universal; good engineering judgment is required to determine when to use AFM or USP. Moreover, much as DFAM has encouraged engineers to design components specifically for additive manufacturing, these results now encourage engineers to consider post-processing methods when designing AM parts.

5.1 Conclusions

At the culmination of this Thesis, conclusions for the effectiveness of abrasive flow machining and ultrasonic shot peening as processes for improving the surface finish of SLM manufactured alloys have been developed.

5.1.1 Abrasive Flow Machining

1. AFM achieved, on average, 1.07 μm finish for all 9 passages. In some areas, 0.1 - 0.2 μm was achieved. Difficult to reach regions, such as expanded areas or offset cavities, were hardly polished and remained in the 10 – 15 μm finish range of the as-built material.

2. All nine passages expanded significantly after AFM processing. Material removal differed from passage to passage because of different flow rates and pressures. No correlation between material removal and final finish was discovered.
3. For round internal geometries already designed for fluid flow, AFM is the perfect process for the surface finishing of SLM manufactured components. The process is unsuitable for any exterior surfaces, angular geometries, or rapidly expanding/contracting cross-sections. The process may be suitable for the polishing of lattice structures, but further research is required.

5.1.2 Ultrasonic Shot Peening

1. For exterior surfaces, USP successfully reduced the as-built surface to 2.22 and 2.06 μm for with ceramic and steel media, respectively. The variation from surface to surface was also low, with consistent data.
2. USP partially peened internal features, reducing the surface finish, on average to 8 μm. However, the peening of internal features proved to be geometry dependent. Straight through and expanding geometry prevented media contact with the surface, limiting the process effects. Sufficiently angled geometry was peened successfully.
3. Both ceramic and steel media increased the hardness of the double hexagon test coupons. Peening with steel media, as a result of its increased mass (and therefore increased kinetic energy) increased the hardness significantly more than ceramic media did.

USP and AFM should both be included in engineers' toolset for the surface finishing of additively manufactured components. Together, these two processes can solve a wide variety of AM related issues. It is highly unlikely that a universal post-processing method will ever be employed for SLM produced components of varying geometries. USP and AFM are indeed a step in the right direction.

References

ABRASIVE FLOW MACHINING (AFM) - Extrude Hone. (n.d.). Retrieved November 11, 2017, from https://extrudehone.com/products/abrasive-flow-machining-afm

Amanov, A., & Pyun, Y.-S. (n.d.). A comprehensive review of nanostructured materials by ultrasonic nanocrystal surface modification technique. https://doi.org/10.1049/joe.2015.0067

ASTM International. (2013). F2792-12a - Standard Terminology for Additive Manufacturing Technologies. *Rapid Manufacturing Association*, 10–12. https://doi.org/10.1520/F2792-12A.2

Attaran, M. (2017). The rise of 3-D printing: The advantages of additive manufacturing over traditional manufacturing. *Business Horizons*, *60*(5), 677–688. https://doi.org/10.1016/j.bushor.2017.05.011

Blade Supercar - Divergent. (n.d.). Retrieved November 21, 2017, from http://www.divergent3d.com/blade-supercar/

DebRoy, T., Wei, H. L., Zuback, J. S., Mukherjee, T., Elmer, J. W., Milewski, J. O., … Zhang, W. (2018). Additive manufacturing of metallic components – Process, structure and properties. *Progress in Materials Science*, *92*, 112–224. https://doi.org/10.1016/j.pmatsci.2017.10.001

Dr. Shashank Shektar. (2012). Phases and Microstructure, 22–23.

EPMA. (2013). Introduction to Additive Manufacturing Technology. *Epma*, 42.

Gong, H., Gu, H., Zeng, K., Dilip, J. J. S., Pal, D., Stucker, B., … Lewandowski, J. J. (n.d.). Melt Pool Characterization for Selective Laser Melting of Ti-6Al-4V Pre-alloyed Powder.

Gong, H., Rafi, K., Gu, H., Starr, T., & Stucker, B. (2014). Analysis of defect generation in Ti-6Al-4V parts made using powder bed fusion additive manufacturing processes. *Additive Manufacturing*, *1*, 87–98. https://doi.org/10.1016/j.addma.2014.08.002

Gorsse, S., Hutchinson, C., Gouné, M., & Banerjee, R. (2017). Additive manufacturing of metals: a brief review of the characteristic microstructures and properties of steels, Ti-6Al-4V and high-entropy

alloys. *Science and Technology of Advanced Materials*, *18*(1), 584–610. https://doi.org/10.1080/14686996.2017.1361305

Hällgren, S., Pejryd, L., & Ekengren, J. (2016). (Re)Design for Additive Manufacturing. *Procedia CIRP*, *50*, 246–251. https://doi.org/10.1016/j.procir.2016.04.150

Hebert, R. J. (2016). Viewpoint: metallurgical aspects of powder bed metal additive manufacturing. *Journal of Materials Science*, *51*(3), 1165–1175. https://doi.org/10.1007/s10853-015-9479-x

Hummel, R. E. (1999). *Understanding Materials Science*. *IEEE Electrical Insulation Magazine* (Vol. 15). https://doi.org/10.1109/MEI.1999.768569

Kaddar, W. (2010). Die generative Fertigung mittels Laser-Sintern : Scanstrategien , Einflüsse verschiedener Prozessparameter auf Thermoplasten und deren Nachbearbeitungsmöglichkeiten, (November), 1–146.

Kar, K. K., Ravikumar, N. L., Tailor, P. B., Ramkumar, J., & Sathiyamoorthy, D. (2009a). Performance evaluation and rheological characterization of newly developed butyl rubber based media for abrasive flow machining process. *Journal of Materials Processing Technology*, *209*(4), 2212–2221. https://doi.org/10.1016/j.jmatprotec.2008.05.012

Kar, K. K., Ravikumar, N. L., Tailor, P. B., Ramkumar, J., & Sathiyamoorthy, D. (2009b). Preferential Media for Abrasive Flow Machining. *Journal of Manufacturing Science and Engineering*, *131*(1), 11009. https://doi.org/10.1115/1.3046135

Kasperovich, G., Haubrich, J., Gussone, J., & Requena, G. (2016). Correlation between porosity and processing parameters in TiAl6V4 produced by selective laser melting. *Materials and Design*, *105*, 160–170. https://doi.org/10.1016/j.matdes.2016.05.070

Kheradmandfard, M., Kashani-Bozorg, S. F., Kim, C. L., Hanzaki, A. Z., Pyoun, Y. S., Kim, J. H., … Kim, D. E. (2017). Nanostructured β-type titanium alloy fabricated by ultrasonic nanocrystal surface modification. *Ultrasonics Sonochemistry*, *39*(May), 698–706.

https://doi.org/10.1016/j.ultsonch.2017.03.061

Kou, S. (2003). *Metallurgy Second Edition Welding Metallurgy*. *Structure* (Vol. 822). https://doi.org/10.1016/j.theochem.2007.07.017

Kumar, S. S., & Hiremath, S. S. (2016). A Review on Abrasive Flow Machining (AFM). *Procedia Technology*, *25*(Raerest), 1297–1304. https://doi.org/10.1016/j.protcy.2016.08.224

Kurzynowski, T., Gruber, K., Stopyra, W., Kuźnicka, B., & Chlebus, E. (2018). Correlation between process parameters, microstructure and properties of 316 L stainless steel processed by selective laser melting. *Materials Science and Engineering A*, *718*(December 2017), 64–73. https://doi.org/10.1016/j.msea.2018.01.103

Lab researchers achieve breakthrough in 3D printed marine grade stainless steel | Lawrence Livermore National Laboratory. (n.d.). Retrieved November 21, 2017, from https://www.llnl.gov/news/lab-researchers-achieve-breakthrough-3d-printed-marine-grade-stainless-steel

Laser Melting - Additively. (n.d.). Retrieved November 11, 2017, from https://www.additively.com/en/learn-about/laser-melting

Launhardt, M., Wörz, A., Loderer, A., Laumer, T., Drummer, D., Hausotte, T., & Schmidt, M. (2016). Detecting surface roughness on SLS parts with various measuring techniques. *Polymer Testing*, *53*, 217–226. https://doi.org/10.1016/j.polymertesting.2016.05.022

Lavery, N. P., Cherry, J., Mehmood, S., Davies, H., Girling, B., Sackett, E., … Sienz, J. (2017). Effects of hot isostatic pressing on the elastic modulus and tensile properties of 316L parts made by powder bed laser fusion. *Materials Science and Engineering A*, *693*(March), 186–213. https://doi.org/10.1016/j.msea.2017.03.100

Li, C., Liu, J. F., & Guo, Y. B. (2016). Prediction of Residual Stress and Part Distortion in Selective Laser Melting. *Procedia CIRP*, *45*, 171–174. https://doi.org/10.1016/j.procir.2016.02.058

Li, S. J., Xu, Q. S., Wang, Z., Hou, W. T., Hao, Y. L., Yang, R., & Murr, L. E. (2014). Influence of cell shape on

mechanical properties of Ti-6Al-4V meshes fabricated by electron beam melting method. *Acta Biomaterialia*, *10*(10), 4537–4547. https://doi.org/10.1016/j.actbio.2014.06.010

Liu, G., Lu, J., & Lu, K. (2000). Surface nanocrystallization of 316L stainless steel induced by ultrasonic shot peening. *Materials Science and Engineering: A*, *286*(1), 91–95. https://doi.org/10.1016/S0921-5093(00)00686-9

Liu, Q. C., Elambasseril, J., Sun, S. J., Leary, M., Brandt, M., & Sharp, P. K. (2014). The Effect of Manufacturing Defects on the Fatigue Behaviour of Ti-6Al-4V Specimens Fabricated Using Selective Laser Melting. *Advanced Materials Research*, *891–892*, 1519–1524. https://doi.org/10.4028/www.scientific.net/AMR.891-892.1519

Liverani, E., Toschi, S., Ceschini, L., & Fortunato, A. (2017). Effect of selective laser melting (SLM) process parameters on microstructure and mechanical properties of 316L austenitic stainless steel. *Journal of Materials Processing Technology*, *249*(June), 255–263. https://doi.org/10.1016/j.jmatprotec.2017.05.042

Ma, C., Dong, Y., & Ye, C. (2016). Improving Surface Finish of 3D-printed Metals by Ultrasonic Nanocrystal Surface Modification. *Procedia CIRP*, *45*, 319–322. https://doi.org/10.1016/j.procir.2016.02.339

Mahmoud, D., & Elbestawi, M. (2017). Lattice Structures and Functionally Graded Materials Applications in Additive Manufacturing of Orthopedic Implants: A Review. *Journal of Manufacturing and Materials Processing*, *1*(2), 13. https://doi.org/10.3390/jmmp1020013

Mazur, M., Leary, M., McMillan, M., Sun, S., Shidid, D., & Brandt, M. (2016). *Mechanical properties of Ti6Al4V and AlSi12Mg lattice structures manufactured by Selective Laser Melting (SLM)*. *Laser Additive Manufacturing: Materials, Design, Technologies, and Applications*. Elsevier Ltd. https://doi.org/10.1016/B978-0-08-100433-3.00005-1

Mercelis, P., & Kruth, J. (2006). Residual stresses in selective laser sintering and selective laser melting. *Rapid Prototyping Journal*, *12*(5), 254–265. https://doi.org/10.1108/13552540610707013

Mohammadian, N., Turenne, S., & Brailovski, V. (2017). Surface finish control of additively-manufactured Inconel 625 components using combined chemical-abrasive flow polishing. *Journal of Materials Processing Technology*. https://doi.org/10.1016/j.jmatprotec.2017.10.020

Murr, L. E., Martinez, E., Amato, K. N., Gaytan, S. M., Hernandez, J., Ramirez, D. A., … Wicker, R. B. (2012). Fabrication of metal and alloy components by additive manufacturing: Examples of 3D materials science. *Journal of Materials Research and Technology*, *1*(1), 42–54. https://doi.org/10.1016/S2238-7854(12)70009-1

Prashanth, K. G., & Eckert, J. (2017). Formation of metastable cellular microstructures in selective laser melted alloys. *Journal of Alloys and Compounds*, *707*, 27–34. https://doi.org/10.1016/j.jallcom.2016.12.209

Precision Devices, Inc. · 606 County Street · P.O. Box 220 · Milan, M. 48160. (2013). Surface Roughness Terminology and Parameters. *3975-Op Parameter Definitions*. Retrieved from www.predev.com/pdffiles/surface_roughness_terminology_and_parameters.pdf

Presentation, P. (n.d.). PROCESS BY ULTRASONIC SHOT NANOCRYSTALLIZATION PROCESS BY, 1–2.

Raghavan, S., Zhang, B., Wang, P., Sun, C.-N., Nai, M. L. S., Li, T., & Wei, J. (2016). Effect of different heat treatments on the microstructure and mechanical properties in selective laser melted INCONEL 718 alloy. *Materials and Manufacturing Processes*, *0*(0), 1–8. https://doi.org/10.1080/10426914.2016.1257805

Ravi Sankar, M., Jain, V. K., Ramkumar, J., & Joshi, Y. M. (2011). Rheological characterization of styrene-butadiene based medium and its finishing performance using rotational abrasive flow finishing process. *International Journal of Machine Tools and Manufacture*, *51*(12), 947–957. https://doi.org/10.1016/j.ijmachtools.2011.08.012

Rhoades, L. (1991). Abrasive flow machining: a case study. *Journal of Materials Processing Tech.*, *28*(1–2), 107–116. https://doi.org/10.1016/0924-0136(91)90210-6

Sachdeva, A., Singh, S., & Sharma, V. S. (n.d.). Investigating surface roughness of parts produced by SLS process. https://doi.org/10.1007/s00170-012-4118-z

Saeidi, K., Gao, X., Zhong, Y., & Shen, Z. J. (2015). Hardened austenite steel with columnar sub-grain structure formed by laser melting. *Materials Science and Engineering A*, *625*, 221–229. https://doi.org/10.1016/j.msea.2014.12.018

Salmi, A., Atzeni, E., Iuliano, L., & Galati, M. (2017). Experimental Analysis of Residual Stresses on AlSi10Mg Parts Produced by Means of Selective Laser Melting (SLM). *Procedia CIRP*, *62*, 458–463. https://doi.org/10.1016/j.procir.2016.06.030

Sames, W. J., List, F. A., Pannala, S., Dehoff, R. R., & Babu, S. S. (2016). The metallurgy and processing science of metal additive manufacturing. *International Materials Reviews*. https://doi.org/10.1080/09506608.2015.1116649

Schmidt, M., Merklein, M., Bourell, D., Dimitrov, D., Hausotte, T., Wegener, K., … Levy, G. N. (2017). Laser based additive manufacturing in industry and academia. *CIRP Annals*, *66*(2), 561–583. https://doi.org/10.1016/j.cirp.2017.05.011

Simson, T., Emmel, A., Dwars, A., & Böhm, J. (2017). Residual stress measurements on AISI 316L samples manufactured by selective laser melting. *Additive Manufacturing*, *17*, 183–189. https://doi.org/10.1016/j.addma.2017.07.007

Sing, S. L., Wiria, F. E., & Yeong, W. Y. (2018). Selective laser melting of lattice structures: A statistical approach to manufacturability and mechanical behavior. *Robotics and Computer-Integrated Manufacturing*, *49*(June 2017), 170–180. https://doi.org/10.1016/j.rcim.2017.06.006

Tang, M. (2017). Inclusions, Porosity, and Fatigues of AlSi10Mg Parts Produced by Selective Laser Melting. *PhD Dissertation*.

Thompson, M. K., Moroni, G., Vaneker, T., Fadel, G., Campbell, R. I., Gibson, I., … Martina, F. (2016). Design for Additive Manufacturing: Trends, opportunities, considerations, and constraints. *CIRP*

Annals - Manufacturing Technology, *65*(2). https://doi.org/10.1016/j.cirp.2016.05.004

Townsend, A., Senin, N., Blunt, L., Leach, R. K., & Taylor, J. S. (2016). Surface texture metrology for metal additive manufacturing: a review. *Precision Engineering*, *46*, 34–47. https://doi.org/10.1016/j.precisioneng.2016.06.001

Tricoire, J. (2016). Process Review: Ultrasonic Shot Peening, Sonats | www.sonats-com.

Uhlmann, E., Schmiedel, C., & Wendler, J. (2015). CFD simulation of the Abrasive Flow Machining process. *Procedia CIRP*, *31*, 209–214. https://doi.org/10.1016/j.procir.2015.03.091

Uns, S., & Nr, S. W. (2014). Specification Sheet : Alloy 316 / 316L, (1), 9–11.

Venkatesh, G., Sharma, A. K., singh, N., & kumar, P. (2014). Finishing of Bevel Gears using Abrasive Flow Machining. *Procedia Engineering*, *97*, 320–328. https://doi.org/10.1016/j.proeng.2014.12.255

Wang, a. C., Liu, C. H., Liang, K. Z., & Pai, S. H. (2007). Study of the rheological properties and the finishing behavior of abrasive gels in abrasive flow machining. *Journal of Mechanical Science and Technology*, *21*, 1593–1598. https://doi.org/10.1007/BF03177380

Wang, X., Fu, Y., & Gao, H. (n.d.). Finishing of Additively Manufactured Metal Parts by Abrasive Flow Machining. Retrieved from https://sffsymposium.engr.utexas.edu/sites/default/files/2016/197-Wang.pdf

Wang, X., Wraith, M., Burke, S., Rathbun, H., & DeVlugt, K. (2016). Densification of W-Ni-Fe powders using laser sintering. *International Journal of Refractory Metals and Hard Materials*, *56*, 145–150. https://doi.org/10.1016/j.ijrmhm.2016.01.006

Xu, J., Rong, Y., Huang, Y., Wang, P., & Wang, C. (2018). Keyhole-induced porosity formation during laser welding. *Journal of Materials Processing Technology*, *252*(July 2017), 720–727. https://doi.org/10.1016/j.jmatprotec.2017.10.038

Zhang, B., Li, Y., & Bai, Q. (2017). Defect Formation Mechanisms in Selective Laser Melting: A Review.

Chinese Journal of Mechanical Engineering, *30*(3), 515–527. https://doi.org/10.1007/s10033-017-0121-5

Zhang, M., Liu, C., Shi, X., Chen, X., Chen, C., Zuo, J., … Ma, S. (2016). Residual Stress, Defects and Grain Morphology of Ti-6Al-4V Alloy Produced by Ultrasonic Impact Treatment Assisted Selective Laser Melting. *Applied Sciences*, *6*(11), 304. https://doi.org/10.3390/app6110304

Zhou, X., Liu, X., Zhang, D., Shen, Z., & Liu, W. (2015). Balling phenomena in selective laser melted tungsten. *Journal of Materials Processing Technology*, *222*, 33–42. https://doi.org/10.1016/j.jmatprotec.2015.02.032

Zhu, L., Guan, Y., Wang, Y., Xie, Z., Lin, J., & Zhai, J. (2017). Influence of process parameters of ultrasonic shot peening on surface roughness and hydrophilicity of pure titanium. *Surface and Coatings Technology*, *317*, 38–53. https://doi.org/10.1016/j.surfcoat.2017.03.044

Appendices

A. Double Hexagon Test Coupon Drawing

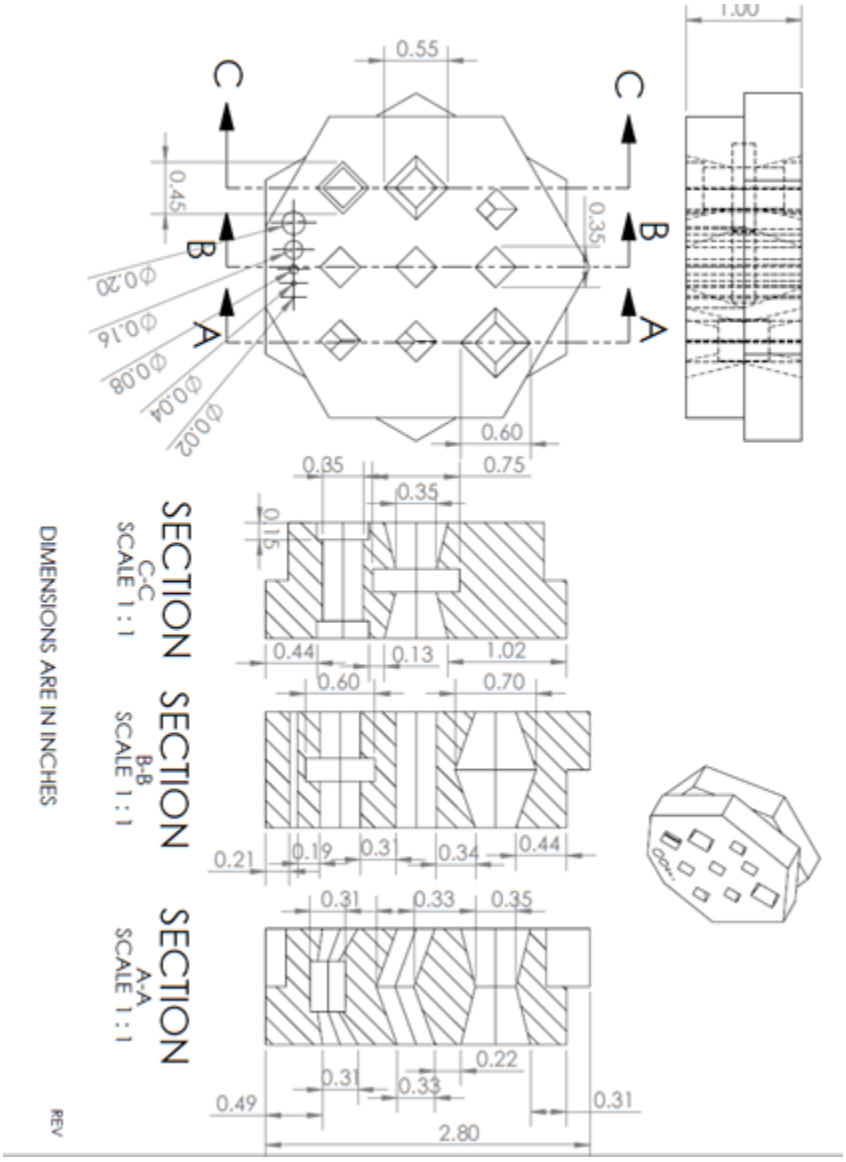

B. Double Hexagon Test Coupon Surface Designations

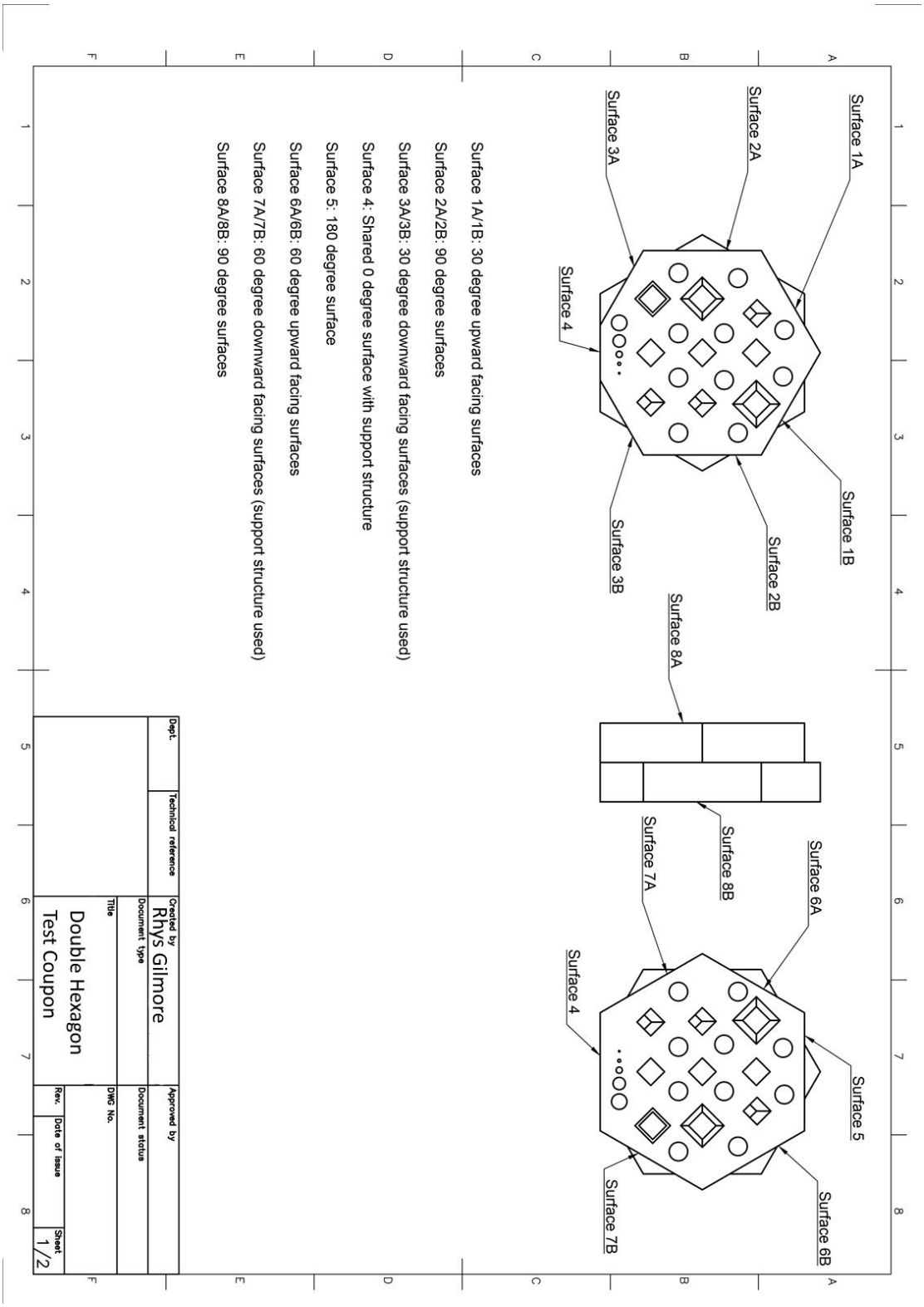

C. Thin Disk Lattice Test Coupon Drawing

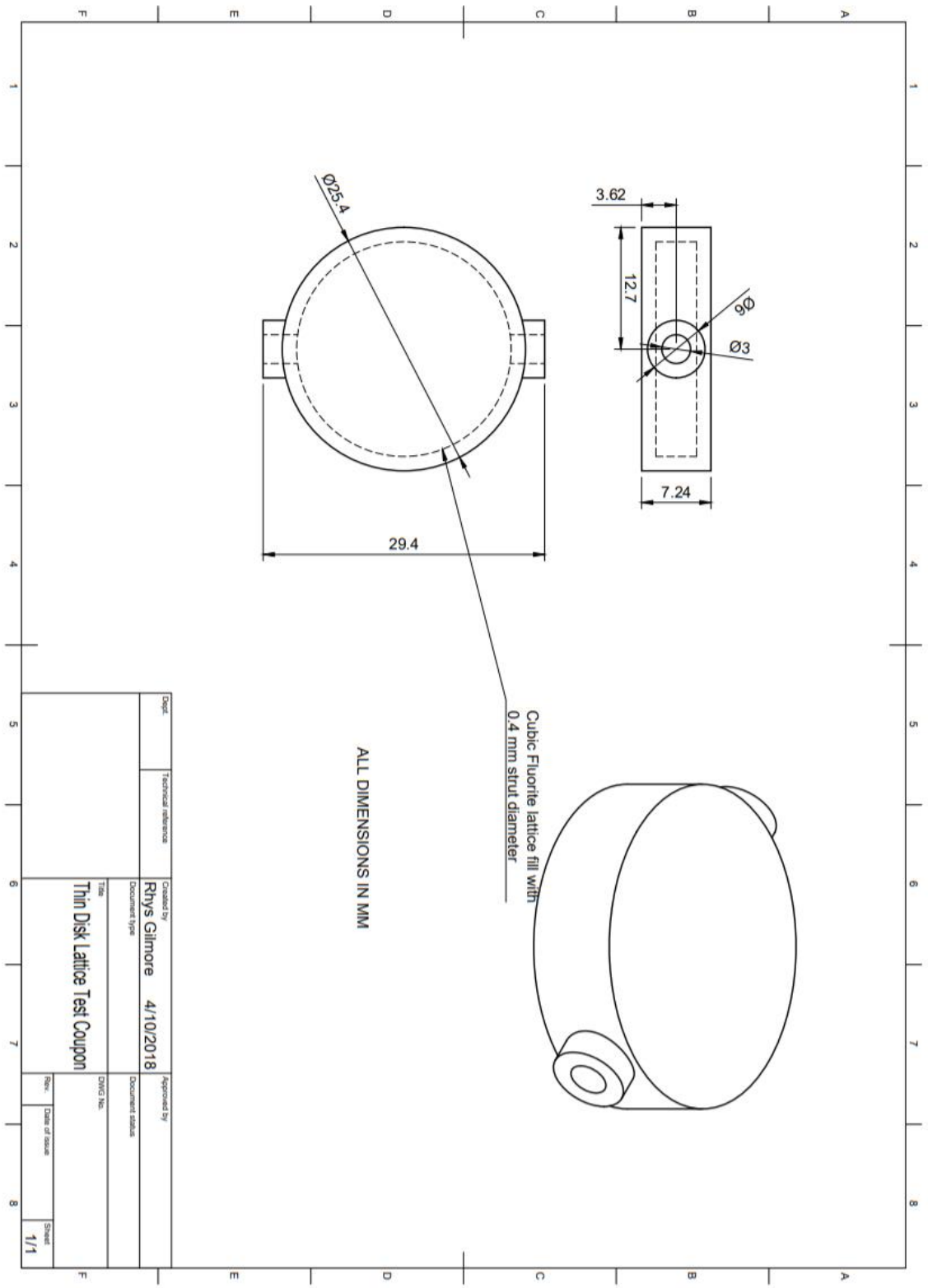

D. USP Hardness Measurements

Table A. I: USP Hardness Measurements

As-Built (HRB)	Specimen 1 (HRB)	Specimen 2 (HRB)
104.6	107.3	114.5
108.2	105.7	115.4
105.5	112.1	113.8
107.7	111.2	111.1
107.0	110.1	112.9
106.6	102.3	112.5
102.0	109.9	114.4
105.0	109.1	107.8
106.4	111.2	111.9
109.5	111.1	113.1
99.8		
105.7		
$\bar{x}$ = 105.67, s = 2.661	**$\bar{x}$ = 109.00, s = 3.060**	**$\bar{x}$ = 112.74, s = 2.162**

E. As-Built Exterior Profilometry

1A		1B		2A		2B		5		6A		6B		8A		8B		
Ra (µm)	Rz (µm)	Ra (µm)	Rz (µm)	Ra (µm)	Rz (µm)	Ra (µm)	Rz (µm)	Ra (µm)	Rz (µm)	Ra (µm)	Rz (µm)	Ra (µm)	Rz (µm)	Ra (µm)	Rz (µm)	Ra (µm)	Rz (µm)	
12.26	84.66	12.55	88.7	16.8	97.5	12.26	71.7	5.82	27.95	13.65	90.3	15.17	6B	16.92	105.1	14.22	87.42	
16.02	112.8	12.68	78.37	14.83	92.58	13.21	82.52	4.58	23.49	17.92	109.8	17.6	90.91	13.14	84.99	13.54	75.77	
16	96.97	14.38	96.97	16.62	104.5	13.25	84.75	5.08	25.18	16.48	102.5	15.97	112.1	11.58	76.55	13.04	80.87	
14.76	**98.14**	**13.20**	**88.01**	**16.08**	**98.19**	**12.91**	**79.66**	**5.16**	**25.54**	**16.02**	**100.87**	**16.25**	**100.57**	**13.88**	**70.33**	**13.60**	**81.35**	$\bar{x}$
2.17	**14.11**	**1.02**	**9.32**	**1.09**	**5.99**	**0.56**	**6.98**	**0.62**	**2.25**	**2.17**	**9.85**	**1.24**	**10.72**	**2.75**	**14.67**	**0.59**	**5.84**	**s**

F. As-Built Interior Profilometry, Ra (μm)

Passage 1		Passage 2		Passage 4		Passage 5		
Upward	Downward	Upward	Downward	Upward	Downward	Upward	Downward	
13.95	14.10	14.88	17.13	10.92	17.71	12.71	17.49	
13.48	13.98	11.86	13.09	11.44	18.34	14.74	15.61	
10.28	15.63	12.3	14.54	11.23	17.39	12.64	14.89	
10.28	15.04	10.28	14.99	13.67	15.43	12.63	15.41	
14.3	14.99	10.63	16.28	14.12	16.15	14.36	17.26	
13.26	15.52	12.52	14.24	12.71	15.32	10.71	14.88	
12.59	**14.88**	**12.08**	**15.05**	**12.35**	**16.72**	**12.97**	**15.92**	$\bar{x}$
1.83	**0.70**	**1.64**	**1.46**	**1.35**	**1.27**	**1.45**	**1.16**	**s**

G. As-Built Interior Profilometry, Rz (μm)

Passage 1		**Passage 2**		**Passage 4**		**Passage 5**		
Upward	Downward	Upward	Downward	Upward	Downward	Upward	Downward	
13.95	14.10	14.88	17.13	10.92	17.71	12.71	17.49	
13.48	13.98	11.86	13.09	11.44	18.34	14.74	15.61	
10.28	15.63	12.3	14.54	11.23	17.39	12.64	14.89	
10.28	15.04	10.28	14.99	13.67	15.43	12.63	15.41	
14.3	14.99	10.63	16.28	14.12	16.15	14.36	17.26	
13.26	15.52	12.52	14.24	12.71	15.32	10.71	14.88	
12.59	**14.88**	**12.08**	**15.05**	**12.35**	**16.72**	**12.97**	**15.92**	$\bar{x}$
1.83	**0.70**	**1.64**	**1.46**	**1.35**	**1.27**	**1.45**	**1.16**	**s**

H. USP Exterior Profilometry, Specimen I

1A		1B		2A		2B		5		6A		6B		8A		8B		
Ra (µm)	Rz (µm)	Ra (µm)	Rz (µm)	Ra (µm)	Rz (µm)	Ra (µm)	Rz (µm)	Ra (µm)	Rz (µm)	Ra (µm)	Rz (µm)	Ra (µm)	Rz (µm)	Ra (µm)	Rz (µm)	Ra (µm)	Rz (µm)	
2.58	12.49	2.33	12.16	2.29	12.66	2.13	14.41	1.83	7.62	2.63	11.85	2.15	13.16	1.96	10.41	2.36	12.03	
2.35	9.83	1.85	9.72	2.28	11.44	2.86	16.53	1.93	8.12	2.62	3.11	2.74	14.02	1.84	8.91	2.59	12.74	
1.99	8.83	2.02	9.86	2.46	14.56	2.03	10.68	1.93	8.66	2.16	12.07	2.37	11.61	2.07	10.85	1.65	9.87	
2.31	**10.38**	**2.07**	**10.58**	**2.34**	**12.89**	**2.34**	**13.87**	**1.90**	**8.13**	**2.47**	**9.01**	**2.42**	**12.93**	**1.96**	**10.06**	**2.20**	**11.55**	$\bar{x}$
0.30	**1.89**	**0.24**	**1.37**	**0.10**	**1.57**	**0.45**	**2.96**	**0.06**	**0.52**	**0.27**	**5.11**	**0.30**	**1.22**	**0.12**	**1.02**	**0.49**	**1.49**	**s**

I. USP Exterior Profilometry, Specimen II

1A		1B		2A		2B		5		6A		6B		8A		8B		
Ra (µm)	Rz (µm)	Ra (µm)	Rz (µm)	Ra (µm)	Rz (µm)	Ra (µm)	Rz (µm)	Ra (µm)	Rz (µm)	Ra (µm)	Rz (µm)	Ra (µm)	Rz (µm)	Ra (µm)	Rz (µm)	Ra (µm)	Rz (µm)	
1.70	8.55	1.43	9.34	1.95	9.47	2.60	12.19	2.34	10.53	1.67	8.09	2.15	9.63	2.05	10.98	1.95	9.6	
2.49	10.82	1.84	11.18	1.64	8.12	2.43	11.09	2.17	10.45	1.63	9.19	2.32	12.56	2.09	10.16	1.75	9.42	
1.81	8.07	2.17	10.73	1.93	9.91	2.50	12.99	2.57	13.15	1.84	9.41	2.11	11.39	2.24	10.22	2.13	9.14	
2.00	**9.15**	**1.81**	**10.42**	**1.84**	**9.17**	**2.51**	**12.09**	**2.36**	**11.38**	**1.71**	**8.90**	**2.19**	**11.19**	**2.13**	**10.45**	**1.94**	**9.39**	$\bar{x}$
0.43	**1.47**	**0.37**	**0.96**	**0.17**	**0.93**	**0.09**	**0.95**	**0.20**	**1.54**	**0.11**	**0.71**	**0.11**	**1.47**	**0.10**	**0.46**	**0.19**	**0.23**	**s**

J. USP Interior Profilometry, Specimen II, Ra (μm)

Passage 1		**Passage 2**		**Passage 4**		**Passage 5**		**Passage 6**		**Passage 7**		**Passage 8**		**Passage 9**	
Up - ward	Down - ward	Up - ward	Down - ward	Up - ward	Down - ward	Up - ward	Down - ward	Up - ward	Down - ward	Up - ward	Down - ward	Up - ward	Down - ward	Up - ward	Down - ward
3.78	7.84	4.39	13.57	3.52	5.79	4.44	14.61	5.28	7.35	3.69	8.21	4.76	14.45	1.86	3.92
4.88	8.46	2.77	13.87	1.98	6.91	4.27	11.49	6.93	7.4	4.8	8.15	4.75	12.27	2.07	4.02
2.73	8.7	2.96	12.41	2.45	5.87	5.18	14.44	3.91	8.84	4.58	9.92	6.71	14.92	2.57	6.53

K. USP Interior Profilometry, Specimen II, Rz (μm)

Passage 1		**Passage 2**		**Passage 4**		**Passage 5**		**Passage 6**		**Passage 7**		**Passage 8**		**Passage 9**	
Up - ward	Down - ward	Up - ward	Down - ward	Up - ward	Down - ward	Up - ward	Down - ward	Up - ward	Down - ward	Up - ward	Down - ward	Up - ward	Down - ward	Up - ward	Down - ward
19.24	46.17	21.75	65.45	20.38	39.65	21.88	67.57	26.17	41.24	16.73	44.53	23.71	76.97	10.59	24.82
24.57	46.06	14.53	69.13	9.7	39.58	19.58	58.13	36.93	41.57	24.86	45.2	23.21	62.07	13.36	25.88
13.96	44.11	14.21	60.26	12.99	34.36	25.34	75.98	22.69	44.34	18.79	56	23.24	75.11	13.49	41.57

L. AFM Interior Profilometry, Ra (μm)

Passage 1		**Passage 2**		**Passage 3**		**Passage 4**		**Passage 5**		**Passage 6**		**Passage 7**		**Passage 8**		**Passage 9**	
Up - ward	Down - ward	Up - ward	Down - ward	Up - ward	Down - ward	Up - ward	Down - ward	Up - ward	Down - ward	Up - ward	Down - ward	Up - ward	Down - ward	Up - ward	Down - ward	Up - ward	Down - ward
0.23	1.84	0.33	1.41	0.23	2.66	0.31	1.66	0.35	0.51	0.23	1.46	0.3	2.55	0.7	5.31	0.57	2.15
0.24	2.1	0.35	1.86	0.22	2.81	0.32	1.51	0.37	0.46	0.27	1.8	0.32	2.11	0.69	5.34	0.56	1.76
0.23	2.01	0.46	1.14	0.22	2.89	0.35	1.4	0.32	0.77	0.28	0.85	0.39	2.43	0.69	5.29	0.76	1.75
0.37	1.18	0.38	1.11	0.1	1.51	0.37	1.07	0.48	1.17	0.34	1.3	0.21	1.64	0.7	4.7	0.47	0.72
0.3	2.02	0.38	0.62	0.12	1.42	0.36	1.26	0.37	0.59	0.32	1.28	0.2	1.17	0.51	3	0.29	0.5
0.3	0.89	0.32	1.16	0.11	1.41	0.46	1.56	0.36	0.65	0.34	1.1	0.34	1.35	1.09	2.35	0.41	0.42

M. AFM Interior Profilometry, Rz (μm)

Passage 1		Passage 2		Passage 3		Passage 4		Passage 5		Passage 6		Passage 7		Passage 8		Passage 9	
Up - ward	Down - ward	Up - ward	Down - ward	Up - ward	Down - ward	Up - ward	Down - ward	Up - ward	Down - ward	Up - ward	Down - ward	Up - ward	Down - ward	Up - ward	Down - ward	Up - ward	Down - ward
1.2	10.89	2.42	7.48	1.19	11.68	1.43	7.67	1.7	3.05	1.46	8.93	2.52	11.54	2.89	30.36	2.62	12.63
1.17	11.86	1.97	10.42	1.1	13.08	1.57	6.65	2.46	3.08	1.77	12.39	1.62	16.13	2.88	28.63	2.52	10.37
1.13	10.74	2.43	6.28	1.1	13.75	1.62	6.51	1.68	3.86	1.8	4.67	2.1	13.26	2.82	28.58	3.14	10.47
1.47	8.07	1.66	7.42	0.73	8.08	1.2	5.19	3.07	7.48	2.13	5.74	1.2	9.65	3.26	22.24	1.87	4.63
1.5	15.69	1.78	5.23	0.92	7.83	1.33	7.58	1.75	4.37	2.11	6.37	1.41	6.07	2.25	15.03	1.7	2.36
1.59	6.24	1.62	8.14	0.73	7.77	1.86	8.24	2.33	4.24	2.55	5.56	1.76	7.31	3.76	12.1	1.71	1.79